Trapping and Manipulating Single Molecules of DNA

Citation

Shon, Min Ju. 2014. Trapping and Manipulating Single Molecules of DNA. Doctoral dissertation, Harvard University.

Permanent link

http://nrs.harvard.edu/urn-3:HUL.InstRepos:11744428

Terms of Use

Share Your Story

The Harvard community has made this article openly available.
Please share how this access benefits you. Submit a story .

Accessibility

Trapping and Manipulating

Single Molecules of DNA

A dissertation presented

by

Min Ju Shon

to

The Department of Chemistry and Chemical Biology

in partial fulfillment of the requirements

for the degree of

Doctor of Philosophy

in the subject of

Chemistry

Harvard University

Cambridge, Massachusetts

October 2013

Dissertation Advisor: Professor Adam E. Cohen   Min Ju Shon

Trapping and Manipulating Single Molecules of DNA

Abstract

This thesis presents the development and application of nanoscale techniques to trap and manipulate biomolecules, with a focus on DNA. These methods combine single-molecule microscopy and nano- and micro-fabrication to study biophysical properties of DNA and proteins.

The Dimple Machine is a lab-on-a-chip device that can isolate and confine a small number of molecules from a bulk solution. It traps molecules in nanofabricated chambers, or "dimples", and the trapped molecules are then studied on a fluorescence microscope at the single-molecule level. The sampling of bulk solution by dimples is representative, reproducible, and automated, enabling high-throughput single-molecule experiments. The device was applied to study hybridization of oligonucleotides, particularly in the context of reaction thermodynamics and kinetics in nano-confinement.

The DNA Pulley is a system to study protein binding and the local mechanical properties of DNA. A molecule of DNA is tethered to a surface on one end, and a superparamagnetic bead is attached to the other. A magnet pulls the DNA taut, and a silicon nitride knife with a nanoscale blade scans the DNA along its contour. Information on the local properties of the DNA is extracted by tracking the bead with nanometer precision in a white-light microscope. The system can detect proteins bound to DNA and localize their recognition sites, as shown with a model protein, EcoRI restriction enzyme. Progress on the measurements of nano-mechanical properties of DNA is included.

Acknowledgments

If I had to restart my Ph.D. course now (!), I will choose to start it in the Cohen Group. Adam Cohen was not just a resourceful scientific advisor: I also learned from him how to live. I deeply thank for all the past guidance, as well as for the future guidance in mind.

Scientists of a feather rock together: witnessing the fly of the group as whole was truly exciting. I owe many thanks to the smart people around me in the group. I overlapped with Alex Fields, Yiqiao Tang, Jennifer Hou, Prashant Jain, Nan Yang, Halil Bayraktar, Joel Kralj, Sabrina Leslie, Daniel Hochbaum, Hohjai Lee, Dougal Maclaurin, Veena Venkatachalam, Lucy Rosenbaum, Jeehae Park, Tony Shen, Daan Brinks, Kit Werley, Sami Farhi, Dian Yang, Peng Zou, Vedha Nathan, Niklas Smedemark-Margulies, Miao-Ping Chien, and Shan Lou. In particular, I thank Alex who shared a fair amount of time talking to and teaching me as a full-fledged member of the group. I also thank Maggie Kenar and Jeff Fosdick for administrating the group and Benjamin Altheimer and Ariana Mann who helped me during their time in the Cohen Group.

I thank Sunney Xie and Suckjoon Jun on my Graduate Advising Committee for providing guidance on my project throughout the program: I now realize how constructive these advices were. I also thank William Shih and Joseph Loparo on my Dissertation Defense Committee for making my final defense on a short notice, in spite of the travel from Longwood. I also thank Xiaowei Zhuang and Timothy Blosser, the first academic acquaintances at Harvard, who taught me the value of glucose oxidase during the rotation. Lastly, I thank Tony Shaw and Allen Aloise, for directing not just the program but me as well.

Fabrication is another title for my Ph.D. projects. I thank the CNS staffs, especially Jiangdong Deng, Ling Xie, Yuan Lu, and Philippe de Rouffignac, for helping me with the fabrication tasks. I thank Hwan Sung Choe, Jungwon Park, and Gi-Dong Sim for sharing thoughts and goods at critical junctures.

Research is only the half of my story in the graduate school. I was lucky enough to meet Nari Yoon on a night a Labview code crashed. I truly thank Nari, for just being there, and traveling a thousand miles to make my final defense.

Jae-byum Chang and Thummim Cho were my closest friends, colleagues, and coworkers. I thank them for sharing ideas and jokes, albeit lame most of the time.

Though remote in both space and time, I felt warmth of the heart from Seoul. I thank my family members for supporting me, and I feel sorry that I was not able to take a good care of them from here.

Table of Contents

1 Dimple Machine: Trapping DNA 1

List of Figures

List of Tables

Abbreviations

AFM	Atomic force microscope
APD	Avalanche Photodiode
APTES	(3-Aminopropyl)triethoxysilane
EM-CCD	Electron-multiplying charge-coupled device
FJC	Freely jointed chain
FRET	Förster (or fluorescence) resonance energy transfer
HEPES	4-(2-hydroxyethyl)-1-piperazineethanesulfonic acid
LPCVD	Low-pressure chemical vapor deposition
MIBK	Methyl isobutyl ketone
IPA	Isopropyl alcohol
PBS	Phosphate buffered saline
PCA	Protocatechuic acid
PCD	Protocatechuate-3,4-dioxygenase
PCR	Polymerase chain reaction
PDMS	Polydimethylsiloxane
PEG	Polyethylene glycol
PMMA	Poly(methyl methacrylate)
PVP	Polyvinylpyrrolidone
RIE	Reactive ion etching
SEM	Scanning electron microscope
SNR	Signal-to-noise ratio
ss(ds)DNA	Single-stranded (double-stranded) DNA
TAE	Tris-acetate-EDTA buffer
WLC	Worm-like chain

1 Dimple Machine: Trapping DNA

1.1 Introduction

A molecule is a living thing. Following the footsteps of Robert Brown who noticed the jittering of a single pollen grain[1], a group of scientists has sought to follow the footsteps of molecules, while another group has decided to confront them. I was among the latter and built a molecule trap: hundreds of nanoscale glass wells dug in an area smaller than a pinpoint.

Dimple Machine is a device for trapping and observing molecules at the single-molecule level[2] (Figure 1.1). Nanofabricated glass chambers, or "dimples", are bathed in a solution of fluorescently labeled molecules, a lid made of PDMS closes the dimples capturing the molecules, and the trapped molecules are illuminated with a laser in an inverted fluorescence microscope. Once all the fluorophores are photobleached, the dimples can be refilled with a new set of molecules, repeating the same experiment.

This technique combines nanofabrication, microfabrication, microfluidics, and single-molecule fluorescence microscopy. The device enables highly parallel, long-term, and attachment-free studies of single molecules or small numbers of molecules confined in nanofabricated chambers.
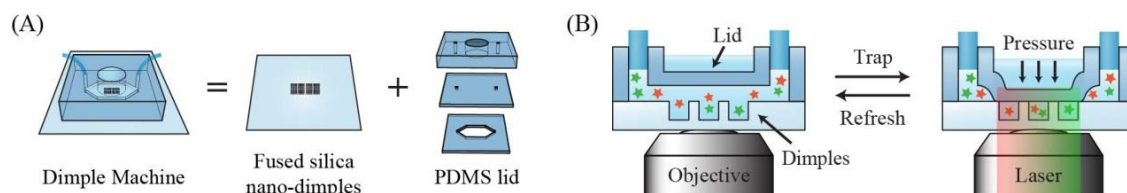
Figure 1.1   Scheme for the Dimple Machine
(A) Combination of nanofabricated dimples and a PDMS lid. (B) Cartoon of trapping (*toward right*) and refreshing (*toward left*) cycle of the device with the lid closing and opening, respectively (not drawn to scale).

1.2 Background

1.2.1 Introduction

The Dimple Machine is about trapping single molecules, imaging single-molecule fluorescence, and studying molecular interaction. This chapter reviews the background in which the Dimple Machine falls.

1.2.2 Single molecule experiments and diffusion

Brownian motion

When a molecule is freely diffusion in solution, the RMS distance it travels, r_{RMS}, during the time t is

$$r_{RMS} = \sqrt{\langle \Delta r_{3D}^2 \rangle} = \sqrt{6Dt} \tag{1}$$

where D is the diffusion coefficient of the molecule. For a spherical particle with a radius, r, this number is given by the Stokes-Einstein equation:

$$D = \frac{k_B T}{6\pi\eta r} \tag{2}$$

where k_B is the Boltzmann constant, T is the temperature, η is the dynamic viscosity of the medium. As evident from this relation, the Brownian motion is larger when the molecule is small and the temperature is high. Because we are interested in trapping small molecules ($a \sim 2$ nm) in aqueous solution ($\eta \sim 10^{-3}$ Pa s at 20 ℃) at room temperature ($T \sim 293$ K), the diffusion coefficient in this case will be $D \sim 10^{-10}$ m^2/s or 100 μm^2/s. Plugging in this value in Eq. (1) and $t = 1$ s, for example, gives $r_{RMS} = 24$ μm. That is, the molecule of interest will travel ~24 μm from its original location within 1 s. This condition results in two difficulties in single-molecule experiments: (1) tracking the random, fast motion of the molecule in solution is challenging, and (2) the molecule escapes the field of view of microscope, $(100 \text{ μm})^2$–$(1 \text{ mm})^2$, within a few seconds.

Immobilizing single molecules

The primary challenge in the early age of single-molecule experiments was to suppress Brownian motion. For this reason, the first reports of single-molecule imaging in solution were conducted in gels, utilizing the pores of polymer matrix for immobilization[3,4]. Later, fixing the molecule to a glass surface has played a key role in the development of single-molecule fluorescence techniques[5]. Here, a molecule is first covalently labeled with a bright fluorescent dye (typically cyanine-based dyes), and a functional group on the molecule, either endogenous or exogenous, is used to attach the molecule to a glass coverslip. Popular methods of surface tethering include antibody-antigen pair (such as streptavidin-biotin), gold-sulfur, amine-aldehyde crosslinking. The rest of the surface that did not react with the molecules are blocked to reduce nonspecific interactions, by coating poly(ethylene glycol) or bovine serum albumin.

The major drawback of these methods, however, is that the molecule of interest needs to be chemically modified. One needs to introduce a chemical group suited for attachment. For proteins, the endogenous functional groups might serve as a point of linkage, but this solution is not universal because of diversity of protein structure. In addition, the surface attachment increase the interaction between the molecules and surface kinetically, which often affects the structure and activity of biomolecules. A relatively long molecular tether can be used to reduce the surface artifact at the cost of complexity in preparing samples. Lastly, the tumbling of molecule is constrained, sacrificing the rotational freedom of molecule.

Vesicle encapsulation

Instead of surface attachment, one can use droplet-like structures to encapsulate molecules and create barrier. The advantage of vesicle encapsulation over direct tethering is that the molecules themselves do not need any modification.

The first instance was using lipid vesicles. Single protein molecules are trapped inside 100 nm lipid vesicles, and the vesicles are in turn tethered to a surface with a supported lipid bilayer. This method was used to study enzymatic reactions[4], protein folding[6], and oligonucleotides[7,8].

A hydrosome was also used to trap single molecules[9]. In this technique, single molecules are trapped within micron-sized water droplets, or hydrosomes, suspended in fluorocarbon oil, and a target hydrosome

3

is steered by using an optical tweezer. The molecule inside the hydrosome was shown to be freely rotating by measuring fluorescence anisotropy. A unique advantage of this technique is to mix contents of two hydrosomes, suited to studying reactions.

Trapping in Cohen Group

One specialty of the Cohen Group is trapping molecules for single-molecule fluorescence imaging. There are two techniques developed before the Dimple Machine.

Anti-Brownian Electrokinetic (ABEL) trap is a device for trapping molecules in solution[10]. It works by monitoring a molecule in solution, tracking it fast to measure the displacement from its original position, and applying a feedback voltage to the solution to induce electrokinetic drift to move the molecule back to the original position. A trapped molecule is observed for seconds, and the measurement can be repeated with a new molecule. Since its first implementation trapping nanospheres[10], the technique has evolved to trap and study virus particles[11], proteins[11,12], DNA[13], and a small-molecule dye[14].

Convex Lens-Induced Confinement (CLIC) is a system that confines molecules in a nanoscale gap, thus constraining the diffusion into a plane[15]. When a fused silica convex lens is brought into contact with a coverslip, the two surfaces form a wedge-shaped gap, the height of which varies smoothly at the nanometer scale. When a solution of molecules is places in this gap, the diffusion in the vertical dimension is effectively blocked. This simple setup rejects the fluorescent background greatly, thereby improving SNR of single-molecule imaging. In addition, the technique can measure the diameter of small proteins by measuring the exclusion of molecules as a function of gap height.

The underlying principle of CLIC and the Dimple Machine is the same: isolating molecules from a bulk solution, rejecting background molecules from imaging. The difference is that the CLIC is 1-D-confinement, imaging molecules in a plane, whereas the Dimple Machine achieves 3-D-confinement, imaging molecules at a point. Note, however, that these methods do not put the molecules *on* the surface, unlike surface attachment. Because the scale of confinement is still greater than the molecular scale, the molecules are free from surface interaction.

1.2.3   Single-molecule fluorescence at high concentration

Detection volume in single-molecule imaging

Imaging single molecules means labeling the molecules with fluorescent dyes, unless the molecule is naturally fluorescent like organic dyes or fluorescent proteins. Since the first optical detection of a single dye[16], the brightness and quantum yields of organic dyes have improved significantly. In parallel, the efficiency of photon detectors has improved, enabling single-photon detection at room temperature.

If the solution is concentrated, however, imaging single molecules encounters another challenge: spatially resolving molecules. One can think of the mean volume per molecule, V_1, in a given solution:

$$V_1 = \frac{1}{N_A c} \tag{3}$$

where N_A is the Avogadro's number, and c is the molar concentration of the solution. For $c = 1$ nM, V_1 becomes around 1 femtoliter (10^{-15} L), which corresponds to the mean separation of molecules ~1 µm.

For an optical system to resolve single molecules, the detection volume must be smaller than V_1 (Figure 1.2). Because the resolution limit of conventional fluorescence optics is ~300 nm at best, the molecules in 1 nM solution will look mostly overlapped with another. This imposes an upper limit on the working concentration for single-molecule imaging:

$$c = \frac{1}{N_A V_1} < \frac{1}{N_A V_{det}}. \tag{4}$$

In particular, the sensitivity in *z*-direction of epifluorescence microscopes is worse than the *x*- and *y*-directions, because the objective looks *through* the sample, collecting light from a thick section of the sample. Therefore, to resolve a single molecule from bulk, the detection volume of the optical systems must be smaller than the average volume a molecule occupies at the given concentration.
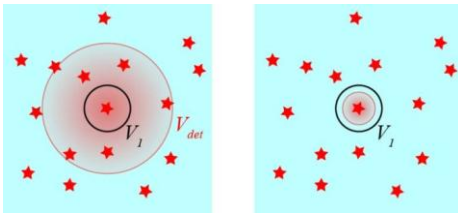
Figure 1.2   Detection volume in single-molecule imaging
In order to resolve single molecules in solution, the detection volume (V_{det}) must be smaller than the mean volume per molecule (V_1).

Sadly, this maximum concentration in single-molecule imaging precludes studying weak molecular interactions. Consider a reversible interaction between *A* and *B* to form *AB*:

$$A + B \rightleftarrows AB \tag{5}$$

with an equilibrium dissociation constant K_{d}:

$$K_{\text{d}} = \frac{[A]_{eq}[B]_{eq}}{[AB]_{eq}} \tag{6}$$

where $[A]_{eq}$, $[B]_{eq}$, and $[AB]_{eq}$ are the equilibrium concentrations of *A*, *B*, and *AB*, respectively. From the law of mass action, the expression can be rewritten as below:

$$K_{\text{d}} = \frac{\big([A]_0 - [AB]_{eq}\big)\big([B]_0 - [AB]_{eq}\big)}{[AB]_{eq}} \tag{7}$$

where $[A]_0$ and $[B]_0$ are the initial concentrations of *A* and *B*, respectively. For a weak association with a K_{d} of 1 μm prepared at $[A]_0 = [B]_0 = 1\,\text{nM}$, solving the Eq. (7) for $[AB]_{eq}$ gives $[AB]_{eq} = 1\,\text{pM}$, a virtually non-existent fraction of the preparation. When $[A]_0 = [B]_0 = 1\,\text{μM}$, however, then $[AB]_{eq} = 0.4\,\text{μM}$, roughly half of the reactants *A* and *B* forming the products *AB*. That is, to keep weakly associating complexes, the concentration of solution must be kept comparable to its dissociation constant. As a result, this condition conflicts with the condition for single-molecule imaging. Therefore, methods of single-molecule imaging with sufficiently small detection volumes are desired.

Optical techniques for reducing detection volume

A wide variety of optical schemes decreasing the detection volume has been developed. The oldest scheme is confocal fluorescence microscope using a focused laser beam with a pinhole to reject out-of-focus fluorescence background. An advanced version of this setup is confocal *scanning* microscope, enabling imaging over a plane rather than a single point. Total internal reflection fluorescence (TIRF) is another trick to reject background in *z*-axis. In this setup, the excitation laser beam is aligned at an angle to the glass substrate. When this angle is larger the critical angle, only the evanescent wave field emerging from the water-glass interface is illuminating the sample. Because the evanescent field decays quickly in ~100 nm, only the sample near the surface is illuminated, emitting fluorescence. More recently, single-plane illumination microscopy[17], using a light sheet to excite a section of the sample, was also applied to track single-molecule in *vivo*[18]. The CLIC device is also reducing the background in *z* by physically

displacing fluorescent molecules. These methods, however, works to reduce background in z direction, only, leaving the resolution issue at high concentration unchanged in x and y.

Recently, the zero-mode waveguide (ZMW) is developed to further decrease the detection volume[19]. In this technique, the excitation light is passed through nanofabricated chambers with aluminum cladding. Inside the chambers, the excitation of the molecules occur only by the allowed mode of the light, thereby reducing the excitation volume. However, the dramatic reduction of detection volume in this device trades off the observation time because the molecules once detected in the chamber will diffuse out of the excitation volume quickly, in 1 ms.

1.2.4 Motivations for the Dimple Machine

As reviewed in the previous sections, single-molecule imaging requires a way to immobilize molecules, preferably not restricting their internal degrees of freedom. Achieving this goal at relatively high concentrations would be preferable for studying weak interactions.

The Dimple Machine employs nanofabricated glass chambers to isolate and immobilize molecules. Once trapped in the chamber, the molecules remain at the predefined positions until they are released. The confinement occurs at 100 nm–1 μm length scale. Therefore, the molecules are localized within the diffraction-limited spot, yet freely diffusing at the molecular scale.

Dimple Machine technology provides a possible resolution to many challenges associated with single-molecule measurements in solution[20]. Molecules in free solution are typically observed for fleeting moments due to diffusion, while surface tethering may disrupt molecular function. Feedback systems[10,12,14] or spatial confinement[8,9,15,21–33] provide an approach to keep molecules within an observation volume while permitting unconstrained motion on the molecular scale. Confinement in 2-D sheets[15] or 1-D channels[21–23] does not completely suppress Brownian motion, while confinement in vesicles[8,9,24–27] leaves molecules randomly distributed and does not provide precise control over the confinement volume, nor a means of replenishing the molecules after photobleaching. Confinement in etched optical fiber bundles has been used to study single-molecule dynamics[28–31], but the requirement that the lateral dimensions be comparable to the optical wavelength leads to significantly larger confinement volumes than described here. The Dimple Machine reversibly confines molecules to well-defined volumes at well-defined locations. The device uses a small sample (< 1 pmol), acquires a large dataset automatically, and can be reused indefinitely.

High-concentration single-molecule experiments. Consider a cubic dimple with a side a. When the dimple traps molecules from the bulk solution, it essentially isolates a small volume for observation. That is, the detection volume of this method is the volume of a dimple, a^3. From Eq. (4), we can calculate the maximum working concentrations for the Dimple Machine (Table 1.1). By using dimples smaller than 100 nm, one can work with a solution at millimolar concentrations and still resolve single molecules.

Table 1.1   Dimple size and maximum concentration for single-molecule imaging

Dimple size	Volume	Maximum concentration
10 nm	10^{-21} L	1.7 mM
100 nm	10^{-18} L	1.7 µM
1 µm	10^{-15} L	1.7 nM

Homogeneous size distribution. The nanofabrication of dimples is highly homogeneous, resulting in uniform size distribution. When vesicles are prepared for encapsulating molecules, for example, their sizes are loosely controlled by the diameter of holes in the polycarbonate membrane used for lipid extrusion. When the dimples are prepared, the uniformity of the sizes is limited by the resolution of electron-beam lithography, which is typically 5–10 nm. Using a higher voltage (100 kV) and high-resolution e-beam resist can improve the resolution even further (1 nm). The homogeneity of the dimples can be critical when the volume of the container matters, such as in studying reactions in nanoconfinement (Section 1.6).

High throughput. The unique advantage of the Dimple Machine is that the trapping is reversible. The observation time in single-molecule imaging is limited by photobleaching event. Therefore, surface immobilization methods are limited by the finite number of molecules immobilized on the surface. In the Dimple Machine, the dimples can be refilled with a new set of molecules from the bulk solution. This repetition of sampling is virtually infinite.

Regular pattern. Most of the surface attachment chemistry does not have the control over the position of the molecules. In the Dimple Machine, on the contrary, the location of molecules is predefined by patterning in the electron-beam lithography. Since the pattern is drawn with computer-aided design software, one can create an arbitrary design for the dimple array. If they are patterned in regular arrays, the analysis becomes simple because nonspecifically adsorbed molecules can be discriminated easily.

1.3 Fabrication of Dimple Machine

1.3.1 Introduction

I devoted my first few years in the Cohen Lab to the fabrication of Dimple Machine. This section steps through the three stages of Dimple Machine production line: (1) nanofabrication of the dimples on a glass coverslip, (2) microfabrication of the lid from a rubber, and (3) assembly of the products from (1) and (2) to form the final device.

1.3.2 The Beginning: Choice of materials

My first learning in the lab has begun in materials science: we had to choose fitting materials for the dimples and the lid. Qualifications include: (a) optically clear to minimize background in fluorescence microscopy, (b) chemically compatible with biomolecules, (c) amenable to fabrication for patterning dimples or shaping the lid, and (d) mechanically proper for trapping molecules. We started from fused silica dimples and a PDMS lid, and this turned out appropriate.

Fused silica dimples

Most of samples going on optical microscopes are prepared on glass or plastics due to their excellent transparency and hardness. From a fabrication perspective, soft materials are much easier to engineer. However, dimples must be made of a hard material to maintain their shapes at the *nanoscale*. This condition discourages the use of soft materials like PDMS[*] or PMMA when making dimples (Table 1.2). Among many subtypes of glasses, fused silica is particularly suited to single-molecule fluorescence microscopy because of its minimal autofluorescence.

Table 1.2   Young's modulus for selected materials

Material	Class	Young's modulus
PDMS	Elastomer	~0.5 MPa
PMMA	Polymer	2 GPa
Soda lime	Glass	50–100 GPa
Fused silica	Glass	72 GPa

---

[*]Recently there are progresses on patterning nano-features on PDMS[96].

PDMS Lid

For the lid of Dimple Machine, in contrary to the dimples, a softer material that can deform when pushed against a flat surface is preferred to cover many dimples over a wide area. PDMS is an elastomer widely employed in soft lithography due to its excellent mechanical properties. Similar to the carbon-based polymers, native PDMS is hydrophobic and sticky toward biomolecules. However, thanks to the high demand for PDMS, various methods reducing adsorption of biomolecules on PDMS have been developed[34–36].

In addition to PDMS, there are a few more candidate materials for the lid. The entries in Table 1.3 are examined when we faced many challenges associated with PDMS, especially a high autofluorescence and background fluorescence coming from impurities. After months of screening, these other materials were concluded to be inapplicable because of the limiting properties (ranked "bad" in Table 1.3), leaving PDMS as yet the best option.

Table 1.3   Potential materials for the lid

Lid material	PDMS	Polyacrylamide	Fused silica	Fluorocarbon oil
Low autofluorescence	fair	very good	very good	good
Hermetic sealing	fair	bad	good	unknown
Wide coverage	very good	good	bad	very good
Impermeable	good	bad	very good	good
Low adsorption	fair	very good	good	bad
Easy to shape	very good	fair	fair	fair
Simple design	very good	fair	very good	fair
Easy to actuate	very good	fair	fair	very good
TIRF-compatible	fair	very good	bad	very good

1.3.3   Nanofabrication of dimples

The heart of the Dimple Machine is a fused silica coverslip containing multiple arrays of nanofabricated circular depressions, or "dimples", with diameters ranging from 70 nm to 1.3 μm and a depth of 200 nm. Regular arrays of dimples are first patterned on PMMA by electron-beam lithography, and then transferred to a fused silica coverslip by reactive ion etching (Figure 1.3).

Electron-beam lithography

A 1" square fused silica coverslip (Esco, R425025 S1-UV) was cleaned in piranha solution (3:1 concentrated sulfuric acid:hydrogen peroxide) at 70 ℃ for 30 min, followed by rinsing in water. The substrate was then spin-coated with adhesion promoter (ShinEtsu, MicroSi MicroPrime HP Primer, at 1,000 rpm), electron-beam lithography resist PMMA (MicroChem, 950 A4, at 3,000 rpm), and conducting polymer[*] (Showa Denko, Espacer300, at 1,000 rpm) in sequence.

Electron-beam lithography was carried out by JEOL JSM-7000F at an accelerating voltage of 30 kV and an electron dose in the range of 700–1,200 μC/cm^2. Typically, 40 dimple arrays were written on one substrate during the exposure, and each array (120 μm $\times$ 120 μm) contained 900 circular dimples of varying sizes, arranged in a square lattice with spacing 4 μm.

Reactive ion etching

The processed substrate was (1) washed in water to dissolve the conducting polymer layer, (2) developed in 1:3 MIBK:IPA for 2 min, and (3) washed in IPA. The developed substrate was briefly cleaned
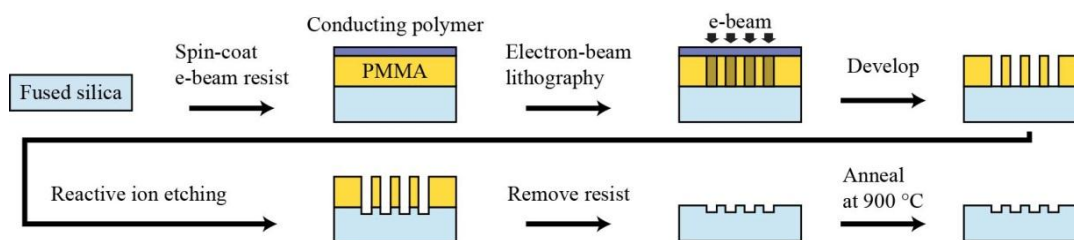
Figure 1.3   Nanofabrication scheme for the dimple arrays

---

[*] Dissipation of electrons during the electron-beam writing is critical when the substrate is insulating. Without a path for discharging, the accumulating electrons gradually repel incoming charges leading to the blurring of patterns, or crack the substrate. A thin layer of metal (~10 nm-thick Cr/Au, for example) had been typically used as a discharge layer, but it requires metal evaporation and wet etching. I learned that water-soluble conducting polymer is a simple and effective alternative: it is deposited by spin coating in 1 min, and removed by rinsing in water in 30 s.

by oxygen plasma (Technics Micro-stripper, 30 mTorr of oxygen for 30 s) and the exposed fused silica was etched in a reactive ion etching system (STS-ICP-RIE) by fluorine-based recipe[*] using PMMA as a mask. Because the etch rate inside a nanoscale cavity is slower than in bulk and nonlinear over time, a careful calibration of etch rate is necessary. Note that PMMA is a weak etch mask for dry-etching fused silica: a selectivity of fused silica over PMMA is ~1:1. Running a given recipe for 20 min *without* the sample to condition the equipment is recommended to obtain reproducible results in etching.

PMMA after etching was removed by dissolving in acetone and in Hellmanex aqueous solution (2% w/v) at 70 ℃ for 30 min.

Annealing

The nanofabricated fused silica was annealed in a furnace at 900 ℃ for 5 h to remove the autofluorescence from the fused silica induced by the electron-beam lithography. Minimizing background fluorescence in single-molecule measurements is crucial to enhance signal-to-noise ratio. Fused silica shows very low autofluorescence. However, we observed a high level of autofluorescence (especially under red excitation) in the regions of the sample exposed to the electron beam during electron-beam lithography (Figure 1.4). While this phenomenon was documented previously[37], we did not find any remedies in the literature. We discovered that by baking the substrate in furnace at 900 ℃ for 5 h the autofluorescence decreased to the initial low level.

Before e-beam   After e-beam   After baking
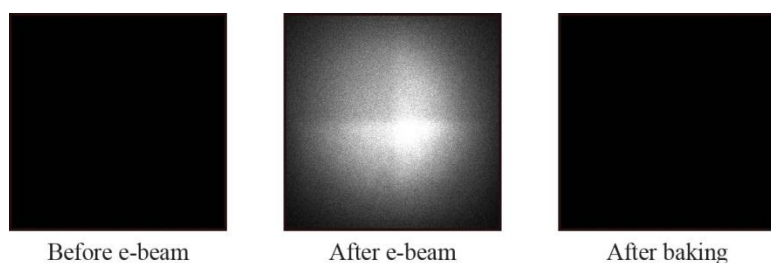
Figure 1.4   Electron-beam-induced autofluorescence of the fused silica
Surface of a fused silica coverslip imaged on a fluorescence microscope exciting at 633 nm. All images are displayed with the same brightness and contrast. Initial autofluorescence was sufficiently low to allow detection of single-molecules (*top*). Electron-beam lithography led to an increase in autofluorescence by more than 1,000-fold, in an electron-dose-dependent manner (*middle*). Baking the finished fused silica wafer in a furnace at 900 ℃ for 5 h completely eliminated the electron beam-induced fluorescence (*bottom*), without distorting the nanofabricated dimples.

---

[*] 15 sccm CHF_3, 5 sccm CF_4, 10 sccm H_2, 5 sccm Ar; 150 W RF power. This recipe etches ~200 nm of fused silica of exposed area in 80 s.

1.3.4 Characterization of dimples

White-light microscope imaging

Nanofabricated dimples can be imaged on a white-light microscope. The minimum diameter of dimples visible under white-light microscope is around 50 nm. Typically, a set of large dimples (1–2 µm diameter) were patterned together with small ones as an alignment marker. Each array in the Dimple Machine contained 900 wells, arranged in a square lattice with spacing 4 µm (Figure 1.5).
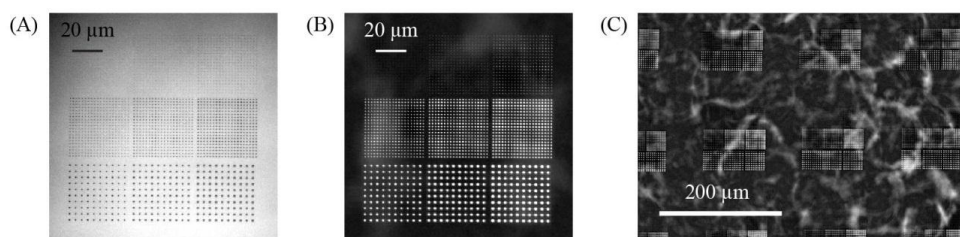
Figure 1.5   Microscope images of dimple arrays
(A) A bright-field and (B) a dark-field microscope image of a single dimple array containing 900 dimples of various sizes. (C) Multiple arrays of dimples over a wide area.

Atomic force microscope imaging

AFM (Asylum Research, MFP-3D) was used for detailed characterization of the dimples (Figure 1.6). The volume per dimple ranged from 8×10^{-19} L to 2.6×10^{-16} L, corresponding to concentrations at unimolecular occupancy between 2.2 µM and 6.3 nM. That is, this array of dimples can capture single molecules from a solution containing 6 nM to 2 µM of target species. As briefed in Section 1.2.3, the capability to isolate molecules from concentrated solutions is valuable when studying weak interactions.
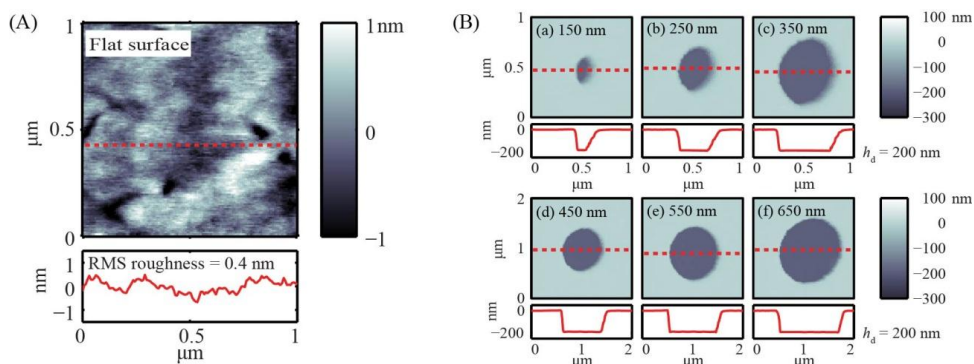
Figure 1.6   Atomic force microscope images of dimples
(A) Clean surface of a fused silica coverslip. (*Top*) Image of the surface of a fused silica coverslip after cleaned in piranha solution. Root-mean-square surface roughness was 0.4 nm. (*Bottom*) Section of the image along the red line in (*top*). (B) Nanofabricated dimples on a fused silica coverslip. (*Top*) Images of the dimples with nominal radii as annotated. (*Bottom*) Section of the scan along the red dashed line in the (*top*) image. The final depth of etching was measured to be 190–200 nm for all dimples.

1.3.5   Evolution of PDMS lid

Engineering a stable and effective lid has consumed a significant fraction of the effort spent on this project. This section delineates the history of the lid design, leading to the current generation of PDMS lid with lithographically defined microposts.

Generation 1: Lens-shaped lid

The first design was the simplest: dimple arrays on a 1" fused silica coverslip with a PDMS lid micro-positioned over the arrays (Figure 1.7). A lens-shaped lid is prepared by doping a fused silica lens with PDMS and attached to a cantilever fixed on an *xyz* translation stage, and a micrometer on the opposite end of seesaw either lifted or lowered the lid. Despite its elegantly simple design, we had at least two issues.

(a) **Force balance of the lid.**   The weight of lid was not heavy enough to seal the dimples, resulting in leakage. Having too much load on the coverslip would break the nanofabricated device.

(b) **Fluorescence background.**   Because of the bulk PDMS is positioned on top of the dimples, a high background, especially in green, was observed when taking fluorescence movies. This came from two sources: autofluorescence of PDMS, and impurities soaked into PDMS. PDMS is known to absorb fluorescent impurities from the environment.

Fortunately, we found a solution that cleared the two problems at once: a microfluidic trapping.
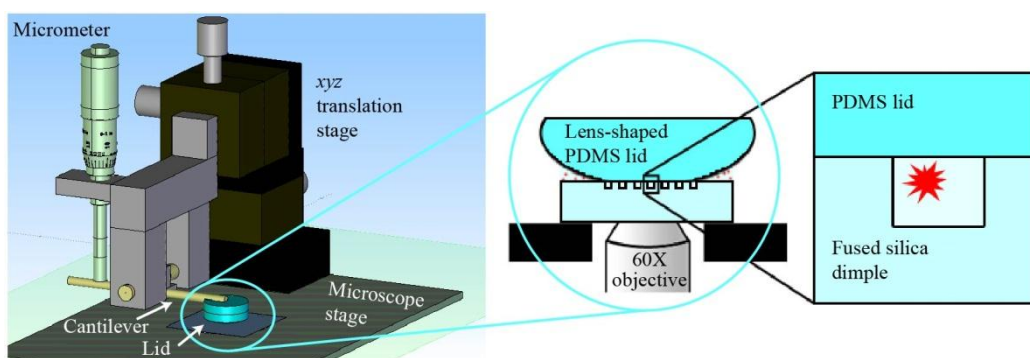
Figure 1.7   First-generation lens-shaped PDMS lid

The first-generation Dimple Machine is characterized by a seesaw cantilever holding a lens-shape PDMS lid (*top left*). The lid is first aligned to the dimple arrays on the coverslip using an *xyz* translation stage, and then manipulated with a micrometer pusher on the opposite end of the seesaw to trap or release the molecules.

Generation 2: Microfluidic lid

In this generation, the lid was made of two PDMS membranes (Figure 1.8): (1) the first layer is a sample channel with its top surface being the lid, and (2) the second layer is a control channel overlaid on top of the sample channel. When the control channel is pressurized either pneumatically or hydraulically, the membrane between the two channels bows down to form a lid sealing the dimples. This style of actuation (a.k.a. Quake valve) has been developed to control a fluid flow through a microfluidic channel.

The application of microfluidic PDMS lid has many advantages over the first-generation bulk lid. First, the lid consists only of a few hundred microns of PDMS membrane, substantially reducing the background fluorescence from the lid. Second, the trapping force of lid can be increased without the danger of breaking the coverslip because the applied force is internal to the device. In addition, the device can be configured to a digital valve for trapping, leading to automated operation and data acquisition.

The microfluidic lid was successfully implemented, and survived through to the current design with a slight modification. Two downsides of this two-layer microfluidic lid were: (a) pressurizing control channel too much led to detaching of sample channel PDMS layer from the coverslip, and (b) the two-layer design increased the complexity of fabrication.
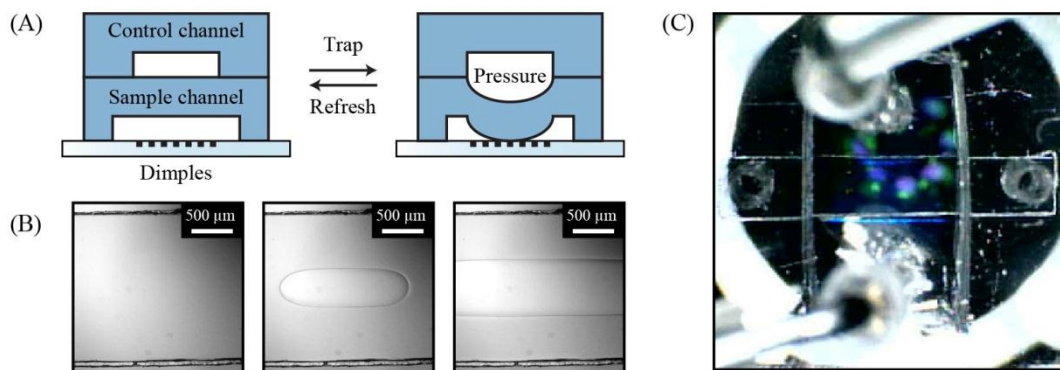
Figure 1.8   Pressure-actuated lid

(A) Pressure-actuated lid working principle. When the control channel is pressurized, either pneumatically or hydraulically, the ceiling of flow channel bows down and seals the dimples. (B) Time-lapse images of lid bowing down. The lid is open (*left*), closing (*center*), and closed (*right*). (C) A photograph of PDMS microfluidic lid. A vertical control channel is overlaid on top of a horizontal flow channel, forming a cross.

Generation 3: Vacuum-actuated lid with microposts

The scheme for vacuum-controlled PDMS lid was adapted from a publication[32]. The lid was actuated by applying vacuum to both ports of the sample chamber. Atmospheric pressure on the top of the lid then caused the lid to bow down until it contacted the silica coverslip, sealing the dimples. To refresh the dimples, the vacuum was released and the lid returned to its raised position (Figure 1.9A). In this scheme, PDMS-fused silica reversible bonding becomes more stable because the force by atmospheric pressure acts *inward* to the sample channel, rather than *pushing away* the coverslip as in Generation 2. In addition, the lid consists of a single microfluidic layer, greatly simplifying fabrication.

Microposts reduce leakage of molecules out of the dimples. Reliable sealing of the dimples is a prerequisite of trapping and accurate measurement of occupancy. The surface roughness of the substrate must be smaller than the length scale of the molecules to be trapped, typically ~1 nm. Clean fused silica has surface roughness below 1 nm (Figure 1.6A). However, plasma etching or exposure to extremes of pH gradually roughened the surface, necessitating care in cleaning. A thin aqueous film often persisted between the fused silica and the lid immediately after closing the lid. This film permitted molecules to escape from the dimples. To facilitate the draining of this film, we introduced the post topography into the PDMS lid (Figure 1.9B), thereby minimizing the distance the water had to flow to reach a deep channel. After introducing the posts, we found that the lid sealed hermetically after ~5 min.
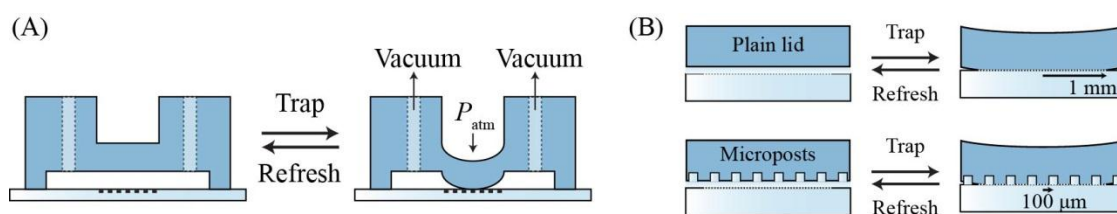
Figure 1.9   **Vacuum-actuated lid with microposts**

(A) Vacuum-actuated lid working principle. When the pressure in sample is lowered by vacuum line, the atmospheric pressure on top of the lid bows down the membrane. (B) Comparison of a plain (*top*) and a structured PDMS lid (*bottom*). The drainage in the presence of microposts can be faster by an order than a plain lid.

1.3.6   Microfabrication of PDMS lid

The following describes the procedure for fabricating PDMS lid with microposts by a standard soft lithography technique using SU-8 and PDMS[38] (Figure 1.10). Four copies of lid can be prototyped from a 3" silicon wafer. The dimension for this fabrication is presented in Figure 1.11B.
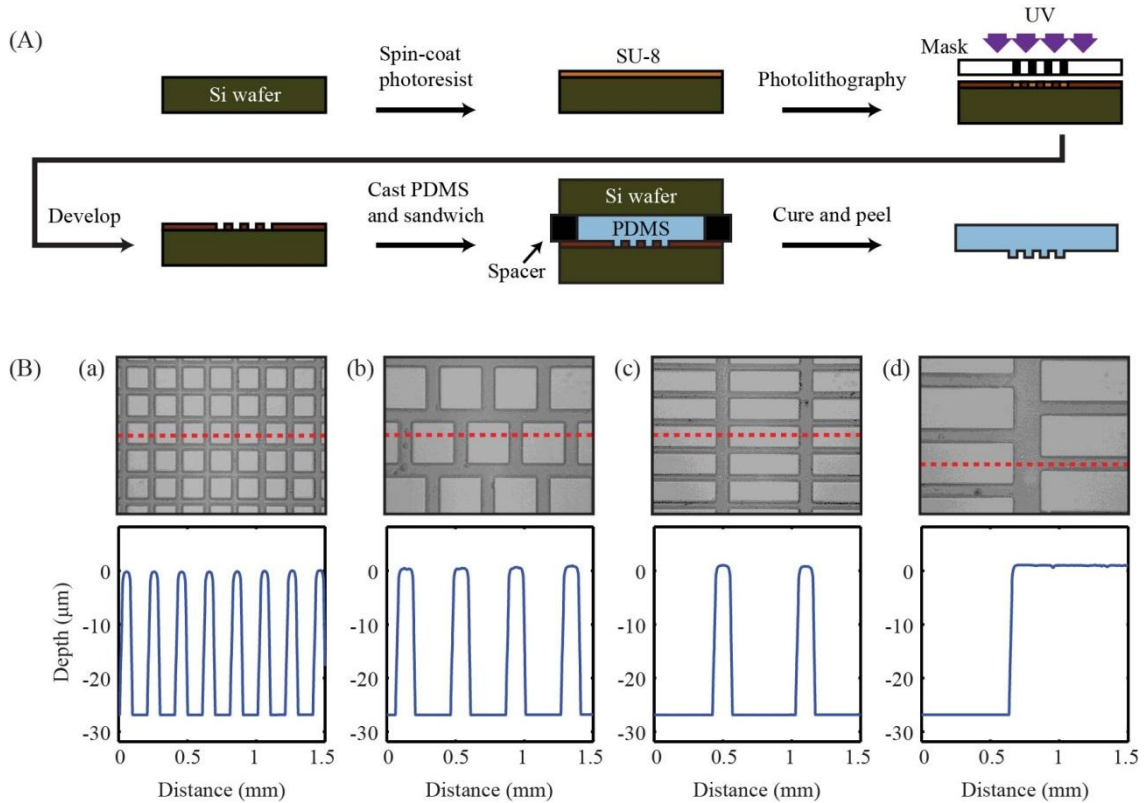
Figure 1.10 Microfabrication of the lid with microposts

(A) Scheme for the Microfabrication of the lid. (B) Microfabriated SU-8 master for the lid. (*Top*) Photo of the surface; (*Bottom*) surface scan with a contact stylus profiler (KLA-Tencor P-16+) along the red dashed line in the (*top*) image. The patterns contained squares (a) 150 μm on a 200 μm grid or (b) 300 μm on a 400 μm grid; or rectangles (c) 500 μm × 150 μm on a 600 μm × 200 μm grid, and (d) 1,000 μm × 300 μm on a 1,200 μm × 400 μm grid. The size and spacing of the posts was not critical; for each device, an array of posts was selected with dimensions that facilitated sealing of complete arrays of dimples. The height of the posts was 28 μm in all structures.

Photolithography

A 3" silicon wafer was cleaned by sonication in acetone, IPA, and methanol, successively, for 5 min each, rinsed in water, and dried on a hotplate. The cleaned wafer was coated with a negative photoresist SU-8 (MicroChem, SU-8 3025) and baked on a hotplate at 95 ℃ for 15 min. The cured resist was exposed through a transparency mask to UV for 15 min. The substrate was baked on a hotplate at 65–95 ℃ for 5 min. The resist was developed in SU-8 developer (MicroChem) for 10 min. The wafer was thoroughly rinsed with IPA and hard-baked at 200 ℃ for 30 min.

PDMS molding

The fabricated SU-8 microstructures served as a master for the fabrication of the PDMS lid. Two-part mixture of PDMS (Dow Corning, Sylgard 184, 10:1 base: curing agent) was poured over the master and topped with a bare silicon wafer to control the thickness of the PDMS membrane to 500 μm. The assembly was then cured at 80 ℃ for 5 h. The top wafer was removed carefully and the cured PDMS membrane was cut to 20 mm $\times$ 20 mm and peeled off the master.

Background autofluorescence from PDMS

PDMS is known to absorb fluorescent impurities from the environment. To minimize background autofluorescence from the PDMS, we worked with as thin a PDMS lid as possible (typically 500 μm). Prior to each experiment, the lid was closed and the area over the trapping region was exposed to the full intensity of the red and green lasers (~100 W/cm^2) for 1 h. After this photobleaching period, sample and oxygen scavenger solutions were introduced into the device. Between uses, devices were stored in a solution of PVP (0.1%) in nanopure water. For both red and green illumination, the PDMS fluorescence exceeded the signal from a single dye molecule (1,000:400 photons/s in the red; 4,000:300 photons/s in the green). However the PDMS fluorescence was constant over time, so the shot-noise-limited SNR in a 1 Hz bandwidth was approximately 10.7 (red) and 4.6 (green).

1.3.7   Lid-dimple assembly

Three-layer PDMS lid

The last step of fabrication is to bond the PDMS lid onto the dimple coverslip with a careful alignment (Figure 1.11). The assembly starts from irreversible bonding of three PDMS layers. Three layers of PDMS were prepared as below. Surfaces of these layers were activated by oxygen plasma for 1 min (SPI, Plasma-Prep II) and then irreversibly bonded.

1. **Sample channel spacer.** This is a spacer between the dimple coverslip and the lid with a hexagonal sample channel cut out with a knife (500-μm-thick). This bottom layer is what defines
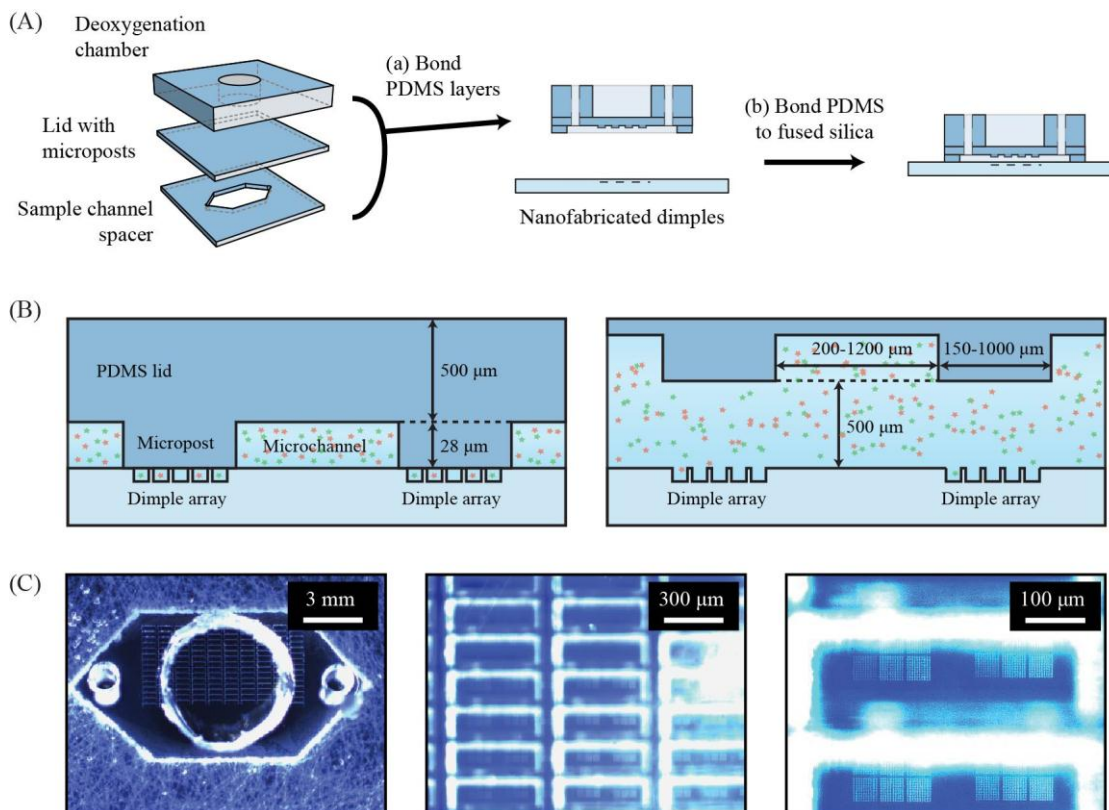
Figure 1.11 Lid-dimple assembly

(A) Scheme for the lid-dimple assembly. (B) Cartoon of the sample channel. The lid is shown when sealing (*left*) and refreshing the dimples (*right*). (C) Microscope images of the PDMS lid assembly. (*Left*) A full view of the sample channel from the top. (*Middle*) Micropost arrays placed on the dimple substrate. (*Right*) A close view of the dimple arrays aligned under the rectangular microposts.

the sample channel. The thickness of this layer determines the distance of dimples from the lid at a resting state. The hexagonal channel in the middle is cut by hand scribing with a X-ACTO knife.

2. **Microfabricated lid membrane.**   This is the lid layer with microposts (500-μm-thick) (Figure 1.9) described in Section1.3.5. We optimized the thickness of the membrane (~500 μm) for an optimal flexibility of the lid.

3. **Deoxygenation chamber**.   This is a 3-mm-thick slab of PDMS with a hole in the center. This top floor has many roles. Most importantly, the aperture punched in the center (~5 mm diameter) defines the lid area that will bow down upon pressure change. The reservoir created by this hole was loaded with deoxygenation buffer for the two reasons below.

   (a) *Suppression of photobleaching via remote deoxygenation from across the lid membrane*: Photobleaching in single-molecule fluorescence experiments can be suppressed by enzymatic deoxygenation of the solution. We exploited the oxygen permeability of PDMS to deoxygenate the dimples from deoxygenation chamber, the top side of the PDMS lid. The reservoir on top of the PDMS lid was loaded with deoxygenation buffer (see Table 1.6 in Section 1.4.3). This reservoir generated a reversed oxygen concentration gradient spanning the lid membrane, causing oxygen to diffuse *out* of the dimples and into the PDMS lid.

   (b) *Diffusion of water into the PDMS lid leading to drying of the dimples*: PDMS absorbs water to a small extent. Each sealed dimple contained less than 1 fL of water, which easily was absorbed into the PDMS lid. The deoxygenation buffer on top of the lid also saturated the lid with water, preventing additional absorption of water from the dimples. The device was run inside a humidified chamber to prevent drying of the deoxygenation buffer. The sealed dimples remained hydrated until the deoxygenation buffer dried out, usually after more than 1 day.

Reversible bonding of lid and dimples

Two ports for sample injection were punched into the PDMS lid complex using a blunt needle (18G). The microposts on the lid were aligned to the dimple arrays by assembly under a dissecting microscope (Figure 1.11C) with a custom three-axis aligner (Thorlabs, DT12). The reversible attachment between PDMS and fused silica was strong enough to maintain a bond throughout the experiments and allowed disassembly, cleaning, and reuse without sacrificing the lid or the substrate.

1.4 Trapping and Counting Molecules

1.4.1 Introduction

This section describes the operation of Dimple Machine and the results: trapping and counting molecules. Dimple Machine traps a sample of oligonucleotides labeled with a red dye, and counts the number of molecules in each dimple by measuring fluorescence emission with a fluorescent microscope and an EM-CCD. The operation of the device was fully automated so that the trap-measure-refresh cycle could be repeated an arbitrary number of times.

1.4.2 Fluorescence microscope setup

Dimple Machine runs on an inverted fluorescence microscope. Fluorescent molecules in dimples are excited with lasers through a $60\times$ oil-immersion objective. Depending on the applications, one can decide on whether to use a parallel wide-field imaging with an EM-CCD (Figure 1.12), or to use a serial confocal scanning with a single-photon counting APD (Figure 1.13). When more than one color is desired, an upgraded setup with two lasers and a dual-view camera can be configured. This section compares the merits of different optical setups.
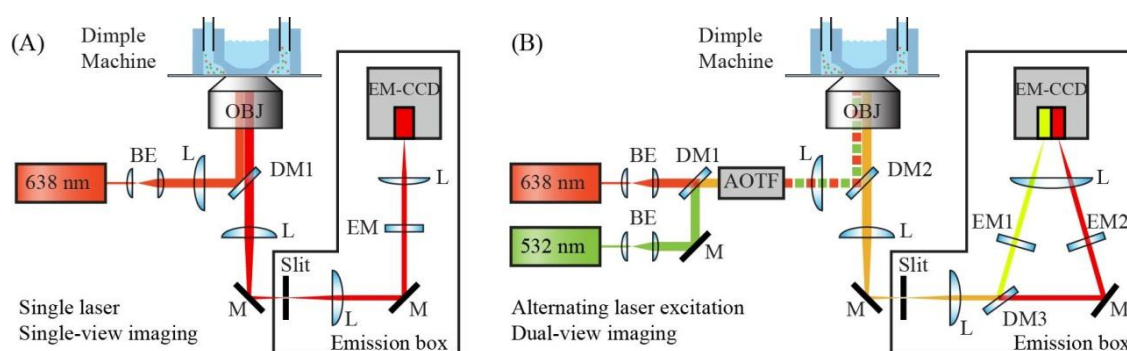
Figure 1.12 Optical setup for the wide-field Dimple Machine
(A) Single-color setup. An inverted microscope is equipped with a single laser (either red or green) and an EM-CCD camera. (B) Two-color imaging setup. An inverted microscope is equipped with alternating red and green laser excitation and a dual-view camera.

Wide-field Dimple Machine

Single color setup. The simplest setup for a wide-field imaging consists of a single laser for excitation, an inverted microscope for collection, and an EM-CCD for detection (Figure 1.12A). This setup enables simple counting experiments in one color.

Alternating laser excitation with a dual-view CCD. When probing more than one species in the sample, an upgraded setup using two lasers is useful (Figure 1.12B). Here, an alternating laser excitation (ALEX) setup equipped with a dual-view EM-CCD (Andor iXon, DU-897E-CS0-#BV, 512×512 with 16 μm pixels) was constructed by adapting protocols described elsewhere[39,40]. Briefly, two laser beams (638 and 532 nm) were combined using a dichroic mirror, and the intensity of each was modulated by an acousto-optical tunable filter (Gooch & Housego, PCAOM 48058-2.5-.55-5W). The microscope contained a dual-band excitation filter (Chroma, z532/635rpc). The molecules were illuminated in epifluorescence mode with a $60\times$ oil-immersion objective (Olympus, 1-U2B616, N.A. 1.45) mounted on an inverted epifluorescence microscope (Olympus, IX71). Typical illumination intensities were 100 W/cm^2. The fluorescence image exiting the microscope was cropped to half with a slit, and then separated into two channels (red and green) by a dichroic mirror. Each channel was imaged on one half of the CCD detector.

Confocal Dimple Machine

In a confocal fluorescence microscope, an excitation beam is focused using the objective onto a sample located at the front focal plane. Due to the focused excitation, the excitation of molecules outside the focal volume is greatly reduced, leading to a high SNR. In addition, a pinhole located at the image plane on the emission path can further filter the out-of-focus emission from the sample, further rejecting background fluorescence.

Aligning a laser to a dimple. A laser beam through an oil-immersion objective is focused onto the dimple array. A single dimple array is first aligned to the field of view using a manual coarse-positioning stage, and then a single dimple is aligned to the focused beam with the help of CCD using a piezoelectric nanopositioning stage (Thorlabs SCXYZ100). Precise alignment of the laser to the center of a single dimple is critical in the confocal setup for the maximal, unbiased information from the dimple. To do this,

the beam was scanned around a single dimple, fast enough not to photobleach all the trapped fluorophores, but slow compared to the time scale of diffusion, and the fluorescence emission is recorded with an APD. Given that the fluorescent molecules in a dimple are freely diffusing, much faster than the scanning, the point-spread function in this method will be centered at the center of the dimple (Figure 1.13C). After a few steps of feedback, the laser beam is aligned to the center of the dimple with 20 nm accuracy. Finally, the piezo is held still and the fluorescence emission from the target dimple is collected by an APD, after a pinhole filtering background fluorescence. After all fluorophores inside it photobleach, the stage is repositioned to the next dimple and the measurement continues. The dimple array is replenished once after all the dimples in the field of view are examined.
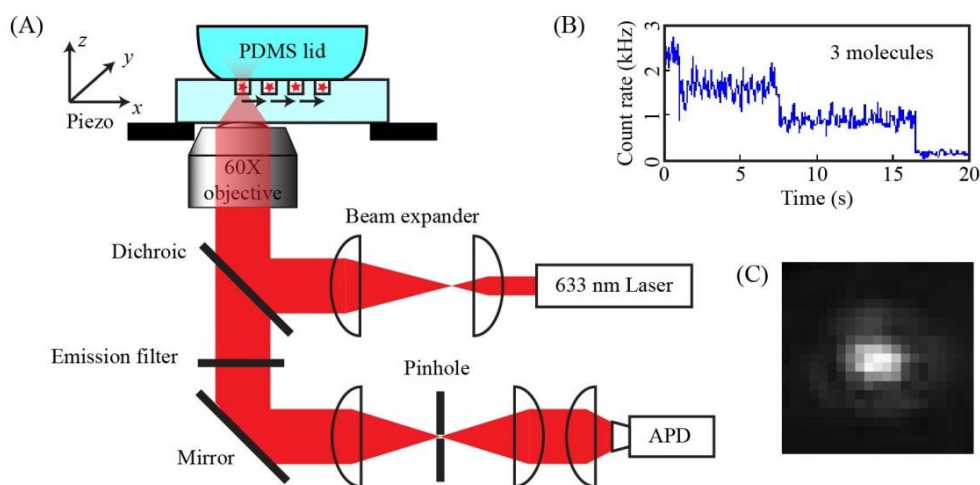
Figure 1.13 Optical setup for the confocal Dimple Machine

(A) Experimental scheme for the confocal Dimple Machine. The confocal Dimple Machine features, in addition to the wide-field imaging setup, a piezoelectric nanopositioning stage to align dimples to a focused beam, and a pinhole for filtering out-of-focus emission to reject background fluorescence from PDMS. APD instead of EM-CCD is used in this setup. (B) Fluorescence emission time trace from a single dimple. The dimple is measured to contain three fluorescently labeled molecules. (C) Point-spread function of a dimple containing fluorescent molecules measured by scanning APD with 633 nm He-Ne laser and a 50 μm pinhole.

This optical setup did improve the SNR, as expected, and made progress towards counting (Figure 1.13B). However, the serial nature of this dimple-by-dimple measurement hampered acquiring a large set of data[*].

Wide-field imaging vs. Confocal scanning

The aspects of these two methods are summarized in Table 1.4. A confocal Dimple Machine is especially suited for applications of which the time scale is below millisecond because the time-resolution of wide-field imaging is inherently limited by the camera's frame rate (> 1 ms). Diffusion of molecules or triplet-state photophysics of fluorophores are examples. On the other hand, due to the serial nature of data acquisition in confocal setup, the overall speed of data accumulation is much slower in confocal scanning than in wide-field imaging. From this point, we focused on developing wide-field imaging.

Table 1.4   Comparison of wide-field imaging and confocal scanning

Aspects	Wide-field	Confocal
Illumination	Expanded beam	Focused beam
Detector	EM-CCD	Single-photon APD
SNR	Lower	Higher
Dynamics	Slow (> 10 ms)	Fast (< 1 ms)
Data throughput	High	Low
Instrumentation	Simpler	Harder

---

[*] After some progress in the confocal setup, we were forced to look back at the wide-field imaging option: the piezo started to malfunction and eventually, it shorted out. Fortunately, with the significant reduction of photobleaching and deduction of background fluorescence in PDMS (Section 1.4.3), we were able to acquire high-SNR data even in wide-field setup.

1.4.3   Trapping

A typical Dimple Machine trapping run proceeded as follows: 50 μL of sample at 2–100 nM was injected into the device; pneumatic actuation caused the lid to close onto the dimples, sealing them hermetically within 2 min; $N_1 = 200$ dimples containing molecules were imaged for 1–5 min; the lid was opened and the contents of the dimples exchanged with the bulk for 1 s; and the cycle was repeated for $N_2 = 200$ times, at a rate of ~10 cycles/h. This experiment generated a dataset consisting of $N_1 \times N_2 = 40,000$ dimples.

Conditioning the device

Nonspecific adsorption of molecules on the fused silica and PDMS surface.   Biomolecules such as DNA and proteins adsorb onto many surfaces, especially on hydrophobic ones. This nonspecific sticking creates background fluorescence that interferes with observations of single molecules. PVP generates a physically adsorbed barrier that prevents nonspecific adsorption of DNA on the fused silica and PDMS[41,42]. Prior to trapping, the sample channel was incubated with 1% PVP for 2 h to minimize adsorption of molecules on the fused silica. The sample channel was then washed with 0.1% PVP multiple times, and briefly degassed in a desiccator. The experimental sample (40 μL) was then injected into the sample channel.

Avoidance of air bubbles in the sample channel.   Application of vacuum to the sample channel induced formation of micro-bubbles in the channel. To avoid bubbles, (1) the sample solution was injected with a micropipette with minimal speed of loading, and (2) the device was degassed for a few minutes in a vacuum desiccator prior to use.

Optimal buffer for trapping

All trapping experiments were carried out in the "trapping buffer" containing 25 mM HEPES at pH 8.0 with 150 mM sodium chloride and with low concentrations of additives to minimize surface effect and improve photostability (Table 1.5).

Table 1.5   Composition of the trapping buffer

Material[a]	Concentration	Role
HEPES	25 mM	Buffer at pH 8.0
NaCl	150 mM	Ionic strength
PVP (MW 10 kDa)	0.1%	Prevents sticking on fused silica
Tween 20	0.1%	Prevents sticking on PDMS
Methyl viologen dichloride	1 mM	Triplet-state quencher (oxidant)
Sodium L-ascorbate	1 mM	Triplet-state quencher (reductant)
Protocatechuic acid	10 mM	Enzymatic deoxygenation (substrate)
Protocatechuate 3,4-dioxygenase	0.1 μM	Enzymatic deoxygenation (enzyme)

[a] All materials are purchased from Sigma-Aldrich.

Suppression of photobleaching

Photobleaching can be suppressed by enzymatic deoxygenation of the solution. We first used PCA/PCD to deoxygenate the sample enzymatically[43] (Table 1.5). However, this approach was not effective because (1) The PCD enzyme was typically at a concentration so low that many dimples contained zero PCD molecules; and (2) Oxygen has high solubility in and permeability through PDMS, so the PDMS lid acted as a large reservoir of oxygen, easily overwhelming the capacity of the oxygen scavengers in the dimples. We improved deoxygenation by combining three approaches (Figure 1.14).

(a) **Enzymatic oxygen scavenging in the microchannels.**   We designed a PDMS lid with microposts. When the lid was closed, the inverted posts on the lid sealed the dimple array, creating microchannels around the array. The channels then irrigated bulk solution near to the dimple array (~100 μm), providing a large sink for oxygen close to the dimples.

(b) **Remote deoxygenation from across the lid membrane.**   We exploited the oxygen permeability of PDMS to deoxygenate the dimples from the top side of the PDMS lid. The reservoir on top of the PDMS lid was loaded with 200 μL of deoxygenation buffer. This reservoir generated a reversed oxygen concentration gradient spanning the lid membrane, causing oxygen to diffuse *out* of the dimples and into the PDMS lid (Table 1.6).

Table 1.6   **Composition of the deoxygenation buffer**

Material[a]	Concentration	Role
HEPES	25 mM	Buffer at pH 8.0
Tween 20	0.1%	Prevents sticking on PDMS
PCA	10 mM	Enzymatic deoxygenation (substrate)
PCD	0.1 µM	Enzymatic deoxygenation (enzyme)

[a] All materials are purchased from Sigma-Aldrich.

(c) **Operation in a nitrogen atmosphere.**   A constant flow of house N_2 was blown into a humidified box covering the device. This physical exclusion of oxygen from the sample chamber prolonged the lifetime of the oxygen scavenger reservoir, facilitating long-term measurements.

In addition to PCA/PCD, we added methyl viologen (1 mM) and ascorbic acid (1 mM) as a redox system quenching the triplet states of fluorescent dyes, and thereby suppressing photoblinking[42].
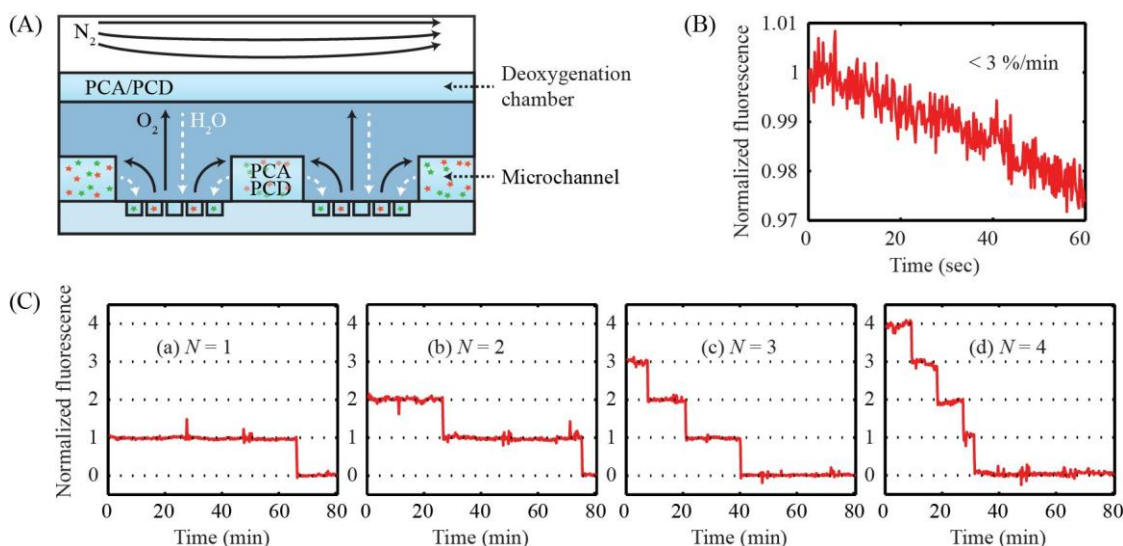
Figure 1.14 Suppression of photobleaching

(A) Scheme for the suppression of photobleaching. The dimples were deoxygenated by three methods: (1) Enzymatic oxygen scavenging in the microchannels; (2) Remote deoxygenation from across the lid membrane; and (3) Nitrogen atmosphere surrounding the device. Note that water molecules can also diffuse through PDMS, indicated by the white dashed arrows. (B) Decay of fluorescence due to photobleaching. The fluorescence is averaged over 100 dimples and 60 cycles. Less than 3% of fluorescence photobleached in 1 min. (C) Prolonged observation of single molecules. Fluorescence intensity traces showing single-step photobleaching for (a) 1, (b) 2, (c) 3, and (d) 4 fluorescent dyes in a single dimple. In these experiments the lid was kept sealed throughout.

Operation of the device

Polyethylene tubing (BD, PE-90) was inserted into the ports of sample channel, and connected to house vacuum via a solenoid valve (Warner, VC-8). The device was placed on a microscope stage and then enclosed in a plastic box containing wet towels to maintain humidity. The box was purged with a constant flow (under 2 scfh) of humidified nitrogen throughout the measurement.

The scheme for pneumatically actuating the PDMS lid was adapted from a publication[32]. Briefly, the lid was actuated by applying vacuum to both ports of the sample chamber. Atmospheric pressure on the top of the lid then caused the lid to bow down until it contacted the silica coverslip, sealing the dimples. We found that it was typically necessary to wait ~5 min between actuation of the vacuum and imaging for the lid to achieve a hermetic seal with the fused silica. Each cycle consisted of 90 s of data acquisition at an exposure time of 50 ms/frame. Red and green laser excitations were applied on alternate frames. The EM-CCD gain was 300. To refresh the dimples, the vacuum was released and the lid returned to its raised position.

Reproducibility of trapping. To achieve reproducible trapping, we found that it was necessary to lower the PDMS lid at the same rate, and with the same force, every time. To achieve this reproducibility, actuation of the lid was controlled by a digital vacuum valve with precise timing to open and close. This feature ensured reproducible repetition of the trapping, producing a large dataset without artifact (Figure 1.16). The lid actuation, alternating laser excitation, and camera exposures were synchronized by a Data Acquisition board (National Instruments, PCIe-6323) run by custom software (LabView, National Instruments).

Storage of the device

After experiments, the Dimple Machine was washed by flowing 0.1% PVP and 0.1 Tween-20 through the sample channel. The washed device was stored in 4 ℃ with 0.1% PVP and 0.02% sodium azide in the sample channel to inhibit the growth of bacteria. It was not necessary to condition the device with 1% PVP again for the next experiment. If needed, the dimple array substrate was detached from the PDMS lid, cleaned in piranha solution, and bonded to the lid again.

1.4.4 Counting

Methods for counting
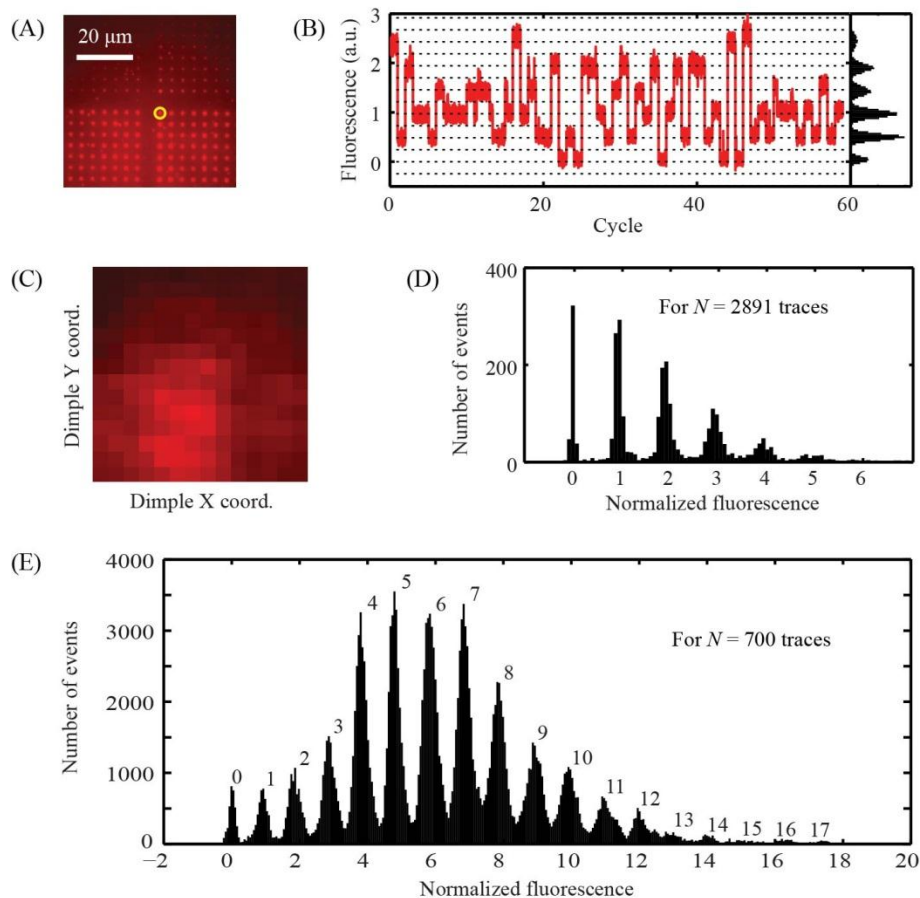
Figure 1.15 Counting of fluorescent dyes in a dimple

(A) Time-average fluorescence image of a dimple array. The intensity of the circled dimple is plotted in (B). (B) Fluorescence time trace of a dimple. The data is concatenated over 60 trapping cycles. Cycles lasted 1 min and were spaced by 5 min. The intensity histogram of the trace is attached on the right. The unit fluorescence intensity from a single dye was obtained from the average spacing of peaks in the histogram. (C) A map of unit fluorescence of a dimple array. The intensity of each pixel represents the unit fluorescence for each dimple shown in (A). The total fluorescence from each dimple was normalized by the corresponding unit fluorescence to measure occupancy. (D) Histogram of normalized fluorescence. The graph is for 2,891 time traces recorded from across the array. (E) Maximum countable occupancy. 30-mer ssDNA labeled with Cy5 (25 nM) in 650 nm radius dimples. The graph is for 7 dimples $\times$ 100 cycles. Intensities were averaged for 1.4 s. Up to ~15 molecules were counted.

The occupancy of dimples, *N*, was measured by the fluorescence intensity (Figure 1.15)[*]. First, the unit fluorescence of a single dye was assessed from the spacing of evenly spaced peaks in the fluorescence intensity histogram (Figure 1.15B). The occupancy was obtained by dividing the total fluorescence from a dimple by this unit and rounding to the nearest integer. The well-resolved peaks in the intensity histogram indicate that this procedure is robust. This calibration was performed separately for each dimple to correct for small variations in laser illumination intensity and collection efficiency (Figure 1.15C). The maximum countable occupancy was ~15 molecules/dimple (Figure 1.15E).

Verification of the device

To validate the device we ran several tests with 30-mer ssDNA oligos labeled with Cy5. Occupancy varied between dimples within a trapping cycle, and within each dimple over multiple trapping cycles, but not within a single dimple during a single trapping cycle (except for slight photobleaching at 3%/min), thus establishing that molecules were completely sealed within the dimples.

Heterogeneity of the dimples. There were negligible differences in mean occupancy between dimples of the same nominal size, thus ruling out static heterogeneity due to variations in nanofabrication. The occupancy of each dimple was averaged over $X = 60$ trapping cycles to calculate $\langle N(k,x)\rangle_x$. The histogram in Figure 1.16A shows the distribution (over the $K = 50$ dimples) of $\langle N(k,x)\rangle_x$. Mean occupancy of all dimples was $\langle N(k,x)\rangle_{k,x} = 1.26$, with standard deviation of $\langle N(k,x)\rangle_x$, $\sigma_X = 0.16$. From Poisson
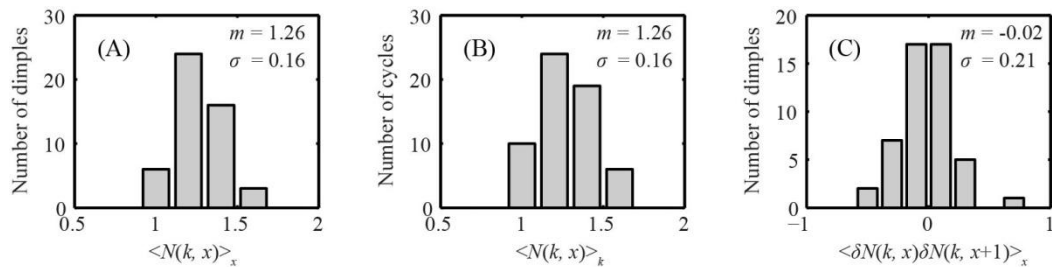
Figure 1.16 Reproducible filling of dimples

The quantity $N(k,x)$ represents the occupancy of the *k*-th dimple in the *x*-th cycle of trapping. A sample of Cy5-labeled 30-mer ssDNA at 8.4 nM was trapped in dimples of radius 550 nm. 50 dimples were studied for 60 cycles. (A) Occupancy distribution for individual dimples averaged over cycles. (B) Occupancy distribution for individual cycles averaged over dimples. (C) Correlation in the single-dimple occupancy over successive cycles.

---

[*] Data was analyzed with custom software written in MATLAB (R2011a, MathWorks).

statistics, one expects the standard deviation in occupancy on a single trial to be $\sigma_1 = \langle N(k,x) \rangle_x$. From the central limit theorem, the standard deviation in mean occupancy averaged over X cycles should be $\sigma_X = \sigma_1/\sqrt{X}$, yielding a predicted $\sigma_X = 0.163$, consistent with the observation.

Heterogeneity of the trapping cycles. There were no long-term drifts in the mean dimple occupancy over many trapping cycles, thus ruling out evaporation or adsorption as causes of long-term instability. The occupancy of the complete array was averaged over $K = 50$ dimples to calculate $\langle N(k,x) \rangle_k$. The histogram in Figure 1.16B shows the distribution (over the $X = 60$ cycles) of $\langle N(k,x) \rangle_k$. Mean occupancy of all dimples was $\langle N(k,x) \rangle_{k,x} = 1.26$, with standard deviation of $\langle N(k,x) \rangle_k$, $\sigma_K = 0.16$. The standard deviation in mean occupancy averaged over K dimples should be $\sigma_K = \sigma_1/\sqrt{K}$, yielding $\sigma_K = 0.178$, consistent with the observation.

Molecular sticking. Finally, the occupancy of each dimple was uncorrelated between measurement cycles, thus ruling out artifacts from sticking of molecules to the walls of the dimple or the PDMS lid. We calculated the correlation of the occupancy of dimple k at cycles x and $x + 1$, averaged over all x (Figure 1.16C). The distribution of correlations (calculated separately for $K = 50$ dimples) is centered on zero, indicating that the loading of the dimples was uncorrelated between successive cycles. This result confirms complete interchange of dimple contents during each refresh cycle.

Poissonian occupancy of dimples

Dimple occupancy, N, was Poisson distributed with mean, $\langle N \rangle \sim cV_d$ where c is the concentration in bulk and V_d is the volume of a dimple (Figure 1.17). For each experiment we adjusted c to achieve a desired $\langle N \rangle$. These results established that the Dimple Machine reversibly encapsulated molecules in well-defined volumes, without strong surface interactions.
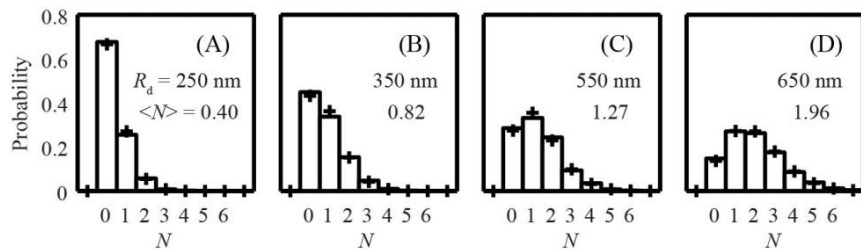
Figure 1.17 Occupancy distribution of the dimples

The sample concentration was 8.4 nM for all. R_d: Radius of the dimples; $\langle N \rangle$: Mean occupancy.

1.5 Application I: Hybridization of DNA

1.5.1 Introduction

We used a Dimple Machine to study the fundamental chemistry of a simple bimolecular reaction in confinement. Two strands of single-stranded DNA (ssDNA) labeled with fluorescent dyes were trapped together in the dimples and their hybridization was monitored by colocalization and by fluorescence resonance energy transfer (FRET). In each trapping cycle, there were small-number fluctuations in the number of DNA molecules in each dimple.

1.5.2 Measurement of hybridization equilibrium

Assortment of species in dimples

Consider the following reaction:

$$R + G \rightleftarrows RG \tag{8}$$

where R and G are any two species, each labeled with a single red or green dye. The fraction of molecules in the dimerized RG state is governed by the dissociation constant, K_d. Suppose molecules from a solution of R and G are trapped in the dimples and the total numbers of red and green dyes ($N_R^{(T)} = N_R + N_{RG}$ and $N_G^{(T)} = N_G + N_{RG}$) are counted in each dimple. If R and G do not interact, then the distributions of $N_R^{(T)}$ and $N_G^{(T)}$ will be statistically independent. If R and G are fused or interact very strongly, then the distributions of $N_R^{(T)}$ and $N_G^{(T)}$ will be highly correlated. For an intermediate strength interaction, R and G will colocalize more often than one would expect from chance, but not perfectly.

To test this, three sets of fluorescently labeled ssDNA oligos were purchased (Integrated DNA Technologies): a non-complementary pair, a doubly labeled hairpin, and a hybridizing pair (Table 1.7).

Table 1.7   DNA sequences used in the Dimple Machine experiments

Linkage	Sequence	Length (bp)
None	R: 5'-/Cy5/-TCT AGT CTC CCC AAA AAA AAA AAA AAA AAA-3'	30
	G: 5'-ATG TCT GAC GCT GGC ATT CGC ATC AAA GGA-/Cy3/-3'	30
Covalent	RG: 5'-GCA ATT TAT TAA TTA TAT ATT TTA TTT AAT ATA ATT/Alexa647/ CCT GGA TCC GCA AGC TGG CGT TTA GTG ATA TCC CGT ATA AGT CTG TAG TGA ATT CTC C/Cy3B/TA TTA TAT TAA ATA AAA TAT ATA ATT AAT AAA TTG C-3'	130
Hybridization	R: 5'-/Cy5/-TCT AGT CTC CCC AAA AAA AAA AAA AAA AAA-3'	30
	G: 5'-/Cy3/-AGA CTA GAC CCC AAA AAA AAA AAA AAA AAA-3'	30

The ssDNA oligo R of the hybridization pair was used in the proof-of-principle occupancy measurement in Section 1.4.4.

Case 1: Independent oligos

We tested the correlated occupancy method in three DNA constructs. In the first, we mixed two non-complementary ssDNA strands, one labeled with Cy3 and the other with Cy5. The 2-D histogram of red and green fluorescence (R-G histogram, Figure 1.18A) showed peaks around integer occupancy of each dimple. By eye, the red and green distributions look independent. We tested for independence by comparison to the theoretically predicted joint probability distribution.
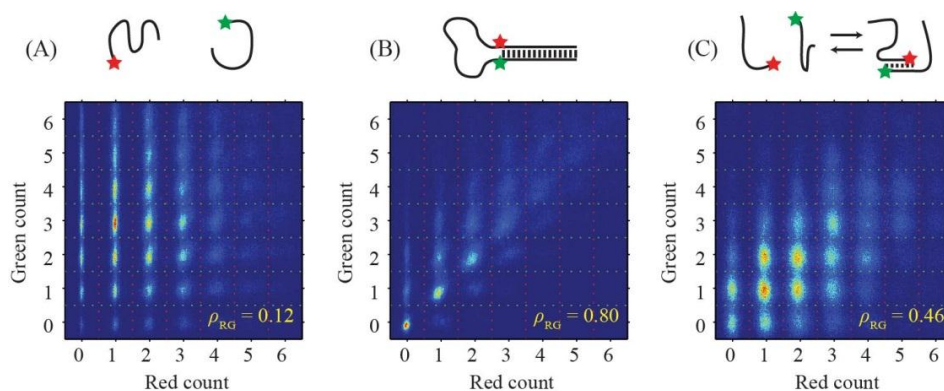
Figure 1.18 Molecular affinity probed by joint occupancy

(*Top*) Cartoon of DNA interactions with (A) no, (B) strong, and (C) weak affinity. (*Bottom*) Experimental red-green (R-G) histograms of joint occupancy. The procedure for converting raw movies into R-G histograms is described in Figure 1.19.

Case 2: Covalently-linked oligos

In the second test, we made a hairpin construct doubly labeled with one red dye (Alexa Fluor® 647) and one green dye (Cy3B). Due to efficient FRET from the green to the red dye, the number of green fluorophores per dimple was estimated by exciting with green light and summing the fluorescence from the red and green channels. Here the joint distribution was strongly peaked along the diagonal, $N_R^{(T)} = N_G^{(T)}$, as one would expect (Figure 1.18B). We attribute the weak off-diagonal peaks to imperfect labeling. Indeed, this measurement lets us estimate the labeling efficiencies, which were 89% with Alexa647 and 72% with Cy3B.

Case 3: Complementary oligos

The third sample contained two ssDNA oligos of length 30 bp, with an 8-bp complementary region at their 5' termini (Figure 1.18C). The oligos were labeled with Cy3 and Cy5, respectively, on their 5' ends. The dimerized state showed efficient FRET. As in the case of the hairpin, we estimated the number of Cy3 molecules by summing the red and green emission under green excitation. As expected from the weak association through base pairing, the correlation in the joint occupancy was intermediate between the two extremes. We quantified the red-green correlation by calculating correlation coefficients (σ_{RG}) (Table 1.8) and from this we calculated $K_d = 63 \pm 12$ nM.

Note that determination of K_d via correlated occupancy does not rely on FRET. This procedure is expected to work well for dimple occupancies small enough that the occupancy can be counted. We readily count more than 10 fluorophores of each color, corresponding to molecular concentrations up to ~10 μM. This concentration sets the upper bound on K_d that can be measured by this technique, which is much higher than the maximum K_d that can be measured by fluorescence cross-correlation spectroscopy[44].

Analysis of correlation in occupancy

Three sets of fluorescence time traces were extracted: (a) $D(t)$: green emission under green excitation; (b) $A(t)$: red emission under green excitation; and (c) $R(t)$: red emission under red excitation. The fluorescence intensity from each dimple was extracted from the 7×7 pixels (typical) centered on the dimple, and the background fluorescence estimated from neighboring pixels was subtracted from the dimple intensity. Based on the camera counts, exposure, time, and EM-CCD gain, we estimate photon

detection rates of 400 photons/s from Cy5 with a background rate of 1,000 photons/s. For Cy3 the signal rate was 300 photons/s and the background rate was 4,000 photons/s. To estimate the occupancy by red molecules, we looked at $R(t)$; to estimate the occupancy by green molecules, we looked at $G(t) = D(t) + A(t)$. The occupancy was measured by counting the number of fluorescent dyes as described in Figure 1.15. A 2-D histogram of red and green fluorescence (R-G histogram) was constructed in a similar way to Figure 1.15, but with two traces $R(t)$ and $G(t)$ (Figure 1.19).
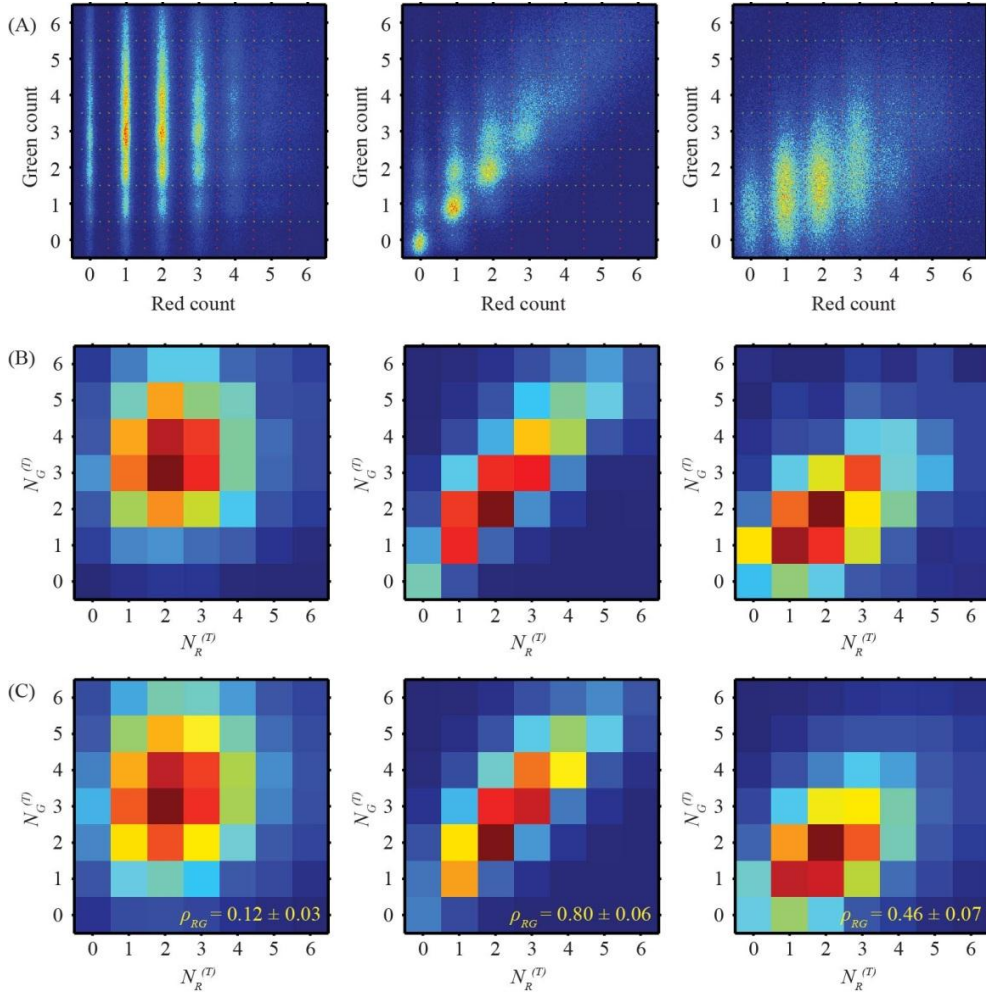
Figure 1.19 Measurement of K_d from correlated occupancy

Non-complementary (*left*), covalently linked (*center*), and hybridizing (*right*) ssDNA pairs. (A) R-G histogram of the unfiltered raw fluorescence. The R-G histograms shown in the main text were obtained from the raw fluorescence traces by application of a median filter running over 13 frames. (B) R-G histogram of the rounded fluorescence. The mean normalized fluorescence from each dimple in each cycle was rounded to the nearest integer value, to provide an estimate of occupancy. (C) Correlated bivariate Poisson fit to the R-G histograms in (B). Fitting parameters are given in Table 1.8.

1.5.3   Correlated bivariate Poisson distribution

Mathematically, the probability distribution of joint occupancy, $P\left(N_R^{(T)}, N_G^{(T)}\right)$ is described by a correlated bivariate Poisson distribution, whose parameters are related to the concentrations [R], [G], and [RG] in bulk. When a mixture of R, G, and RG is trapped in dimples, each species assorts independently, following its own Poisson distribution:

$$f_R(N) = \frac{(\lambda_R)^N e^{-\lambda_R}}{N!}, f_G(N) = \frac{(\lambda_G)^N e^{-\lambda_G}}{N!}, \text{and } f_{RG}(N) = \frac{(\lambda_{RG})^N e^{-\lambda_{RG}}}{N!} \tag{9}$$

where λ_R, λ_G, and λ_{RG} are the average occupancy of dimples by R, G, and RG, respectively. Consider a dimple with a joint occupancy $\left(N_R^{(T)}, N_G^{(T)}\right)$. If there are N_{RG} molecules of RG in this dimple, the occupancy by monomeric R and G are $N_R = N_R^{(T)} - N_{RG}$ and $N_G = N_G^{(T)} - N_{RG}$, respectively. The probability of the joint distribution is

$$P\left(N_R^{(T)}, N_G^{(T)}\right) = \sum_{N_{RG}=0}^{N_{RG}^{max}} f_R\left(N_R^{(T)} - N_{RG}\right) f_G\left(N_G^{(T)} - N_{RG}\right) f_{RG}(N_{RG}). \tag{10}$$

Plugging in Eq. (10) into Eq. (9) results in the following expression:

$$P\left(N_R^{(T)}, N_G^{(T)}\right) = e^{-(\lambda_R + \lambda_G + \lambda_{RG})} (\lambda_R)^{N_R^{(T)}} (\lambda_G)^{N_G^{(T)}} \left(-\frac{\lambda_R \lambda_G}{\lambda_{RG}}\right)^{-N_G^{(T)}} U\left(-N_G^{(T)}, 1 - N_G^{(T)} + N_R^{(T)}, -\frac{\lambda_R \lambda_G}{\lambda_{RG}}\right) \tag{11}$$

where U represents the Tricomi confluent hypergeometric function:

$$U(a, b, z) = \frac{1}{\Gamma(a)} \int_0^\infty e^{-zt} t^{a-1} (1 + t)^{b-a-1} dt. \tag{12}$$

Eq. (11) serves as a model for the joint distribution with three fitting parameters λ_R, λ_G, and λ_{RG}. We fit the experimental R-G histogram to Eq. (11) using maximum likelihood estimation in Matlab. The error bars represent the 95% confidence intervals determined by the Matlab measure of goodness of fit. The correlation coefficient σ_{RG} between R and G is obtained by

$$\sigma_{RG} = \frac{\lambda_{RG}}{\sqrt{(\lambda_R + \lambda_{RG})(\lambda_G + \lambda_{RG})}}. \tag{13}$$

The fractions of species at equilibrium in bulk can be inferred from the average occupancy of dimples:

$$K_d = \frac{[R]_{eq}[G]_{eq}}{[RG]_{eq}} = \frac{\left(\lambda_R/(N_A V_d)\right)\left(\lambda_G/(N_A V_d)\right)}{\lambda_{RG}/(N_A V_d)}. \tag{14}$$

Fitting this model to the measured distribution of occupancy gives an estimate for K_d (Table 1.8).

Table 1.8   Fitting parameters for a correlated bivariate Poisson model

Linkage	None	Covalent	Hybridization
λ_R	2.21 ± 0.11	0.31 ± 0.04	1.39 ± 0.13
λ_G	3.43 ± 0.12	0.96 ± 0.05	1.09 ± 0.14
λ_{RG}	0.39 ± 0.10	2.50 ± 0.07	1.07 ± 0.13
σ_{RG}	0.12 ± 0.03	0.80 ± 0.06	0.46 ± 0.07
K_d (nM)	900 ± 200	1.10 ± 0.15	63 ± 12

1.5.4   Comparison to bulk measurement

The measurement of K_d by correlated occupancy method agreed well with a bulk titration in a fluorimeter (57 ± 12 nM, Figure 1.20) and with a theoretical prediction[*] (44–110 nM at 17–20 ℃). The following describes the method for measuring K_d in bulk.

Experimental procedure

Equimolar mixtures of hybridizing ssDNA oligos were prepared at various concentrations from 2 nM to 2 μM in HEPES buffer at pH = 8.0 with 150 mM NaCl. The fluorescence emission spectra of the mixture were measured in a fluorimeter (Cary Eclipse, Agilent) exciting the sample at 550 nm, collecting the emission from 550 nm to 750 nm (Figure 1.20A). The emission intensity at 670 nm was selected as a value representing the intensity of FRET acceptor emission and plotted against concentrations (Figure 1.20B).

Analysis: Fraction of dimer in a binary mixture

When R and G associate in a mixture, they exist in equilibrium with the bound form, RG (Eq. (8)), with the relative fraction of each species determined by the dissociation constant K_d:

---

[*] This prediction was made with the DINAMelt Web Server[97] at: http://mfold.rna.albany.edu/?q=DINAMelt.

$$K_{\mathrm{d}} = \frac{[R]_{eq}[G]_{eq}}{[RG]_{eq}} = \frac{\big([R]_0 - [RG]_{eq}\big)\big([G]_0 - [RG]_{eq}\big)}{[RG]_{eq}} \tag{15}$$

where $[R]_{eq}$, $[G]_{eq}$, and $[RG]_{eq}$ are the equilibrium concentrations of R, G, and RG, respectively, and $[R]_0$ and $[G]_0$ are the initial concentrations of R and G, respectively. Solving Eq. (15) for $[RG]_{eq}$ as a function of $[R]_0$, $[G]_0$, and K_{d} gives

$$[RG]_{eq} = \frac{1}{2}\Big([R]_0 + [G]_0 + K_{\mathrm{d}} - \sqrt{([R]_0 + [G]_0 + K_{\mathrm{d}})^2 - 4[R]_0[G]_0}\Big). \tag{16}$$

In our study, the FRET efficiency is low when R is unbound, and high when bound to G. If the acceptor emission intensity is I_{low} in R and I_{high} in RG, the average acceptor intensity I_A is

$$\langle I_A \rangle = \left(\frac{[R]_{eq}}{[R]_0}\right)I_{\mathrm{low}} + \left(\frac{[RG]_{eq}}{[R]_0}\right)I_{\mathrm{high}} = I_{\mathrm{low}} + \left(\frac{[RG]_{eq}}{[R]_0}\right)\big(I_{\mathrm{high}} - I_{\mathrm{low}}\big). \tag{17}$$

Substituting Eq. (16) into Eq. (17) gives a model for the acceptor emission. This model was fit to the experimental curve to obtain K_{d} (Figure 1.20).
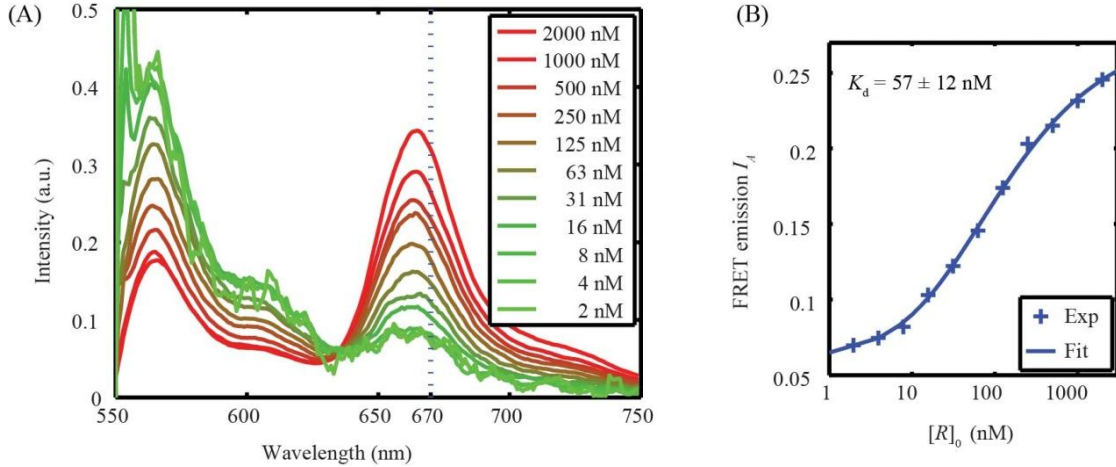
Figure 1.20 Bulk measurement of K_{d}
 (A) Fluorescence emission spectra of the hybridizing ssDNA pair mixtures. The spectra are measured in a fluorimeter at the excitation wavelength of 550 nm at various initial concentrations (legend). The dashed line (emission at 670 nm) indicates the wavelength at which the FRET acceptor emission is taken. (B) FRET acceptor emission intensity as a function of initial concentration of DNA, $[R]_0$. The K_{d} extracted from the curve was 57 ± 12 nM. (*Exp*): Experimental data; (*Fit*): Fitted curve.

1.6 Application II: Reactions in Nano-Confinement

1.6.1 Introduction

Many biochemical reactions take place within the confines of membrane-bound structures. When small numbers of molecules are present, stochastic fluctuations in molecule number play a significant role in determining reaction outcomes[45–51]. The importance of these fluctuations increases as the order of the reaction increases and as the absolute number of molecules decreases. We asked, "How do statistical fluctuations in occupancy affect the thermodynamics and kinetics of reactions in confinement?"

Confinement has previously been used in single-molecule studies, but under conditions where the confined region was large compared to the optical wavelength, or where the confinement was in self-assembled structures lacking precisely defined sizes and locations[8–10,12,14,15,20–33]. Here we achieved sufficiently tight confinement that (a) the radius of confinement was small compared to the mean separation of reactant molecules in bulk solution, and (b) the radius of confinement was small enough that all possible pairwise intermolecular collisions occurred on an experimentally accessible timescale. This qualitatively new regime led to several apparent deviations from the Law of Mass Action, which are reconciled by a statistical description of reactivity in confinement. We found that confinement rectified these fluctuations, leading to dimple-to-dimple fluctuations in equilibria and rate constants. The observations are quantitatively explained by a modification to the Law of Mass Action to incorporate local concentration fluctuations.

1.6.2 Measurements of reaction in dimples

Alternating laser fluorescence measurements[39] determined the complete time-dependent reaction state within each dimple: (a) red emission under red excitation indicated the total number of red dyes ($N_R + N_{RG}$); (b) red emission under green excitation indicated the number of dye pairs capable of undergoing FRET (N_{RG}); and (c) green emission under green excitation indicated the number of green dyes not quenched by a red acceptor (N_G). We observed that the reaction thermodynamics and kinetics varied with dimple occupancy and size, even for identical bulk concentrations of reactants. When analyzing FRET, a

2-D histogram of donor and acceptor fluorescence (D-A histogram) was constructed similarly using $D(t)$ and $A(t)$. Data traces in which we observed a photobleaching event were excluded from kinetic or thermodynamic analysis[39].

1.6.3   Thermodynamics in dimples

Effects of occupancy

We examined the effect of occupancy on reaction thermodynamics. Fluorescence time traces were first categorized by $\left(N_{\mathrm{R}}^{(T)}, N_{\mathrm{G}}^{(T)}\right)$ with the integers $N_{\mathrm{R}}^{(T)}$ and $N_{\mathrm{G}}^{(T)}$ representing the total numbers of red and green strands, irrespective of hybridization state (Figure 1.21A). For each occupancy, we then studied the distribution of dimers, $P(N_{\mathrm{RG}})$. We excited with green light, and made a 2-D histogram of green and red emission, indicating donor and acceptor fluorescence (D-A histogram). Figure 1.21B–E show these histograms for the cases $N_{\mathrm{R}}^{(T)} = N_{\mathrm{G}}^{(T)}$, though the analysis is not restricted to symmetric occupancy. The D-A histogram clearly resolved multiple states of reaction corresponding to distinct numbers of dimers. The maximum number of dimers varied with dimple occupancy according to $N_{\mathrm{R}}^{max} = \min\left(N_{\mathrm{R}}^{(T)}, N_{\mathrm{G}}^{(T)}\right)$ as expected.
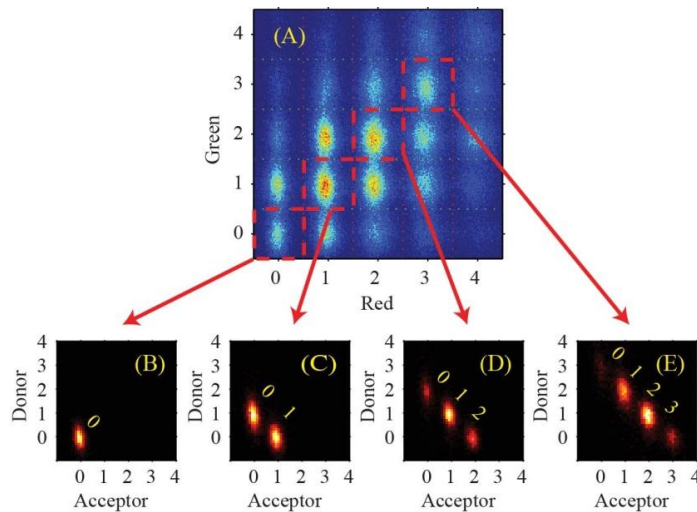
Figure 1.21 Thermodynamics of hybridization in confinement

(A) Red-Green histogram showing correlated occupancy of dimples, as expected from a weak association of R and G in bulk. (B–E) Donor-Acceptor histogram indicating probability distribution of RG pairs, $P(N_{\mathrm{RG}})$, for different dimple occupancies, $\left(N_{\mathrm{R}}^{(T)}, N_{\mathrm{G}}^{(T)}\right)$, of (B) (0, 0), (C) (1, 1), (D) (2, 2), and (E) (3, 3).

The relative intensities of the peaks in the D-A histogram gave the distribution, $P(N_{RG})$. Figure 1.22 shows the probability distribution $P(N_{RG})$ for dimples of the same size ($R_d = 250$ nm), but different occupancy. The reaction equilibrium shifted toward the dimer at higher occupancy (compare $\left(N_R^{(T)}, N_G^{(T)}\right) = (1, 1)$, $(1, 2)$, and $(1, 3)$; or $(2, 2)$ and $(2, 3)$). Note that these data were all taken at the same nominal bulk ssDNA concentration, 30 nM. The variations in equilibrium were purely due to small-number fluctuations in occupancy. Other sizes of dimples ($R_d = 150$, 450, and 550 nm) showed the same trend.

The shift in equilibrium is easily explained if one invokes the local concentration of each species in the dimple, rather than the bulk concentration. We define the local concentration (c_{local}) of each species as:

$$c_{local} = \frac{N}{N_A V_d} \tag{18}$$

where N is the number of molecules, N_A is Avogadro's number, and V_d is the volume of a dimple. The mean number of dimers per dimple is then given by the usual equilibrium expression.

Within each dimple we obtain the distribution, $P(N_{RG})$, not just its mean. This distribution can be simulated by modeling the reaction in the dimple as a finite-state Markov process:

$$\dot{\mathbf{P}} = \mathbf{MP} \tag{19}$$

where $\mathbf{P} = P(N_{RG})$ describes the state of the system and $\mathbf{M}$ is a kinetic matrix. The dimension of $\mathbf{P}$ is $N_{RG}^{max} + 1$. The form of $\mathbf{M}$ depends on dimple size and occupancy, $\left(N_R^{(T)}, N_G^{(T)}\right)$. Details of construction of $\mathbf{M}$ are given in Section 1.6.5.
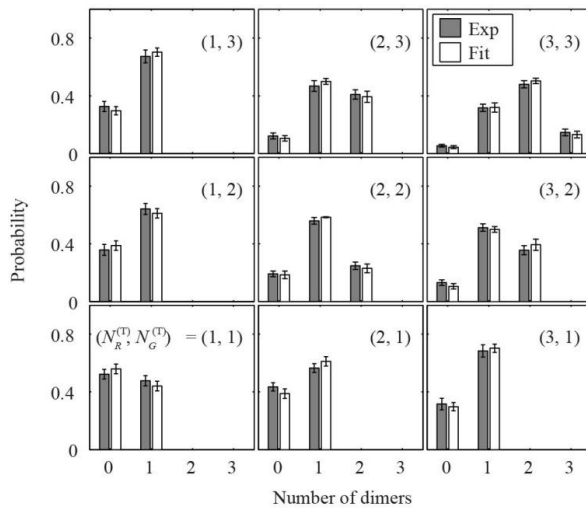
Figure 1.22 The distribution of dimers as a function of joint occupancy

(*Exp*): Measured distribution; (*Fit*): Fit to Markovian reaction model.

Solving Eq. (19) for $\dot{\mathbf{P}} = 0$ yields equilibrium distributions $P(N_{\mathrm{RG}})$ in quantitative agreement with experiment. This model has only a single fitting parameter, K_{d}. Applying a global fit to all occupancies yielded $K_{\mathrm{d}} = 56 \pm 4$ nM ('Fit' of Figure 1.22). This value agreed with the previous measurements of K_{d} on this sample (Table 1.9). The fact that a single value K_{d} of can describe the equilibrium for all occupancies implies that the occupancy did not affect the free energies of molecules, but tipped the balance of reaction by changing c_{local}.

Effects of dimple size

To see the effect of dimple size on equilibrium, the dimer distributions in different dimples were compared at the same occupancy (Figure 1.23). For a given occupancy, smaller dimples had higher dimer concentration. This trend can be explained again by the change in c_{local}, with smaller dimples having higher c_{local} when occupied, and thus the equilibrium shifted toward the product.

The K_{d}'s for all dimple sizes were comparable (Table 1.9). This result confirms that the apparent shift in equilibrium is due to rectification of small-number fluctuations, not a change in the intrinsic nature of the hybridization. A relatively large K_{d} in the smallest dimples ($R_{\mathrm{d}} = 150$ nm) might be due to surface interactions reducing the effective concentration.
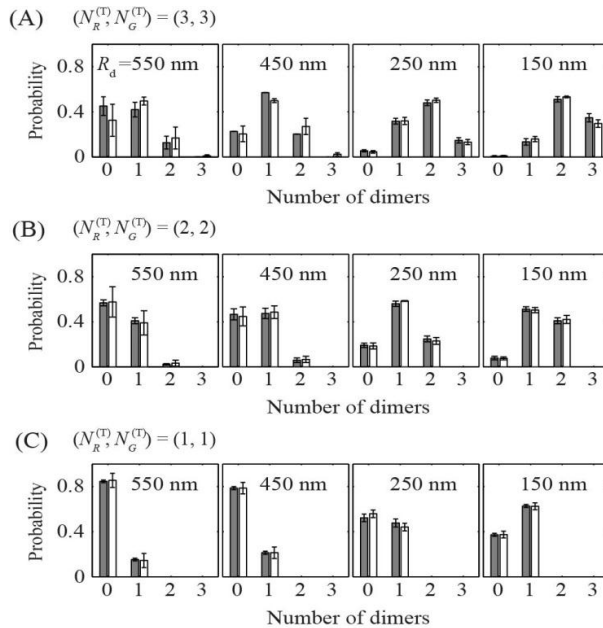
Figure 1.23 Effect of dimple size on the reaction equilibrium

The distribution of dimers as a function of dimple size at the joint occupancy as annotated.

1.6.4   Kinetics in dimples

Effects of occupancy and dimple size

We next examined the effects of confinement on reaction kinetics. The fluorescence traces showed clear stepwise changes in FRET corresponding to single association and dissociation events (Figure 1.24). The intensity of acceptor fluorescence was a direct indicator of the number of dimers.

We studied the autocorrelation of acceptor fluorescence:

$$C_{AA}^{(2)}(\tau) = \langle \delta A(t) \delta A(t+\tau) \rangle_t \tag{20}$$

where $\delta A(t) = A(t) - \langle A(t) \rangle_t$ is the deviation of acceptor fluorescence at time t from average. The autocorrelation function was different for different dimple occupancies and dimple sizes (Figure 1.25).

We used the kinetic model of Eq. (20) to simulate these autocorrelation functions as follows. Integration of Eq. (19) yields

$$\mathbf{P}(t) = \mathbf{G}(t|t_0)\mathbf{P}(t_0) \tag{21}$$

where $\mathbf{G}(t|t_0) = \exp[\mathbf{M}(t - t_0)]$. The autocorrelation function is then

$$C_{AA}^{(2)}(\tau) = \left[\sum_{N_i,N_f=0}^{N_{RG}^{max}} N_f \mathbf{G}(\tau|0) N_i \mathbf{P}_{eq}(N_i) \right] - \langle N_{RG} \rangle^2 \tag{22}$$
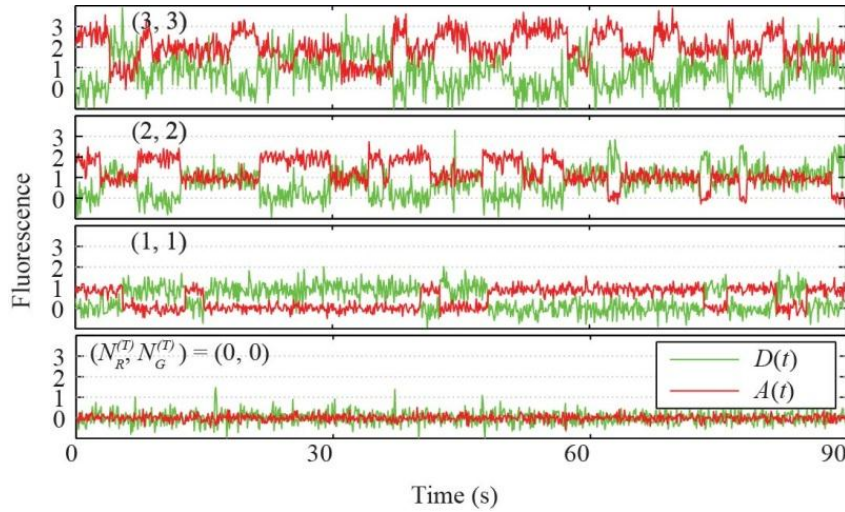
Figure 1.24   FRET traces revealing reactions in dimples

Fluorescence time traces monitoring hybridization in dimples with different occupancies.

where $\mathbf{P}_{eq}$ is the equilibrium probability distribution. This model quantitatively reproduces the amplitude and timescale of the measured autocorrelation, both as a function of dimple occupancy and size.

We performed a global fit of Eq. (22) to the autocorrelation decays at all occupancies (Section 1.6.5) and obtained values for the rate constants, k_{on} and k_{off}, that were consistent with all the data (Table 1.9).

Table 1.9   Reaction constants for DNA hybridization in dimples

R_d (nm)	Bulk	550	450	250	150
K_d (nM)	63 ± 12^a, 57 ± 12^b	54 ± 3	51 ± 4	56 ± 4	74 ± 4
k_{on} (10^6 M^{-1}s^{-1})		1.27 ± 0.04	1.18 ± 0.07	1.09 ± 0.09	0.77 ± 0.07
k_{off} (10^{-2} s^{-1})		6.88 ± 0.06	5.96 ± 0.07	6.15 ± 0.08	5.70 ± 0.11

[a] Measured from the correlated occupancy on dimples with $R_d = 250$ nm. (Section 1.5.2, Figure 1.19).
[b] Measured in a fluorimeter (Section 1.5.4, Figure 1.20).

The autocorrelation decayed more quickly for smaller dimples or higher occupancy. Both effects arise from the increased c_{local} in these conditions, and thus an increased association rate. The dissociation rate, k_{off}, was independent of dimple size or occupancy.
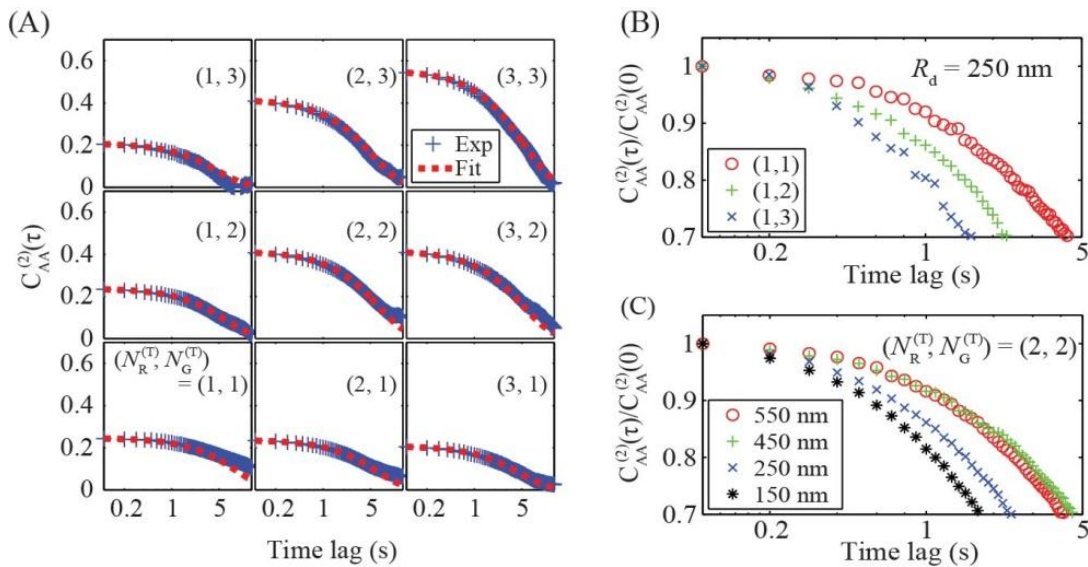
Figure 1.25   Kinetics of hybridization in confinement

(A) Autocorrelation of acceptor fluorescence as a function of occupancy. (B) The effect of occupancy on the rates of reaction. (C) The effect of dimple size on the rates of reaction. The autocorrelations in (B) and (C) are normalized to unity at zero lag.

1.6.5   Theory of multi-state Markov process

Steady-state distributions

Consider a dimple with a joint occupancy $\left(N_R^{(T)}, N_G^{(T)}\right)$ in which R and G associate and dissociate with rate constants k_{on} and k_{off}, respectively. Assuming that the reaction is Markovian, the number of dimers at time t, $N_{RG}(t)$ can be considered as a state variable whose path is determined by the kinetic matrix $\mathbf{M}$ with the element m_{ij} representing the transition rate from state j to state i:

$$m_{ij} = \lim_{\Delta t \to 0} \frac{P[N_{RG}(t + \Delta t) = i | N_{RG}(t) = j] - \delta_{ij}}{\Delta t} \quad (i, j = 0, 1, \dots, N_{RG}^{max}) \tag{23}$$

where N_{RG}^{max} is the maximum number of RG given by $\min\left(N_R^{(T)}, N_G^{(T)}\right)$. Note that to avoid confusion, the matrix indices i and j start from zero. Only certain elements of the rate matrix are nonzero. These are:

$$m_{(i+1)i} = k_{on}[R][G] = k_{on} \frac{N_R}{N_A V_d} \frac{N_G}{N_A V_d} = k_{on} \frac{(N_R^{(T)} - i)}{N_A V_d} \frac{(N_G^{(T)} - i)}{N_A V_d} \quad (i = 0, 1, \dots, N_{RG}^{max} - 1) \tag{24}$$

$$m_{i(i+1)} = k_{off}[RG] = k_{off} \frac{N_{RG}}{N_A V_d} = k_{off} \frac{i+1}{N_A V_d} \quad (i = 0, 1, \dots, N_{RG}^{max} - 1) \tag{25}$$

$$m_{ii} = -\sum_{j \neq i} m_{ji} = -m_{(i+1)i} - m_{(i-1)i} \tag{26}$$

where N_A is Avogadro's number, and V_d is the volume of the dimple. All other elements of $\mathbf{M}$ are zero.

To calculate the steady state probability distribution, we apply the condition of detailed balance between state j and $j+1$:

$$m_{j(j+1)} P_{j+1} = m_{(j+1)j} P_j. \tag{27}$$

Applying this condition recursively from P_0 yields

$$P_i = \left(\prod_{j=0}^{i-1} \frac{m_{(j+1)j}}{m_{j(j+1)}} \right) P_0 \quad (i = 1, 2, \dots, N_{RG}^{max}). \tag{28}$$

Substituting Eqs. (24) and (25) into Eq. (28) gives an expression for the steady-state distributions:

$$P_i = \frac{N_R^{(T)}! \, N_G^{(T)}!}{i! \left(N_R^{(T)} - i\right)! \left(N_G^{(T)} - i\right)!} \left(\frac{k_{on}}{N_A V_d k_{off}}\right)^i P_0. \tag{29}$$

Applying the condition $\Sigma P_i = 1$ yields:

$$\overline{P_i} = \frac{P_i}{\sum_j P_j}.$$

(30)

Eq. (29) gives a model for the distribution of RG with one fitting parameter, $K_d = k_{off}/k_{on}$. We estimated K_d for each size of dimples, taking the data for low joint occupancy into account, by maximum likelihood estimation in Matlab. Error bars represent the 95% confidence intervals determined by the Matlab measure of goodness of fit.

Eq. (29) can also be derived from equilibrium statistical mechanics as $P_i/P_0 = (g_i/g_0)\exp(-i\Delta G/k_BT)$, where g_i is the degeneracy of state i and $i\Delta G$ is the free energy to form i molecules of product.

An important feature of Eq. (29) is that the steady-state distribution of dimer depends not only on the reaction equilibrium ($K_d = k_{off}/k_{on}$), but also on the dimple volume and on the stochastically determined occupancy.

Autocorrelations

The second-order autocorrelation, $C^{(2)}(\tau)$ of the state variable $i = N_{RG}(t)$ is predicted by summing the conditional probabilities of $N_{RG}(t)$ for the two time points separated by τ:

$$C^{(2)}(\tau) = \left(\sum_{j=0}^{N_{RG}^{max}} jP[N_{RG}(t) = j|N_{RG}(0) = i]\right)\left(\sum_{i=0}^{N_{RG}^{max}} iP[N_{RG}(0) = i]\right) - \langle N_{RG}\rangle^2$$

(31)

$$= \mathbf{1N}e^{\mathbf{M}\tau}\mathbf{NP}_{eq} - \left(\mathbf{1NP}_{eq}\right)^2$$

(32)

where $\mathbf{N}$ is a $(N_{RG}^{max} + 1) \times (N_{RG}^{max} + 1)$ diagonal matrix with $N_{ii} = i$, and $\mathbf{1}$ is a row vector of ones[52]. For the $\left(N_R^{(T)}, N_G^{(T)}\right)$ pairs with $N_{RG}^{max} = 1$ (i.e., two-state process), Eq. (32) reduces to a simple formula

$$C^{(2)}(\tau) = \frac{r_{on}r_{off}}{(r_{on} + r_{off})^2}e^{-(r_{on}+r_{off})\tau}$$

(33)

where r_{on} and r_{off} are the on- and off-rates of the reaction, respectively. Eqs. (24) and (25) gives

$$r_{on} = \frac{k_{on}N_R^{(T)}N_G^{(T)}}{N_A V_d} \text{ and } r_{off} = k_{off}.$$

(34)

The condition $N_{RG}^{max} = 1$ implies that at least one of $N_R^{(T)}$ or $N_G^{(T)}$ equals 1; however, one of these quantities can be greater than 1. The quantity $N_{RG}(t)$ was proportional to the acceptor fluorescence, so we

calculated the autocorrelation, $C_{AA}^{(2)}(\tau)$:

$$C_{AA}^{(2)}(\tau) = \langle \delta A(t+\tau)\delta A(t)\rangle \tag{35}$$

where δ represents the difference from the average. The autocorrelation was then fit to a model (Eq. (33)) to extract k_{on} and k_{off} (Figure 1.25). The fitting was performed in Matlab with error bars representing the 95% confidence interval determined by the Matlab measure of goodness of fit.

We calculated the autocorrelations for higher occupancies numerically by Eq. (31), keeping the k_{on} and k_{off} estimates from the two-state autocorrelations. The calculated curves agreed to the measurement for all high-occupancy correlations, confirming that the rate constants are not dependent on occupancy.

1.6.6   Perspectives: Nano-confinement effect

We have shown that confinement in nanoscale dimples rectifies statistical fluctuations in concentration that occur continuously in the bulk solution. Correlated colocalization of two species provides a quantitative measure of association in bulk. When the dimple volume is smaller than the mean volume per molecule in bulk, then single occupancy leads to an effectively higher concentration than in the bulk. Equilibria and reaction rates vary from dimple to dimple, purely due to stochastic fluctuations in occupancy.

An interesting subtlety of this experiment is that if one averages the quantity $\langle N_{RG}\rangle_t / N_R N_G$ over all dimples containing at least one red and one green molecule, the equilibrium is shifted in favor of dimers, compared to the equilibrium in bulk. This apparent bias occurred because we are calculating the equilibrium conditional on the dimples being occupied, and occupancy by even one molecule of R and one of G led to higher concentrations than in bulk. To reproduce the bulk ratios of [R], [G], and [RG], one would need to calculate the averages $\langle N_R\rangle$, $\langle N_G\rangle$, and $\langle N_{RG}\rangle$ over all occupancies *including* empty dimples prior to evaluating the equilibrium expression. Similarly, the apparent association rates in the dimples were higher than in the bulk, again because those dimples that had at least one of each reactant were at higher concentration than the bulk.

The confinement effects reported here are likely to be significant whenever molecules are confined to nanoscale volumes. Such scenarios commonly occur in vesicles and organelles in eukaryotic cells[47], in emulsions[48], and in micro-/nano-reactors[49]. While we focused on a bimolecular reaction, confinement effects will be more pronounced for higher-order reactions, and particularly for autocatalytic processes.

1.7 Future Direction

The Dimple Machine enables several new kinds of single-molecule experiments. Due to the deeply sub-wavelength confinement, single-molecule experiments can be performed with high signal-to-noise ratio at high concentrations of reactants. Only the Dimple Machine and small vesicles provide tight enough confinement to observe individual bimolecular association events at the single-molecule level. Zero-mode waveguides also allow single-molecule experiments at high concentrations[19], but free diffusion out of the waveguide limits observations of untethered molecules to microseconds.

A particularly intriguing application of the Dimple Machine is toward studying weakly interacting complexes. Weak interactions are difficult to quantify because complexes dissociate during most purification protocols. If the interacting species can be fluorescently labeled, then the Dimple Machine enables quantification of the interaction without purification.

Another possible application of the Dimple Machine is toward studying cooperative interactions. In a multimeric complex, there may be a distribution of association states. Description by a single Hill coefficient may miss important features of this distribution. Through fluorescence counting, the Dimple machine enables one to measure directly the underlying distribution of stoichiometries.

2 DNA Pulley: Manipulating DNA

2.1 Introduction

How flexible is a pencil? This sounds like a boring question, probably because you can pick it up, bend it, and see how stiff it is. When it comes to the stiffness of DNA, however, the question can attract thousands of smart people. The DNA Pulley is devised in an effort to answer this question, and to do so in the most direct way one can think of: bend it. The difficulty is in the length scale: the DNA behaves like a rod only under ~100 nm. How would you bend a 100 nm rod?

The DNA Pulley consists of a single DNA molecule hooked around a silicon nitride knife (Figure 2.1). One end of the DNA is attached to a glass surface, and the other to a magnetic bead. A magnet on the knife stretches the DNA taut. By moving the capillary with a nanopositioning stage, the blade can move along the tethered DNA, searching along the contour of the DNA for asperities (e.g., due to bound protein) or local deviations in bending modulus. We demonstrate that DNA Pulley system can probe local environment of a single DNA molecule by locating the proteins bound to the DNA. Next, we try measuring the local elasticity of the DNA, starting from a single-stranded nick as an extreme example.
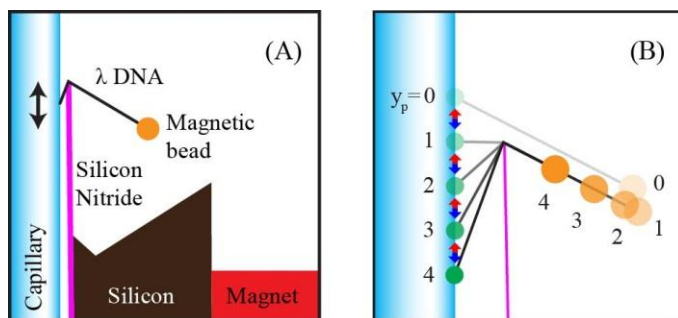
Figure 2.1   Scheme for the DNA Pulley

(A) A cartoon of the DNA Pulley showing a capillary holding the DNA, a surface-tethered λ DNA with a magnetic bead, and a silicon nitride knife with a magnet glued to it. (B) As the capillary is moved by a piezo, the DNA is pulled pivoting the knife-edge. The bead images are analyzed to extract information on the local environment of the DNA.

2.2 Background

2.2.1   Introduction

The structure of DNA has been the subject of study since its famous history of helix modeling[53,54]. Coupled with the emergence of its key role in genetics, scientists have characterized various structural parameters of the molecule. Here, we will review the history of the DNA elasticity, focusing on the experimental methods. Next, I will introduce existing single-molecule techniques for visualizing proteins bound to DNA.

2.2.2   Elasticity of DNA

Theoretical formulation for modeling the DNA with the language of polymer physics has gone hand in hand with the experimental findings. Two major theories considered were:

(1) Freely-jointed chain (FJC): a chain consisting of "random-walk" monomers, without any interactions between the monomers; and

(2) Worm-like chain (WLC): a chain consisting of elastic rods with a finite bending rigidity.

The history of the measurements on the flexibility of DNA[55] stepped forward together with testing these two theoretical models. One of the early experiments that provided noteworthy results is applying an electric pulse to align DNA and watching its rotational relaxation. The results from this experiment was in agreement with the WLC model[56]. In the WLC model, the elasticity of the DNA is effectively described by a single parameter, persistence length. This is the length scale over which the molecule "remembers" its orientation. Therefore, a polymer with its length comparable to its persistence length is at an intermediate regime where it is not very rigid, but not very flexible, either. For DNA, the persistence length in physiological condition is measured to be ~50 nm, with some ionic strength dependence.

After another decade, a single-molecule stretching with an optical tweezer has turned out as the most stringent test of the two models, confirming the WLC model[57,58]. This has sparked the single-molecule manipulation of DNA[59]: stretching and overstretching DNA[60], twisting and supercoiling DNA[61], and also

leading to the DNA Pulley. The ability to manipulate a single molecule of DNA has also enabled watching single protein molecules on the DNA (Section 2.2.4).

One of the classical methods of measuring the flexibility of DNA is cyclization assay (Figure 2.2). In this assay, a linear DNA construct whose two ends are complementary to each other is prepared. As the conformation of the molecule fluctuates, the open linear form is in equilibrium with its close circular form. When ligase is introduced, the fraction of circular form is covalently sealed and the amount of product is quantified. Because the efficiency of the circularization is related to its flexibility, this simple assay can reflect the underlying flexibility of the DNA. The results by this technique seemed to have approved the WLC model[62–64], in line with the consensus of the day, until a report[65] has started a long course of debate whether DNA is truly a worm or not.

2.2.3 More than WLC?

The report by Cloutier and Widom[65] claimed that the cyclization efficiency of a short DNA of length ~100 bp was 10^2–10^4 times greater than predicted by the WLC model. Because this was the first cyclization experiments done at this length scale, several other groups of scientists joined the debate to testify observations. Most notably, Vologodskii and coworkers reinvestigated the same experiments[66] to find out that the experiments in fact confirm the WLC model, rather than disproving it. They attributed the discrepancy in the interpretation to an improper ligase concentration. But this was not the end of the story: other results challenging the classical WLC view of the DNA has been reported since then[67,68].

Just like any scientific models and theories, polymer models microscopically distinct can still give rise to similar results on the longer length scale. Thus, the agreement of the past results cannot be concluded as proving the WLC model. The controversy in the field is mostly due to the absence of direct methods to
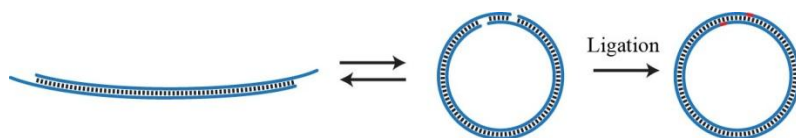
Figure 2.2   DNA cyclization assay
Linear DNA molecules with complementary sticky ends are in equilibrium with its circularized form, and the closed form is captured by incubation with ligase and quantified. The amount of closed form is related to the flexibility of the linear DNA.

probe the flexibility of DNA. In addition, because of the tight coupling between the two properties, (dynamic) *flexibility* and (static) *curvature*, the experimental approaches measuring the bending of DNA is usually confounded.

Another level of complexity comes from the sequence dependence. It is known that some sequences of DNA are particularly more bent or flexible than average. Because the properties of DNA being questioned are below the persistence length, say 100 bp, the randomness of the sequence becomes more difficult to guarantee. It would be more convincing to measure the flexibility and curvature as a sequence-dependent manner, and correlating the results with sequence characteristics, if any.

2.2.4   Visualizing single-proteins on the DNA

In the nucleus of a cell, a host of proteins directly interacts with DNA, by binding, diffusing, and zooming along the molecule. Some of them actively modify the DNA, breaking and re-joining it. Molecular biologists have gained incredible insights into most of these molecular systems in ensemble simply by mixing proteins with DNA and running a gel[69]. Single-molecule scientists during the past decades have horned fine tools for visualizing proteins on the DNA, and either affirmed or disproved these findings in the past, as well as gathering information on the newly discovered DNA-binding proteins. In this section, the major experimental methods for imaging proteins associated with DNA are overviewed[70,71]. We will categorize the methods by the way of manipulating DNA.

Molecular combing

This old technique is very simple: a drop of DNA solution is put on the substrate and dried[72,73]. The surface tension of the drying meniscus of water drags and stretches the DNA, leaving a DNA molecule tightly associated on the surface. The great advantage of this method is its simplicity, whereas the disadvantage is the nonspecific and heterogeneous interaction with the surface. The throughput of this method is relatively high compare to the other single-molecule techniques due to the ease of preparation. It can be used to map the protein binding sites in a long DNA molecule[74].

Stretching of surface-tethered DNA

In this approach, the target DNA is surface-tethered by one end, and the DNA is stretched by a variety of ways: a fluid flow[75–77], an electrokinetic flow[78], and optical or magnetic tweezers[61,79]. The fluid flow stretching can be accompanied by labeling the other end of the DNA with a micron-sized bead to increase and homogenize the stretching force along the DNA. The flow stretching of DNA can optical be parallelized with the help of microfabrication[80]. Alternatively, the DNA can be held with single-molecule tweezers. The DNA in this case must be labeled with a microparticle for steering. A method of flow-stretching a surface tethered DNA and fixing the second, sticky end of a DNA to the surface is also demonstrated[81]. Using multiple tweezers for steering one or two molecules of DNA simultaneously has been reported, too. These setups achieve a high degree of manipulation at the cost of complexity in the setup.

Scanning probe methods

The DNA Pulley system falls into this category. This method offers the most direct way of detecting proteins on the DNA. Broadly speaking, a sharp probe is scanned around the DNA in search of the proteins. The most well established device is AFM. Some successful cases were reported[82,83], but this method is still not very generalizable because of the diverse nature of proteins and limited resolution.

Other scanning probe techniques in combination with single-molecule tweezers have been developed. The first experiments was done using a micropipette as a probe[84]. However, this technique has not been reported to be able to detect proteins on the DNA. Shortly after, a scanning probe method utilizing a second DNA molecule as a probe is devised[85]. Here, four optical traps are used to control two DNA molecules independently. One molecule is wrapped around the other to tie a knot, and the knot is scanned along the DNA to detect bound proteins. This technique has been shown to detect several kinds of restriction enzymes bound to the DNA under non-cleaving condition. A variation of this technique replacing two optical tweezers with a magnetic tweezer is also developed and shown to perform similarly[86].

2.2.5   Motivations for the DNA Pulley

The DNA Pulley envisions perhaps the most direct way of measuring the local mechanics of single DNA molecules. A nano-knife made of silicon nitride can be used to either: (a) probe to measure the local curvature, (b) bend to measure flexibility, or (c) induce higher curvature to study nonlinear regime of bending. In particular, the DNA Pulley, in principle, can induce a high curvature that what is accessible by thermal fluctuation or other experimental techniques. This can be very informative as most of the experiments until now has been conducted only in the slightly bent regime.

Most recently, a way of introducing a high curvature in the DNA by a molecular force is devised in our group[87]. Here, a base-pairing zipping force is transferred onto the ends of a short segment of DNA, essentially tweezing the DNA. When the force becomes larger than a critical force, the DNA was shown to experience a mechanical failure known as Euler buckling. This mechanical transition, however, is not a sign of higher flexibility that what the WLC model predicts: in fact, this result is in agreement with the classical view of WLC model, without a need to invoke higher-order terms in the flexibility.

As all the information will be delivered in the coordinates of the magnetic bead, it is important to minimize the source of fluctuation: thermal noise from bead fluctuation, shot noise from the photon detection, thermal expansion from temperature drift, and any kinds of mechanical drift from the ground to the camera.

In addition to the investigation of local mechanical properties, the DNA Pulley system is expected to work as a 1-D AFM for the DNA. Because the thickness of the scanning blade is below 100 nm, it is able to detect the subtleties in the local environment, say proteins on the DNA, with a good precision. When combined with a fluorescence setup, the mechanical perturbation and scanning simultaneous with imaging can be valuable in understanding protein-DNA interactions sensitive to the force.

2.3 Construction of DNA Pulley

2.3.1 Introduction

DNA Pulley consists of three bodies: (a) A glass capillary that holds and moves the DNA, (b) a molecule of DNA, one end tethered to a capillary and the other to a magnetic bead, and (c) a silicon nitride knife that contacts the DNA and scans along the contour. This section describes the procedure for preparing the full system of the DNA Pulley. Next, I will provide methods for fabricating the silicon nitride knife. Silicon nitride knife is the key component of the DNA Pulley. It is the mechanical probe touching the DNA, and inducing perturbation when desired. Silicon nitride and silicon was chosen due to their high mechanical strength and ease of fabrication. Finally, an ultra-stable measurement setup for high sensitivity is discussed.

2.3.2 Synthesis of surface- and bead-tethered DNA

The body of DNA Pulley system is a single molecule of DNA. It is the molecule of interest, the local properties of which are to be measured. We employ a synthetic scheme employing λ DNA (Figure 2.3). For clear imaging, it is essential to use a construct longer that at least ~5 μm to ensure enough separation of the beads from capillary surface. This, however, does not limit the range of construct to be probed in DNA Pulley: any sequence of interest, either genomic or PCR-amplified, can be incorporated into the system by enzymatic reactions.
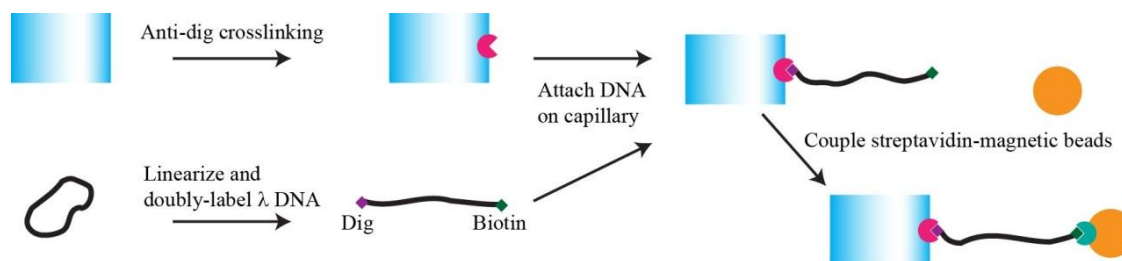
Figure 2.3   Synthetic scheme for the DNA in DNA Pulley
Anti-digoxigenin is cross-linked to the amino-silanized surface of a capillary. A λ DNA linearized and end-labeled with digoxigenin and biotin are then attached to the capillary via digoxigenin-anti-digoxigenin binding. Finally, a streptavidin-coated magnetic bead is reacted with the DNA-modified capillary to label the free biotinylated end of surface-tethered DNA.

The molecular construct is synthesized by attaching a λ DNA on glass capillary, and a streptavidin-coated magnetic bead on the DNA, in sequence. The overall procedure is summarized in Table 2.1.

Table 2.1   Synthesis of DNA Pulley

Step	Reagent	Duration	Rinse
Capillary cleaning	Acetone Alkonox solution (sonication) Air plasma after drying	1 min 10 min 5 min	N/A Water N/A
Amine modification[a]	(3-Aminopropyl)triethoxysilane (Sigma)	4 h	N/A
Aldehyde modification	0.5% Glutaraldehyde (Sigma) in PBS	30 min	PBS
Antibody crosslinking	20 μg/ml Anti-digoxigenin (Roche) in PBS	30 min	WB[b]
DNA tethering	200 pM Biotin- and dig-labeled λ DNA in PBS	1 h	WB
Surface passivation	WB	15 min	N/A
Bead coupling	4 pM Streptavidin-coated magnetic beads[c] in BB[d]	1 h	WB
Ligation	20 units/μL T4 DNA ligase (New England Biolabs) in T4 DNA ligase reaction buffer	1 h	WB
Bead passivation	50 pM biotinylated oligonucleotides in BB	30 min	PBS
Storage	WB		N/A

[a] Amine modification was carried out in a glass desiccator under vacuum with vapor-phase silane.

[b] WB (wash buffer): 1× TAE buffer with 130 mM KCl, 4 mM $MgCl_2$, 20 μg/ml acetylated bovine serum albumin, 80 μg/ml

[c] Streptavidin-coated beads (Dynabeads® MyOne™ Streptavidin C1, Life Technologies) were rinsed before use following manufacturer's protocol.

[d] BB (binding buffer): WB with 1 M NaCl

Linearization and labeling λ phage DNA

The λ phage genomic DNA (48.5 kb, 16 μm) is one of the most popular DNA structures. It was extensively studied as a model to understand mechanical properties of DNA. It was also widely employed as a linker in single-molecule constructs, due to its sticky ends permitting annealing or labeling by other molecules. Here in DNA Pulley, we use one of the sticky ends as a surface tether, and the other is labeled with a magnetic bead.

The λ DNA (New England Biolabs) was linearized and the two ends were each labeled with digoxigenin or biotin following adapting published protocols[88]. 0.5 mg/ml (15.6 nM) λ DNA in Tris-HCl

buffer was first linearized by heating up to 90 ℃ in the presence of 0.5 M NaCl, holding for 10 min, and

fast cooling in ice for 5 min. The linearized λ DNA was then mixed with a pair of oligonucleotides

(Integrated DNA Technologies): complimentary to the two 12-nt *cos* sites of λ DNA. The two oligos were

each 5'-labeled with digoxigenin or biotin, thereby introducing the labels to the construct.

Attachment of λ DNA on glass capillary

The flat outer surface of square glass capillaries (1 mm × 1 mm × 25 mm, Friedrich & Dimmock) were

used as a substrate for DNA Pulley. Using a flat surface has multiple advantages over a round surface

(Figure 2.4). The blade can access more molecules over a wider area. It also provides larger area optically

clear for imaging because less beads are shadowed by capillary. In addition, the analysis becomes easier

because the beads, when pulled with magnet, align in a straight line on the projected image, discriminating

unnatural pulley constructs.

The labeled λ DNA was conjugated to the surface of capillary by adapting published protocols[89].

Briefly, the glass surface was activated with glutaraldehyde, amino-modified with APTES, and coated with

anti-digoxigenin. The anti-digoxigenin-coated capillary was mixed with labeled λ DNA, The full sequence

of reactions is detailed in Table 2.1. All reactions from the aldehyde modification were carried out in PCR

tubes (1 capillary per tube) at room temperature. After bead conjugation, the construct was ligated to make

the bonds from annealing covalent.
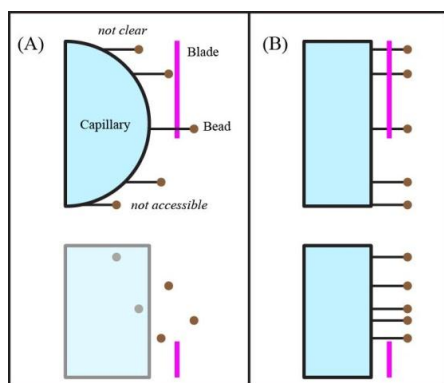
Figure 2.4   Comparison of flat and round surface for the DNA Pulley
A round (A) and a square capillary (B) showing the cross-section (*top*) and the projected image on a
camera (*bottom*). The beads (brown circles) are pictured in positions when pulled with magnets. A flat
capillary allows the blade to access larger area than a round capillary and locates the beads on a line when
they are extended.

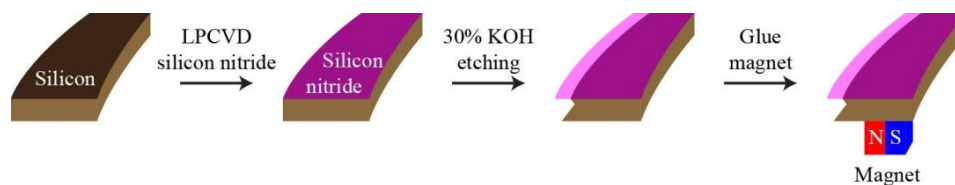### 2.3.3   Nanofabrication of the silicon nitride blade

50 nm of low-stress silicon nitride was deposited on a 400 μm-thick (100) silicon wafer using low-pressure chemical vapor deposition at Harvard CNS (Tystar). The nitride-coated wafer was then diced into 15 mm × 4 mm chips and etched in 30% KOH at 75 ℃ for 20–30 min. The etching created undercut sidewall on the curved edge, with typically 15–20 μm protrusion of the nitride blade-edge from the wafer (Figure 2.5).

Unfortunately, this scheme of nanofabrication is not very scalable because the nanofilm formed after wet etching is extremely fragile. The minimum thickness of the nitride blade, rigid enough for handling, turned out to be ~30 nm. Critical point drying that reduces the surface tension during the drying of blade is expected to help maintain intact thinner blades.

2.3.4   Attachment of magnet to the knife

Ideally, a magnet manipulating the beads should be controlled independent of both the capillary and the knife. However, in practice, spatial coordination of the three bodies (a capillary, a knife, and a magnet) in a small space is challenging. In particular, positioning the magnet as close to the pulley as possible is encouraged to exert a strong force (> 1 pN). With this regard, we decided to glue the magnet to the back of the silicon wafer, which achieves the minimum distance possible between the bead and the magnet. This configuration trades off a freedom of magnet for a significant ease of construction.

A 1/16" cubic neodymium magnet was glued on the back of the knife, away from the blade edge, with the north pole of the magnet facing toward the pulley in front (Figure 2.6A–B). The position of magnet


Figure 2.5   Fabrication scheme for the silicon nitride knife
Low-stress silicon nitride evaporated by LPCVD is used as a blade material. Silicon under the nitride film was etched back by 30% KOH, exposing the nitride blade. The distinct shape of the silicon wafer chip facilitated the etching from the side.

relative to the knife-edge determined the magnetic force vector acting on the pulley, typically exerting ~1 pN.

Figure 2.6 shows the stereomicroscope (A–B) and scanning electron microscope (C–E) images of final silicon nitride knife pictured at different angles and magnifications. Note that the edge of silicon nitride blade is nanoscopically smooth (Figure 2.6E), free from nanoscale grooves or cracks. This is critical to guarantee a reproducible contact, free from artifact, between the blade and DNA.

To minimize nonspecific adsorption of molecules on the silicon and silicon nitride, the knife was cleaned by air plasma for 10 min, immediately before the etching. This step is expected to increase the portion of silicon oxy-nitride on the surface, thereby increasing hydrophilicity. The blade is prepared fresh just before the experiments in all measurements presented.
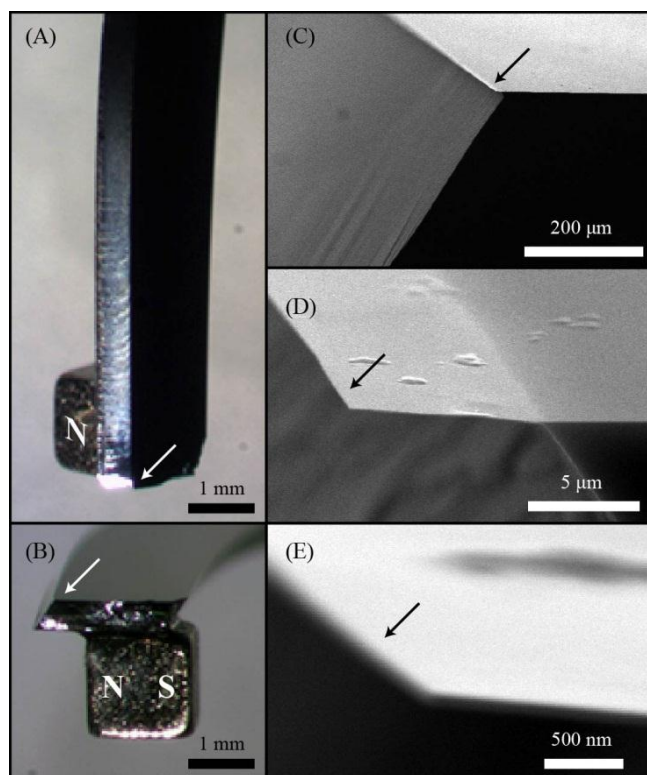
Figure 2.6　Images of silicon nitride knife

(A–B) Stereomicroscope images viewing (A) front and (B) bottom of the silicon nitride knife with a glued magnet. Silicon nitride blade is invisible at this scale. The location of nitride blade is marked with white arrows. Poles of the magnet are labeled as N or S. (C–E) SEM images of silicon nitride blade at different magnifications. The location of nitride blade is marked with black arrows. The edge is shown to be nanoscopically smooth over longer than 100 µm along the edge from the tip.

2.3.5   Measurement setup

Sample chamber and stages

A capillary with DNA Pulley was mounted in a custom Teflon/aluminum chamber with a glass bottom for imaging (Figure 2.7). After loading the sample (typically 500 μL), the chamber was fixed on a nanopositioning stage (Mad City Labs) and in turn on a micropositioning stage (Mad City Labs) for coarse positioning. Silicon nitride knife clamped on a separate *xyz*-micromanipulator (Newport) was aligned to the capillary ensuring high mechanical stability. The knife-edge was aligned orthogonal to the *xy*-plane so that the analysis was simplified.

The entire setup including the microscope was enclosed in a cardboard box and floated on an optical table with a vibration isolator. The experiments were conducted in an air-conditioned room to keep the room temperature constant. Mechanical drift in capillary and knife under this setting were checked to be minimal (~1 nm/min). In particular, enclosing the whole setup to block the air current reduced the drift by an order of magnitude.

Optical setup

All measurements were performed on an inverted white-light microscope (Olympus IX71). The sample was trans-illuminated with an LED and the resulting image of magnetic bead, Silicon nitride knife, and capillary was collected with a $40\times$ air objective (Olympus, N.A. 0.60) and recorded with a CCD (Andor, 16-μm pixels) at 2–20 Hz of frame rate depending on the types of measurements. To reduce camera pixelation artifacts, the image after tube lens was expanded with a $3\times$ beam expander before the CCD..
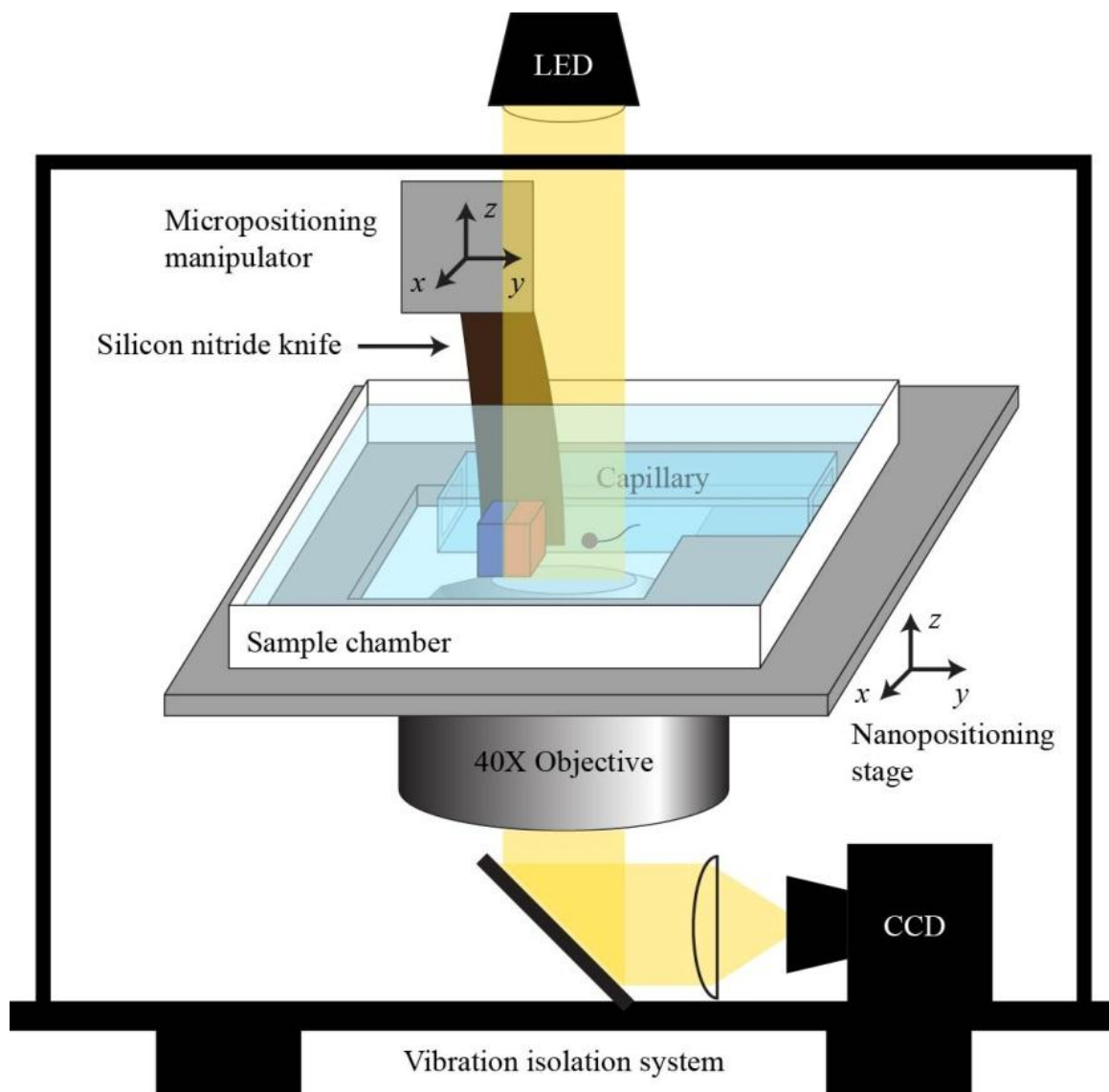
Figure 2.7   **Measurement setup for the DNA Pulley**

2.4 Verification of DNA Pulley

2.4.1 Introduction

In this section, the DNA Pulley system is validated through the localization of beads, either fixed on a coverslip or tethered by the pulley. Noises associated with bead localization, piezo stage precision, thermal fluctuation of beads in solution are discussed.

2.4.2 Localization of bead

Fixed bead localization accuracy

To estimate the localization accuracy, we looked at the fixed beads on a glass coverslip while the stage is at rest. The images acquired with CCD were analyzed by custom software written in Matlab. The bead positions were extracted by a radial symmetry-based localization method[90] from a $(29 \text{ pixel})^2$ or larger ROI (corresponding to $\sim(4 \text{ }\mu m)^2$ on the sample) (Figure 2.8A). When the images were recorded at 10 Hz, the localization accuracy was roughly 1 nm (Figure 2.8B–C). When the bead was observed for longer than 1 min, the mechanical drift ($\sim$1 nm/min) dominated the width of distribution.
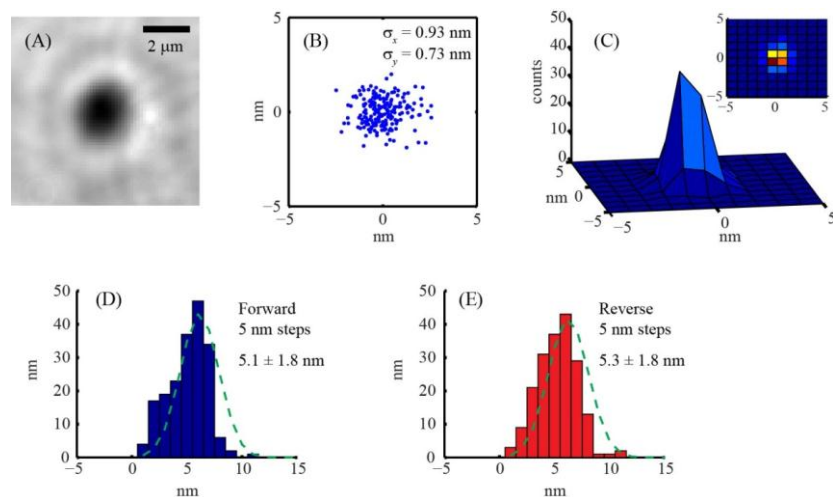
Figure 2.8   Precision of bead localization

Image of a fixed bead on a glass coverslip. The images are averaged over 20 s. (B) Localization of fixed bead at 10 Hz over 200 frames. (C) 2-D histogram of the data presented in (B). (*Inset*) the projection of the histogram. (D, E) Measurements of the step distances of the piezo stage. Bead images recorded during the 190 steps of forward and reverse 5-nm stepping were executed to calculate the step size.

Precision of the piezoelectric stage

Next, to estimate the precision of bead localization, we looked at the same bead while the piezo is stepping by 5 nm. The distribution of step sizes were centered at 5 nm as expected for both forward and reverse steps, and the width of distribution was roughly 2 nm. Assuming the same localization precision, we conclude that the accuracy of nanopositioning piezo stage is also around 1 nm.

2.4.3   Thermal fluctuation of the beads on the pulley

Fluctuation measurement

The magnetic force acting on the bead in the pulley was measured from thermal fluctuation of the bead, *in situ* before scanning experiments (Figure 2.9). The bead fluctuation with all stages at rest was recorded at 200 Hz and its fluctuation was fit to an exponential decay function with a time constant, τ.

Typical time scale of fluctuation was ~10 ms for the longitudinal axis, and ~100 ms for the lateral axis. The difference arises from the nature of pulley pivot, which constrains the stretching of the DNA more than
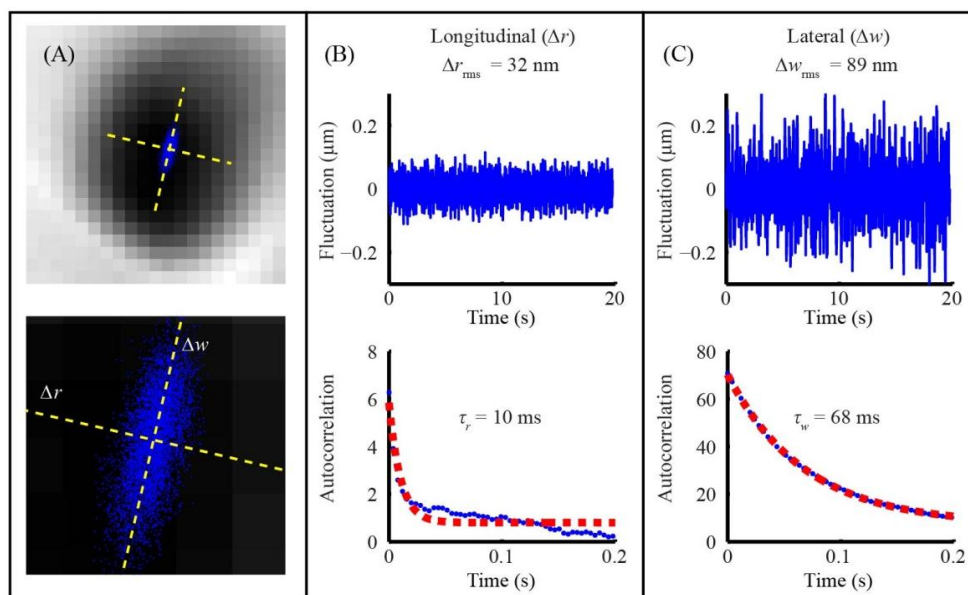
Figure 2.9   Fluctuation of beads on the pulley

(A) Image of fluctuating bead, recorded at 250 Hz and averaged for 1 min. Blue dots are the results of bead localization for each frame. Yellow dashed lines indicate the axes extracted from the principal components of the cloud of points. Bottom image is a close-up view of the cloud. (B, C) Fluctuation along the longitudinal axis (B) and along the lateral axis (C) with its respective autocorrelation (*bottom*). The autocorrelation decay is fit to a single-exponential curve to obtain the time constant, τ.

the rotation around the pivot. Because of this large difference in the thermal noise, the measurements of longitudinal coordinates are expected to be more sensitive to the DNA-dependent signals.

Fluctuation-Force-Extension curve

For a bead-on-a-spring system, the characteristic timescale of Brownian motion is given by

$$\tau = \frac{k_s}{\gamma} = \frac{k_s}{6\pi\eta a} \tag{36}$$

where k_s is the spring constant, γ is the drag constant, η is the dynamic viscosity of the medium, a is the radius of the bead. We obtained k_s from experimental τ values and calculated instantaneous spring constant of the DNA. This measurement lets you extract the total extension of the DNA and the applied magnetic force by comparing to the extensible worm-like chain model (a.k.a. modified Marko-Siggia equation[91]):

$$F = \left(\frac{k_{\mathrm{B}}T}{L_{\mathrm{p}}}\right)\left[\frac{1}{4(1 - x/L_0 + F/K_0)^2} - \frac{1}{4} + \frac{x}{L_0} - F/K_0\right] \tag{37}$$

where F is force; x, extension (end-to-end distance); L_{p}, persistence length; L_0, contour length, K_0, elastic modulus; $k_{\mathrm{B}}T$, Boltzmann constant times the absolute temperature. This relation combined with the fluctuation time scale measurement inferred a typical range of the force applied to the bead and the extension of λ DNA (Figure 2.10).

Note that our experiments do not rely on precise calibration of force, forgiving corrections for possible artifacts in this measurement such as camera time binning or drift. That is, the force measurements in this study served only as a qualitative check.
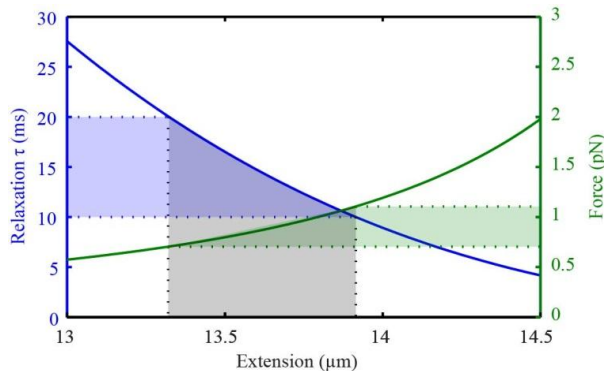
Figure 2.10 Calibration of force on the DNA Pulley
(*Left y-axis*) Measured relaxation time scale of the bead fluctuation. (*Right y-axis*) Stretching force on the DNA. The relaxation time scale typically ranged from 10 to 20 ms. These values correspond to, by Eqs. (36)and (37), 13–14 μm extension of λ DNA (85% extension) and ~1 pN of magnetic force.

2.5 Scanning along the Pulley

2.5.1 Introduction

This section describes a scanning experiment where the nitride blade is scanned along the contour of the DNA. The geometry of the bead trajectory was solved and the associated parameters for the pulley system were extracted.

2.5.2 Scanning a single DNA Pulley

A single DNA Pulley construct on the capillary was first located in the microscope with its bead pulled with a magnet. Only the constructs with longer than 10-μm separation from the surface was taken into scanning measurements to exclude spurious or unnatural molecules. The blade was first aligned in z to the molecule by moving the capillary up and down with the piezo, thereby aligning the DNA to the tip of the probe. To prevent unwrapping of the molecule from the blade during the scanning, the molecule was aligned typically $z = +5$ μm above the tip. The precision of this alignment procedure was higher than 1 μm.

After z-alignment, the blade was placed as close as possible to the capillary, ensuring no contact at the same time. Note, however, that a dead space in the probe scanning from a big spacing between the capillary and the blade is not a limitation, since the DNA molecules can be modified to hold the sequence of interest sufficiently away from the end.

Lastly, the piezo was ramped in y to locate the first touch of the blade to the DNA. When the first contact point was established, the piezo was retracted 2–3 μm back form the contact to make the engagement process clear. Although this engaging period does not convey any information on the DNA itself, the resulting trajectory becomes more sensitive to the fitting to a model, improving the precision of molecular mapping. A typical scanning experiment consisted of a triangular ramp of 1.2–1.6 V, corresponding to a travel of 12–16 μm, a pair of forward and reverse scans. The scan speed was 1 μm/s for the trajectory mapping.

2.5.3 Bead trajectory analysis

Conversion of coordinates

All analysis of scanning was started by localizing the bead in the acquired images, and then converting the coordinates in pixels into the molecular coordinates (Figure 2.11). The long-axis of molecular coordinate system is readily revealed by minimum-filtering of the scanning trajectory.
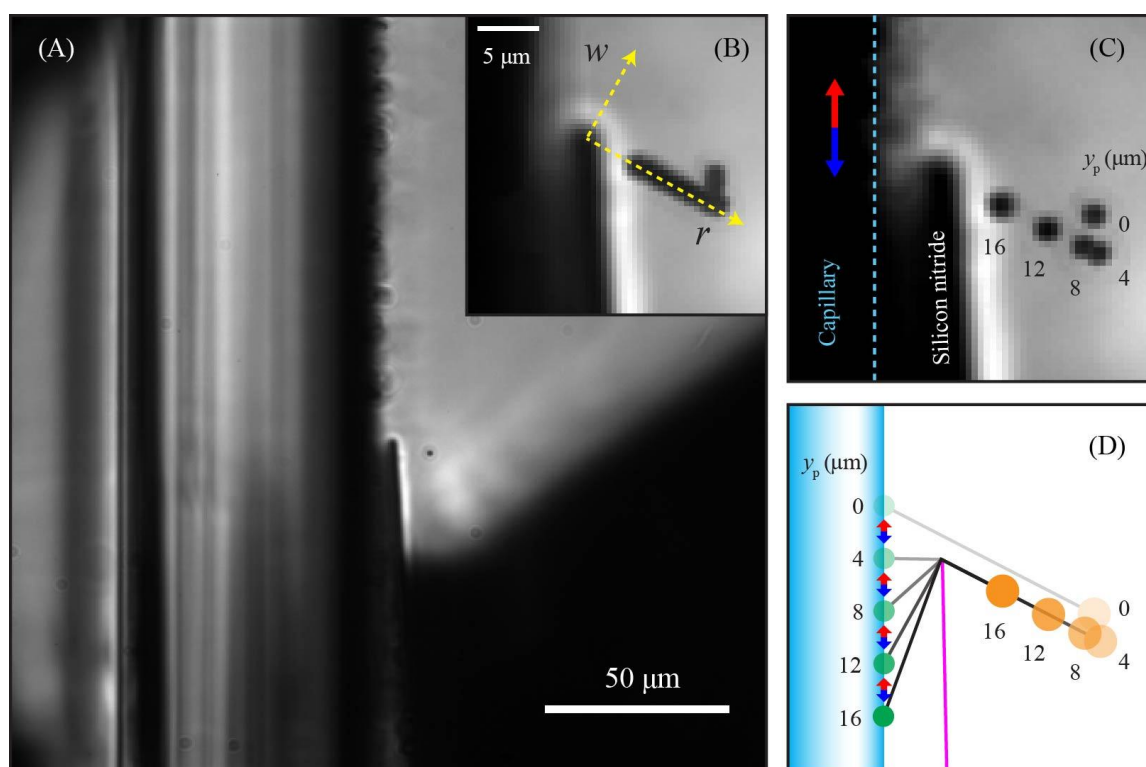
Figure 2.11 Analysis of the DNA Pulley scanning trajectory
(A) A wide-field view of the DNA Pulley on the capillary (*left*) with a silicon nitride knife (*bottom right*). (B) Bead images over a full scan are minimum-filtered to highlight the passage of bead. The molecular axes *r* and *w* can be extracted after localizing the beads. (C) Time-lapse images of bead at selected points. Numbers next to the beads indicate the coordinates of piezo movement, y_p. Capillary is marked with a cyan dashed line. (D) Cartoon of the pulley corresponding to the time points in (C).

The raw coordinates in pixels were converted to two-axis molecular coordinates:

(a) **A radial coordinate, *r*.** This is the distance of the bead from the blade edge-DNA contact point, or the pivot point of pulley. The *r* must be shorter than the actual contour length of the DNA segment between the bead and the blade for two reasons: (a) the force may not be strong enough to stretch the molecule up to its full extent, and (b) the direction of magnetic force may not be in the *xy*-plane, in which case the projection on 2-D is shorter than the length in 3-D.

(b) **A lateral coordinate, *w*.** The lateral deviation of bead from the linear scanning trajectory. Due to the high noise from thermal fluctuation, this measurement is not informative.

Geometry of the DNA Pulley

By solving the geometry of the pulley system, the bead motion can be fully characterized with a small set of parameters. The measurements of *r* can then be fit to a model and plotted as a function of the blade location along the DNA. This way, the information on the local environment of DNA contained in *r* is expressed as a function of the sequence of the DNA.

The analysis of scanning trajectory is greatly simplified if the blade edge is aligned parallel to the *z*-axis, eliminating both the nonlinear sliding of pivot along the edge and the out-of-plane motion of the bead. Before experiments, the blade edge was viewed through the *z*-axis and aligned/checked to be vertical. In contrast, the angle of force vector in the setup is not precisely controlled. Because the distance of the magnet from the bead is comparable to the size of the magnet, the magnetic field around the bead cannot be simply predicted. Thus, the azimuthal angle of the force vector must be included as a fitting parameter.

When the *z*-component of the magnetic force vector is not zero, the bead is pulled upward, and therefore the *z*-coordinates of the three points B (bead), P (pivot), and S (surface attachment) are generally different (Figure 2.12). More precisely, only B is located in the image plane because the microscope is focused onto the bead, irrespective of P or S. Even if $\phi_f \neq \pi/2$, however, the bead does not move out of the initial image plane if the knife is vertical.
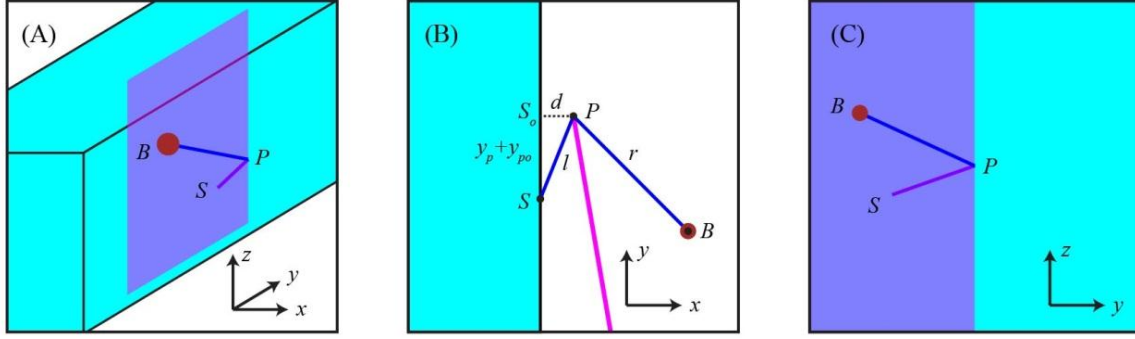
Figure 2.12 Geometry of the DNA Pulley

(A) 3-D view of the pulley system. The points B, P, and S are the coordinates for the bead, pivot, and surface attachment point, respectively. (B) The pulley viewed on the xy-plane, or the image plane. (C) The pulley viewed on the yz-plane. Note that the three points B, P, and S do not lie on the same xy-plane when $\phi_f \neq \pi/2$. Because the length $\overline{SP} = l$ in (B) is the projection onto xy-plane, it is shorter than the actual length of $\overline{SP} = l$ by a factor of $\sin(\phi_f)$, where ϕ_f is the azimuthal angle of the force vector.

From Figure 2.12B, we can relate the observable r to the independent variable, piezo coordinate (y_p). S_0 is the point on the surface closest to the pivot. We will call this distance d, which is the spacing between the capillary and the knife. Although the exact location of S_0 is unknown, the distance $\overline{SS_0}$ is simply the piezo coordinate y_p offset by a constant (y_{po}), because the point S moves linearly and 1:1 with y_p. In addition, from the right triangle $\triangle SS_0P$, we get

$$l^2 = \left(y_p + y_{po}\right)^2 + d^2. \tag{38}$$

Therefore, the rest of the DNA, r, is given by

$$r = l_0 - l = l_0 - \sqrt{\left(y_p + y_{po}\right)^2 + d^2} \tag{39}$$

where l_0 is the total extension of DNA projected onto the xy-plane.

Ratiometric measurements of length and molecular coordinate

The length l and l_0 described so far is the projection of molecules onto the xy-plane. As mentioned above, the DNA is in general not lined in a horizontal plane because of the z-component of the force vector. Therefore, l_0 can in turn be expressed as

$$l_0 = L_0 \sin \phi_f \tag{40}$$

where L_0 is the total extension in 3-D and ϕ_f is the azimuth of magnetic force vector. In our measurements, the two variables, L_0 and $\sin \phi_f$ does not have to be separated. Hence, we will regard l_0 as a single fitting parameter, acknowledging that we do not know L_0 and $\sin \phi_f$, independently. Thanks to the geometric similarity between the projected lines and the shapes in 3-D, however, the ratio l/l_0 in the projected image is the same as the ration in 3-D space, L/L_0, and therefore this ratio is enough to infer the absolute position of the blade on the DNA, i.e., the sequence.

Eq. (39) serves as a model for fitting the bead motion as a function of piezo coordinates. (Figure 2.13) The model fit the measured radial coordinates $r(y_p)$ very well in all cases examined. Occasionally (under 10%), there were a fraction of pulley construct displaying a curve with l_0 longer than 16 μm. We think these constructs are either spurious, dimers, damaged (nicked or unzipped), or overstretched DNA.
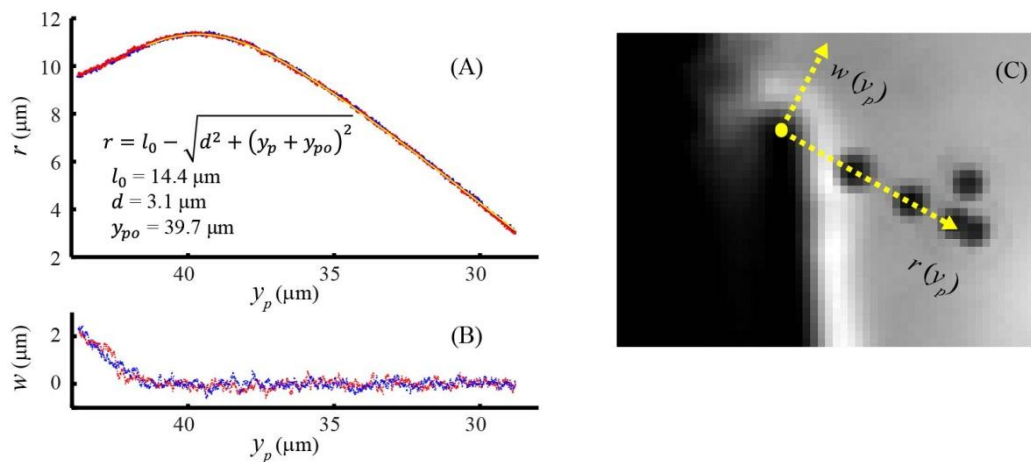
Figure 2.13 Molecular coordinates measured in simple scanning

Forward (*blue*) and reverse (*red*) trace of scanning is overlaid with a yellow fit. The fitting parameters obtained by this model are reasonable. (A) Radial coordinates with the fit. (B) Lateral coordinates. Note that the initial decrease in w is not a pulling, but the approach before the blade touches the DNA. (C) Microscope images of bead with molecular axis.

2.6   Detection of EcoRI on DNA

2.6.1   Introduction

When probing site-specific local features of DNA with the DNA Pulley, one will have to know where the blade is located, as precisely as possible. Potential candidates for the fiducial markers include polystyrene nanospheres, quantum dots, fluorescent beads, etc. While these methods will introduce structures that might be big enough to be detectable, site-specific labeling of a long DNA such as λ DNA is still a challenging task. To achieve simple site-specific labeling, we introduced EcoRI restriction enzymes under non-cleaving conditions that form stable complexes with the DNA at the cognate sites.

2.6.2   Measurement condition

EcoRI proteins recognize 6-mer palindromic sequence GAATTC in the DNA, and its specificity is among the highest of the restriction enzymes. While the enzyme requires Mg^{2+} for catalytic activity, Ca^{2+} in place of Mg^{2+} is known to inhibit enzymatic activity completely[92]. The specificity and affinity for the cognate sites are still preserved, however, making it a useful tool for designing a site-specific protein-DNA complex. The λ DNA on the pulley contains 5 EcoRI recognition sites, located at 21,226, 26,104, 31,747, 39,168, and 44,972 bp away from the surface tethered end.

The DNA Pulley was first incubated with 10–50 nM EcoRI-HF in the presence of 1 mM $CaCl_2$, typically for 1 h. The effect of incubation time on the protein-DNA complex formation was not thoroughly investigated. After the EcoRI incubation under non-cleaving condition, we did not notice a substantial reduction in the number of pulleys on the capillary surface. This confirms that the EcoRI with calcium ions were not effective in digestion.

The EcoRI-incubated DNA Pulley constructs were studied by applying the same scanning condition as in the simple trajectory mapping. The scanning speed was 1 μm/s with a 100 Hz sampling and camera frame rate.

2.6.3   Friction between EcoRI and the blade

When we scanned the pulley after incubation in EcoRI, a dramatic new behavior was detected: the movements of the bead were mostly the same, but many intermittent pauses of the movement were observed (Figure 2.14). We found that this signal was indeed EcoRI-dependent and reproducible in other pulley constructs, in other sample preparations, and in other batches of EcoRI stocks. In addition, there were localized regions exhibiting this behavior repetitively.
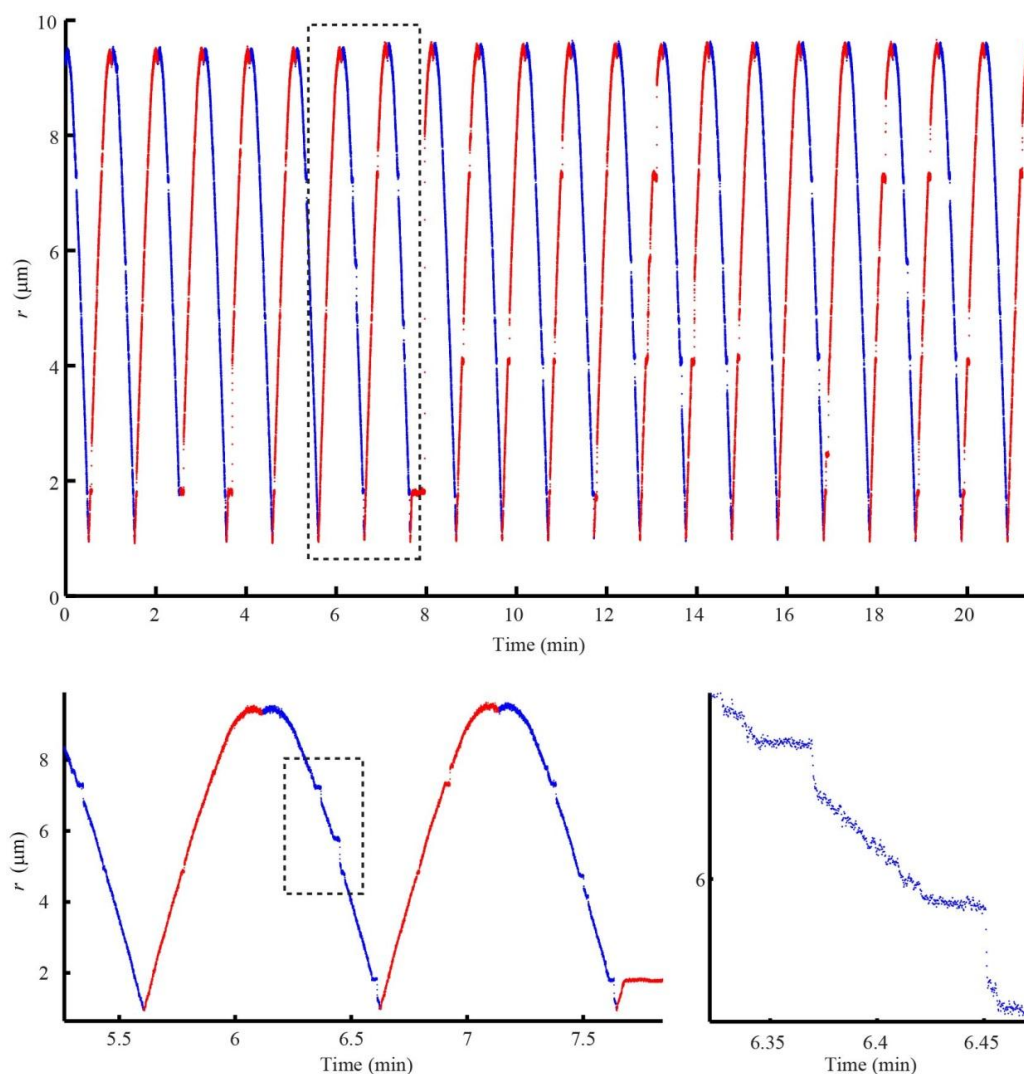
**Figure 2.14 Friction between EcoRI and the blade**

Consecutive 21 scans of forward (*blue*) and reverse (*red*) direction. There are occasional pauses during the scan, both in the forward and reverse scan. In particular, the lifetime of such pauses was longer in reverse direction. Black dashed rectangle marks the area zoomed in for the next graph.

Asymmetry between the forward and reverse direction

The pauses induced by EcoRI were pronounced in the reverse scans (red curves in Figure 2.14). Why are the EcoRI signals more pronounced in the reverse scan than in the forward direction? The interpretation of the asymmetry is given in Figure 2.15. When the blade is stuck by a protein during the forward scan, the force by piezo on the blade, on the protein, on the DNA is in sequence stretching the DNA. Therefore, latching on the EcoRI and moving forward will introduce high strain in the construct. One of the bonding must break before it moves further. On the other hand, the reverse scan does not induce strain into the molecules because the piezo moves in the direction of loosening the DNA. Hence, the protein-blade interaction was long-lived during the reverse scan.

Nature of protein-blade friction

What causes the blade to stall near the protein? There are two major possibilities: (a) the proteins might stick to the silicon nitride at the molecular level, or (b) the protein might act simply as a mechanical roadblock to the running blade. Studying the friction as a function of force is likely to distinguish the two possibilities. If (a) is true, a high force on the DNA will help detach the protein from the DNA. If (b) is true, a high force on the DNA will tighten the rope around the pivot (blade), making the proteins to get around harder.
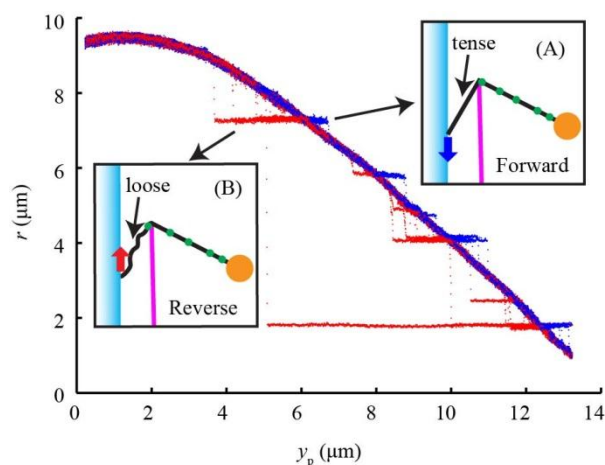
Figure 2.15 Asymmetic interaction of EcoRI with the pulley

In the forward scan, the movement of piezo increases the strain in the construct, until one of the bonds break. (B) In the reverse direction, the movement of piezo does not increase tension in the molecule, loosening the pulley. As a result, the lifetime of such interaction is longer for the revere scan.

2.6.4 Mapping EcoRI recognition sites

Can we reliably map the detected sites to the know sequences of DNA? If so, would it serve as a fiducial marker for further studies? We already developed a well-behaving model for the pulley system in Section 2.5.3. Here, we will further manipulate this model to interpret EcoRI data.

The piezo stage essentially positions the blade to a predefined location along the DNA, at every point. From the Figure 2.12, this function will be $l(y_p)$ and given by

$$l_{in}(y_p) = \sqrt{(y_p + y_{po})^2 + d^2}. \tag{41}$$

To make it explicit that this function is an input to the system, not a measurement, we will call it $l_{in}(y_p)$. When the pulley runs ideally, the actual position of the blade $l_{out}(y_p)$ will be the same as the input, $l_{in}(y_p)$. This output is measured in the pulley system by the bead coordinates:

$$l_{out}(y_p) = l_0 - r. \tag{42}$$
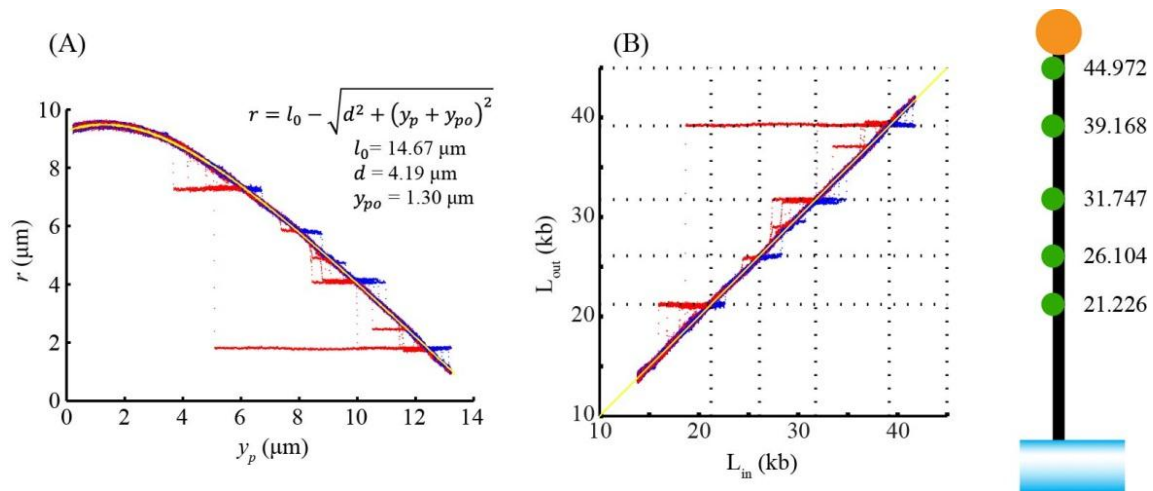
Figure 2.16　Mapping of EcoRI sites to sequences

(A) First, the fitting parameters for the regular scanning were extracted. A plot of r vs. y_p was used as described above. (B) A plot of the measured output location versus the input location. EcoRI proteins were detected at 4 out of 5 recognition sites, with two nonspecific sites. The black dotted lines mark the recognition sites for EcoRI. The cartoon on the right depicts the DNA Pulley with the exact EcoRI recognition sites on a λ DNA molecule.

However, when the pulley does not run smooth (e.g., EcoRI bound to DNA), the output will deviate from prediction. Therefore, by plotting $l_{out}(y_p)$ versus $l_{in}(y_p)$, we can learn the deviation of the system from regularity. Lastly, to recover the molecular dimension, we can take the ratio of l and l_0, and multiply by the full length of λ DNA (48.5 kb). This step converts l_{in} and l_{out} to L_{in} and L_{out}, respectively.

The measured binding sites of EcoRI are clearly registered to its known binding sequences in the λ DNA in all molecules probed. In Figure 2.16, for example, the 4 binding sites in the range probed by the blade were mapped to its recognition sites. Interestingly, there were two additional sites detected during the scanning, where the bound proteins are displaced by the blade relatively easily. We attribute these weaker binding events to nonspecific binding of EcoRI.

2.6.5   Detection of EcoRV on λ DNA

EcoRV is another Type II restriction enzyme similar in mode to EcoRI. We tested if EcoRV will behave the same way as EcoRI, except for the different density of the recognition sites (21 sites for EcoRV compared to 5 for EcoRI). Figure 2.17 presents such a result, displaying the same pauses of the blade during the scanning.
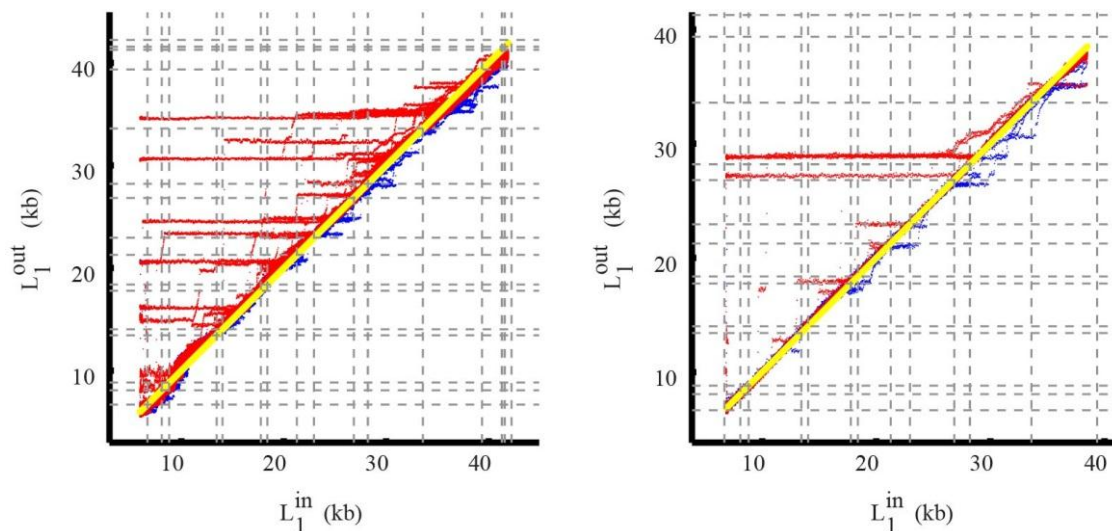
Figure 2.17   EcoRV dragging the blade similarly to the EcoRI

Measurements of the two pulleys in the same sample buffer are presented (63 scans for the left plot, 20 scans for the right plot). Similar to the EcoRI-induces pauses, the EcoRV-induced pausing is more prominent in the reverse direction. The black dashed lines mark the recognition sites for EcoRV.

2.7 Local Elasticity of DNA

2.7.1 Introduction

The ultimate goal of this project is to extract local elasticity of the DNA, as a function of sequence. In this section, theoretical calculations of the expected signal as well as the initial investigations with single-stranded nicks are presented. Challenges in this sensitive measurement are discussed at the end.

2.7.2 Elastica theory and simulations

To estimate the level of signal we are expecting, the DNA-bending model was simulated. The problem of elastic bending of a rod is first posed by James Bernoulli in 1961. The solution to the problem, known as elastica curves, is fully solved by the work of Bernoulli himself[93] and Euler[94*]. We modeled the DNA as a simple cylindrical rod experiencing an external force on the ends. Due to the two-fold mirror symmetry of the force in the DNA Pulley, we only consider the half with the half with a magnetic bead.

The bending of DNA pivoted on the nitride blade can be thought of as a rod with one end clamped (Figure 2.18). Consider a segment of the tethered DNA with a length *L*, comparable to the persistence length (50 nm). Microscopically, the end of this DNA segment will experience a vertical force downward transmitted as a tension. In this configuration, the angle between the tangent to the rod and the *y*-axis (θ_0) is determined by the segment length[95]:
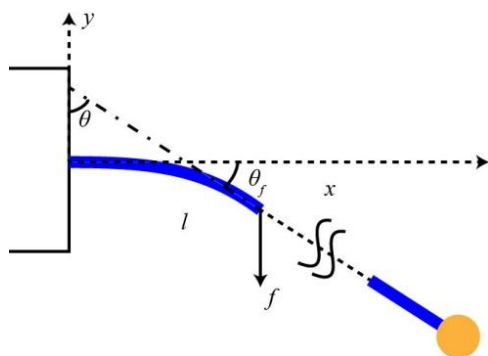
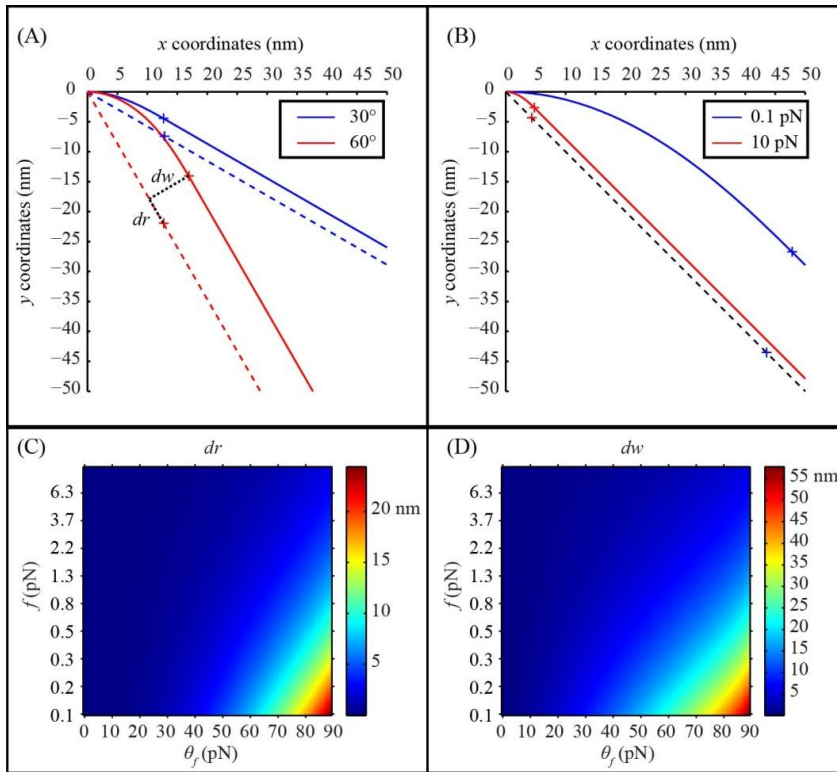**Figure 2.18 Elastica model for the bending of DNA clamped on one end**

---

* According to a reference[98], "The complete solution is most commonly attributed to Euler in 1744 because of his compelling mathematical treatment and illustrations, but in fact James Bernoulli had arrived at the correct equation a half-century earlier."

$$L = \sqrt{\kappa/2f} \int_{\theta_0}^{\frac{\pi}{2}} \frac{\cos\theta \, d\theta}{\sqrt{\cos\theta_0 - \cos\theta}} \tag{43}$$

where κ is the bending modulus and f is the applied force. In the DNA Pulley, θ_0 is bound by the polar angle of magnetic force vector, θ_f, as $\theta_0 = \pi/2 - \theta_f$. Therefore, plugging in θ_f into the Eq. (43) will give a length, L^* at which point the shape of DNA transitions from an elastica to a straight line. The complete shape of the elastica regime (Figure 2.19, solid curves) is parametrically given by θ_f:

$$x = \sqrt{2\kappa/f}\left[\sqrt{\cos\theta_f} - \sqrt{\cos\theta_f - \cos\theta}\right],$$

$$y = \sqrt{\kappa/2f} \int_{\theta}^{\frac{\pi}{2}} \frac{\cos\theta \, d\theta}{\sqrt{\cos\theta_f - \cos\theta}}. \tag{44}$$

Figure 2.19 Calculation of DNA bending comparing elastica and kinked DNA

The DNA is modeled as a rod with the persistence length of 46.5 nm (solid curves) and compared to the free joint or kinked model (dashed lines). Crosses on the curves for the two models are marked at the same contour length from the origin. (A) Varying the force angle, θ_f, at a constant force magnitude $f = 1$ pN. The difference between the elastic and kinked model is greater at a larger angle. The longitudinal and lateral difference is designated as dr and dw, respectively. (B) Varying the force magnitude, f, at a constant force angle $\theta_f = 45°$. The difference between the elastic and kinked model is greater at a smaller force. (C–D) Extended simulations of the plot in A and B.

As depicted in Figure 2.19A and B, the signal we are looking for is the difference in the bead position, resulting from a change in the local structure. If the DNA behaves as a perfect WLC, it will follow the solid curves. If the curvature introduced in the DNA is relieved by a localized kink, it will follow a free-joint curve shown in dashed lines. To estimate the signal, the coordinates of the end of the DNA segment for the two models, keeping the same contour length, is compared with the cross marks on the curves.

A large bending angle or a weak force is expected to give a large difference in the naturally curved and the kinked state. In addition, the amplitude of *dw* is generally larger than *dr* (Figure 2.19C and D). However, a weak force condition or measuring *dw* instead of *dr* suffers from higher thermal noise than measuring *dr* at a strong force condition.

2.7.3　Single-stranded nicks

An extreme instance of flexibility in a DNA molecule will be a single-stranded nick. We introduced single-stranded nicks at defined positions with a nicking enzyme, Nb.BbvCI. This enzyme has 7 recognition sites in the DNA (Figure 2.20). Because we demonstrated reliable mapping of the blade location onto the molecular coordinates, we attempted to localize a nicked site and probe the details with a slow scanning, averaging over many frames to maximize the measurement precision.

Measuσrement condition.　　The DNA Pulley capillary was first incubated with a working concentration of Nb.BbvCI at 37 ℃ for 1 h for nicking. The capillary was washed with WB (Table 2.1) to dilute and remove nicking enzymes. The nicked DNA Pulley was then incubated with EcoRI, same as in Section 2.6.

Results.　　The nicked DNA capillary contained significantly less amount of pulley constructs compared to the capillaries before the nicking. We think this is because either nicks make the DNA fragile, or the nicking enzymes occasionally cleave both strands due to nonspecific activity.
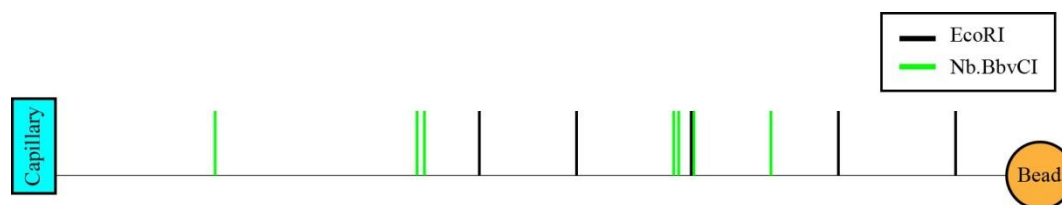
Figure 2.20　Reconition sites for EcoRI and Nb.BbvCI nicking enzymes in λ DNA

There are 5 and 7 recognition sites in λ DNA for EcoRI and Nb.BbvCI, respectively.

The nicked DNA Pulley showed the same scanning trajectory as in the intact DNA (Figure 2.21A, B), and therefore permitted the application of the same fitting model (Eq. (39)). This allowed us to pinpoint the location of nicks, zoom in on the section, and conduct slow and precise measurement over a long time.
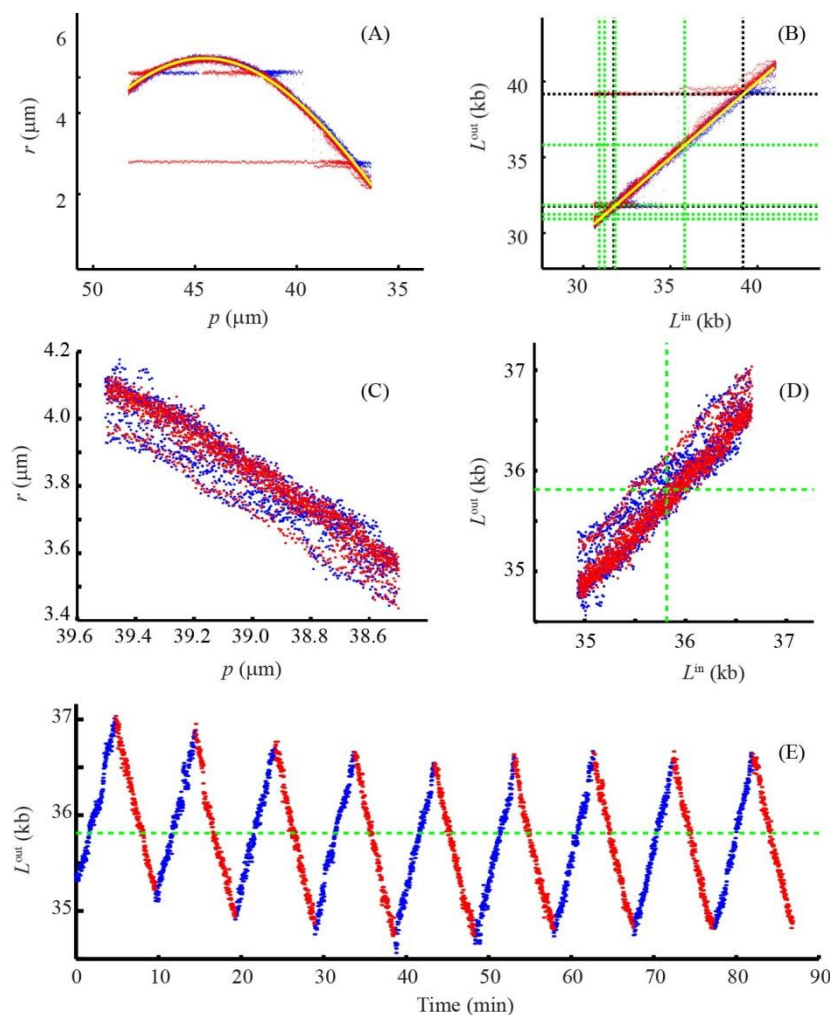
Figure 2.21 Measurement of the local flexibility near single-stranded nicks

(A) The scanning trajectory of the nicked DNA. The yellow curve is the fit to the model Eq. (39). The EcoRI signals allow us to map the blade location on the molecular coordinates. (B) The scanning trajectory plotted as a function of molecular coordinate. Black and green dotted lines mark the recognition sites for EcoRI and EcoRV, respectively. (C) Slow scanning experiments (9 scans) over a 2-μm section of the region scanned in (B). (D) A mapping of the curves in (C) onto the molecular coordinates. The green dotted line marks a recognition site for the nicking enzyme, located at 35,813 bp away from the surface end. (E) A plot of 9 consecutive scans plotted as a function of time. Due to the drift on the hour time-scale, the registration of consecutive scans is gradually lost, leading the blurring of the collection of scans.

Challenges

Scanning a short segment over a long period has been unsuccessful for the reasons discussed below, mostly related to the measurement precision and noise.

(a) **Mechanical drift of the sample.**   As shown in Figure 2.21C–E, the registration of scans taken over a long period (1.5 h) is gradually lost. The drift in this graph, ~100 nm in 90 min, is expected to arise from the mechanical drift in the system (~1 nm/min). Despite a considerable effort to improve the stability, the hour-scale random drift persisted.

(b) **Thermal fluctuation of the bead.**   When we looked at individual scans in Figure 2.21C–E, we found that the fluctuation within each scan is ~10 nm, which is still high compared to the expected signal (Figure 2.19). Increasing the force will reduce the thermal noise at the risk of breaking and losing the pulley. Unfortunately, the lifetime of nicked constructs was significantly shorter than intact pulleys, prohibiting prolonged observation.

(c) **Pixelation.**   The localization of beads is inherently limited by camera pixelation. A 16-μm pixel in our CCD, when equipped with a $40\times$ objective, images an area of $(400\,\text{nm})^2$. Pixelation artifacts manifest as a sudden jump in the bead localization, very much like a signal expected from a local fluctuation in the elasticity of DNA. Using a high magnification objective will reduce the artifact, but the constraint in working distance makes the pulley operation challenging. In order to minimize pixelation artifacts, we inserted a $3\times$ beam expander between the microscope tube lens and the camera.

(d) **Detection shot noise.**   Every signal of N in nature comes with a shot noise, $\sim\sqrt{N}$. The only way of minimizing shot noise is averaging as many frames as possible, requiring a long measurement time. This conflicts with the drift issue that is dominating when taking long movies.

(e) **Thermal drift.**   Because all the objects in the microscope images are magnified by two orders of magnitude, a small temperature drift leading to thermal expansion of the metals in the optical table, microscope body, the mechanical stages and holders can manifest as an extremely slow drift. We performed the measurement in an air-conditioned room for temperature stability.

(f) **Loss of pulley.**   A particular concern in the nicking experiments was the high loss of samples, during both the preparation and the scanning. It is supposed that the nicks would make the molecule more fragile, so that many of the constructs are lost by shearing. In addition, the nicking enzyme Nb.BbvCI, an altered form of restriction enzyme BbvCI, may retain some level of double-strand-cutting activity, which will sever the construct by acting on a single location.

2.8 Future Direction

Using the DNA Pulley, we demonstrated the capability of detecting proteins bound to the DNA, and localizing its position that agreed with the prediction. In this light, the techniques proved its potential as a 1-D scanning probe technique. Unlike the other techniques using DNA as a scanning probe, the silicon nitride probe is hard, suited for mechanical measurements.

Proteins that introduce a structural change to the DNA will be particularly interesting to study. In fact, the restriction enzymes studied here (EcoRI and EcoRV) are known to induce a bend in to the DNA. A careful measurement near the protein sites might reveal a local variation in the structure. In this light, proteins that are designed to induce high curvature will be of interest.

The nano-mechanical measurements single-stranded nicks until now has not detected a local increase in the flexibility/curvature. To enhance the signal, one can create a single-stranded gap, possibly expanding the flexible region. This might be challenging, however, because the molecules with a long single-stranded region are assumed delicate.

The opposite direction of nano-mechanical measurement of single-stranded nicks is to measure stiffening of DNA. RecA filament is an example that stiffens DNA. It first forms a protein-DNA filament with a ssDNA, and searches for a homology in sequence sliding along the dsDNA. When it finds a match, the RecA-ssDNA-dsDNA complex forms a stiff filament. This experiment might be practically easier than working with fragile nicked samples.

Bibliography

1. Brown, R. A brief account of microscopical observations made in the months of june, july and august 1827 on the particles contained in the pollen of plants. *Philos. Mag.* **4,** 161–173 (1828).

2. Shon, M. J. & Cohen, A. E. Mass action at the single-molecule level. *J. Am. Chem. Soc.* **134,** 14618–23 (2012).

3. Dickson, R. M., Cubitt, A. B., Tsien, R. Y. & Moerner, W. E. On/off blinking and switching behaviour of single molecules of green fluorescent protein. *Nature* **388,** 355–8 (1997).

4. H. Peter Lu, Luying Xun, X. S. X. Single-molecule enzymatic dynamics. *Science (80-.).* **282,** 1877–1882 (1998).

5. Ha, T. *et al.* Initiation and re-initiation of DNA unwinding by the Escherichia coli Rep helicase. *Nature* **419,** 638–41 (2002).

6. Rhoades, E., Gussakovsky, E. & Haran, G. Watching proteins fold one molecule at a time. *Proc. Natl. Acad. Sci. U. S. A.* **100,** 3197–202 (2003).

7. Okumus, B., Wilson, T. J., Lilley, D. M. J. & Ha, T. Vesicle encapsulation studies reveal that single molecule ribozyme heterogeneities are intrinsic. *Biophys. J.* **87,** 2798–2806 (2004).

8. Cisse, I. I., Kim, H. & Ha, T. A rule of seven in Watson-Crick base-pairing of mismatched sequences. *Nat. Struct. Mol. Biol.* **19,** 623–7 (2012).

9. Reiner, J. E. *et al.* Optically trapped aqueous droplets for single molecule studies. *Appl. Phys. Lett.* **89,** 013904 (2006).

10. Cohen, A. E. & Moerner, W. E. Method for trapping and manipulating nanoscale objects in solution. *Appl. Phys. Lett.* **86,** 93103–93109 (2005).

11. Cohen, A. E. & Moerner, W. E. Suppressing Brownian motion of individual biomolecules in solution. *Proc. Natl. Acad. Sci. U. S. A.* **103,** 4362–5 (2006).

12. Goldsmith, R. H. & Moerner, W. E. Watching conformational- and photo-dynamics of single fluorescent proteins in solution. *Nat. Chem.* **2,** 179–86 (2010).

13. Cohen, A. E. & Moerner, W. E. Principal-components analysis of shape fluctuations of single DNA molecules. *Proc. Natl. Acad. Sci. U. S. A.* **104,** 12622–7 (2007).

14. Fields, A. P. & Cohen, A. E. Electrokinetic trapping at the one nanometer limit. *Proc. Natl. Acad. Sci. U. S. A.* **108,** 8937–42 (2011).

15. Leslie, S. R., Fields, A. P. & Cohen, A. E. Convex lens-induced confinement for imaging single molecules. *Anal. Chem.* **82,** 6224–9 (2010).

16. Moerner, W. & Kador, L. Optical detection and spectroscopy of single molecules in a solid. *Phys. Rev. Lett.* **62,** 2535–2538 (1989).

17. Huisken, J., Swoger, J., Del Bene, F., Wittbrodt, J. & Stelzer, E. H. K. Optical sectioning deep inside live embryos by selective plane illumination microscopy. *Science* **305,** 1007–9 (2004).

18. Siebrasse, J. P., Kaminski, T. & Kubitscheck, U. Nuclear export of single native mRNA molecules observed by light sheet fluorescence microscopy. *Proc. Natl. Acad. Sci. U. S. A.* **109,** 9426–31 (2012).

19. Levene, M. J. *et al.* Zero-mode waveguides for single-molecule analysis at high concentrations. *Science (80-.).* **299,** 682–6 (2003).

20. Cohen, A. E., Fields, A. P., Hou, J. H., Leslie, S. R. & Shon, M. J. In honor of W.E. Moerner: confining molecules for single-molecule spectroscopy. *Isr. J. Chem.* **49,** 275–282 (2009).

21. Lyon, W. A. & Nie, S. Confinement and detection of single molecules in submicrometer channels. *Anal. Chem.* **69,** 3400–3405 (1997).

22. Foquet, M., Korlach, J., Zipfel, W. R., Webb, W. W. & Craighead, H. G. Focal volume confinement by submicrometer-sized fluidic channels. *Anal. Chem.* **76,** 1618–26 (2004).

23. Kamagata, K. *et al.* Long-term observation of fluorescence of free single molecules to explore protein-folding energy landscapes. *J. Am. Chem. Soc.* **134,** 11525–32 (2012).

24. Boukobza, E., Sonnenfeld, A. & Haran, G. Immobilization in surface-tethered lipid vesicles as a new tool for single biomolecule spectroscopy. *J. Phys. Chem. B* **105,** 12165–12170 (2001).

25. Okumus, B., Arslan, S., Fengler, S. M., Myong, S. & Ha, T. Single molecule nanocontainers made porous using a bacterial toxin. *J. Am. Chem. Soc.* **131,** 14844–9 (2009).

26. Chiu, D. T., Lorenz, R. M. & Jeffries, G. D. M. Droplets for ultrasmall-volume analysis. *Anal. Chem.* **81,** 5111–8 (2009).

27. Jofre, A., Case, J. & Hicks, S. Single molecule observations of DNA hybridization kinetics. in *SPIE Nanosci. + Eng.* (Kawata, S., Shalaev, V. M. & Tsai, D. P.) 740014–740014–10 (2009). doi:10.1117/12.828027

28. Gorris, H. H., Rissin, D. M. & Walt, D. R. Stochastic inhibitor release and binding from single-enzyme molecules. *Proc. Natl. Acad. Sci. U. S. A.* **104,** 17680–5 (2007).

29. Rissin, D. M., Gorris, H. H. & Walt, D. R. Distinct and long-lived activity states of single enzyme molecules. *J. Am. Chem. Soc.* **130,** 5349–53 (2008).

30. Li, Z., Hayman, R. B. & Walt, D. R. Detection of single-molecule DNA hybridization using enzymatic amplification in an array of femtoliter-sized reaction vessels. *J. Am. Chem. Soc.* **130,** 12622–3 (2008).

31. Rissin, D. M. *et al.* Single-molecule enzyme-linked immunosorbent assay detects serum proteins at subfemtomolar concentrations. *Nat. Biotechnol.* **28,** 595–9 (2010).

32. Sims, P. A., Greenleaf, W. J., Duan, H. & Xie, X. S. Fluorogenic DNA sequencing in PDMS microreactors. *Nat. Methods* **8,** 575–80 (2011).

33. Rondelez, Y. *et al.* Microfabricated arrays of femtoliter chambers allow single molecule enzymology. *Nat. Biotechnol.* **23,** 361–5 (2005).

34. Mata, A., Fleischman, A. J. & Roy, S. Characterization of polydimethylsiloxane (PDMS) properties for biomedical micro/nanosystems. *Biomed. Microdevices* **7,** 281–93 (2005).

35. Huang, B., Wu, H., Kim, S. & Zare, R. N. Coating of poly(dimethylsiloxane) with n-dodecyl-beta-D-maltoside to minimize nonspecific protein adsorption. *Lab Chip* **5,** 1005–7 (2005).

36. Ruiz-Taylor, L. A. *et al.* Monolayers of derivatized poly(L-lysine)-grafted poly(ethylene glycol) on metal oxides as a class of biomolecular interfaces. *Proc. Natl. Acad. Sci. U. S. A.* **98,** 852–7 (2001).

37. Peters, H. & Schultes, R. On the fluorescence of quartz under the influence of cathode rays of low voltage. *Phys. Rev.* **36,** 1631–1635 (1930).

38. Qin, D., Xia, Y. & Whitesides, G. M. Soft lithography for micro- and nanoscale patterning. *Nat. Protoc.* **5,** 491–502 (2010).

39. Kapanidis, A. N. *et al.* Alternating-laser excitation of single molecules. *Acc. Chem. Res.* **38,** 523–33 (2005).

40. Roy, R., Hohng, S. & Ha, T. A practical guide to single-molecule FRET. *Nat. Methods* **5,** 507–16 (2008).

41. Dorfman, K. DNA electrophoresis in microfabricated devices. *Rev. Mod. Phys.* **82,** 2903–2947 (2010).

42. Vogelsang, J. *et al.* A reducing and oxidizing system minimizes photobleaching and blinking of fluorescent dyes. *Angew. Chem. Int. Ed. Engl.* **47,** 5465–9 (2008).

43. Aitken, C. E., Marshall, R. A. & Puglisi, J. D. An oxygen scavenging system for improvement of dye stability in single-molecule fluorescence experiments. *Biophys. J.* **94,** 1826–1835 (2008).

44. Schwille, P., Meyer-Almes, F. J. & Rigler, R. Dual-color fluorescence cross-correlation spectroscopy for multicomponent diffusional analysis in solution. *Biophys. J.* **72,** 1878–86 (1997).

45. Rothenberger, G. & Grätzel, M. Effects of spatial confinement on the rate of bimolecular reactions in organized liquid media. *Chem. Phys. Lett.* **154,** 165–171 (1989).

46. Polak, M. & Rubinovich, L. Nanochemical equilibrium involving a small number of molecules: a prediction of a distinct confinement effect. *Nano Lett.* **8,** 3543–7 (2008).

47. Holcman, D. & Schuss, Z. Stochastic chemical reactions in microdomains. *J. Chem. Phys.* **122,** 114710 (2005).

48. Landfester, K. Synthesis of colloidal particles in miniemulsions. *Annu. Rev. Mater. Res.* **36,** 231–279 (2006).

49. Barzykin, A. V., Seki, K. & Tachiya, M. Kinetics of diffusion-assisted reactions in microheterogeneous systems. *Adv. Colloid Interface Sci.* **89-90,** 47–140 (2001).

50. Vriezema, D. M. *et al.* Self-assembled nanoreactors. *Chem. Rev.* **105,** 1445–89 (2005).

51. Sawada, T., Yoshizawa, M., Sato, S. & Fujita, M. Minimal nucleotide duplex formation in water through enclathration in self-assembled hosts. *Nat. Chem.* **1,** 53–6 (2009).

52. Fredkin, D. R. & Rice, J. A. Correlation functions of a function of a finite-state Markov process with application to channel kinetics. *Math. Biosci.* **87,** 161–172 (1987).

53. Watson, J. D. & Crick, F. H. C. Molecular structure of nucleic acids. *Nature* **171,** 737–738 (1953).

54. Pauling, L. & Corey, R. B. Structure of the Nucleic Acids. *Nature* **171,** 346–346 (1953).

55. Hagerman, P. J. Flexibility of DNA. *Annu. Rev. Biophys. Biophys. Chem.* **17,** 265–86 (1988).

56. Hagerman, P. J. & Zimm, B. H. Monte Carlo approach to the analysis of the rotational diffusion of wormlike chains. *Biopolymers* **20,** 1481–1502 (1981).

57. Smith, S., Finzi, L. & Bustamante, C. Direct mechanical measurements of the elasticity of single DNA molecules by using magnetic beads. *Science (80-.).* **258,** 1122–1126 (1992).

58. Bustamante, C., Marko, J., Siggia, E. & Smith, S. Entropic elasticity of lambda-phage DNA. *Science (80-.).* **265,** 1599–1600 (1994).

59. Bustamante, C., Bryant, Z. & Smith, S. B. Ten years of tension: single-molecule DNA mechanics. *Nature* **421,** 423–7 (2003).

60. Smith, S. B., Cui, Y. & Bustamante, C. Overstretching B-DNA: the elastic response of individual double-stranded and single-stranded DNA molecules. *Science (80-.).* **271,** 795–799 (1996).

61. Strick, T., Allemand, J.-F., Croquette, V. & Bensimon, D. Twisting and stretching single DNA molecules. *Prog. Biophys. Mol. Biol.* **74,** 115–140 (2000).

62. Shore, D. & Baldwin, R. L. Energetics of DNA twisting. *J. Mol. Biol.* **170,** 957–981 (1983).

63. Shimada, J. & Yamakawa, H. Ring-closure probabilities for twisted wormlike chains. Application to DNA. *Macromolecules* **17,** 689–698 (1984).

64. Podtelezhnikov, A. A. & Vologodskii, A. V. Dynamics of Small Loops in DNA Molecules. *Macromolecules* **33,** 2767–2771 (2000).

65. Cloutier, T. E. & Widom, J. Spontaneous sharp bending of double-stranded DNA. *Mol. Cell* **14,** 355–362 (2004).

66. Du, Q., Smith, C., Shiffeldrim, N., Vologodskaia, M. & Vologodskii, A. Cyclization of short DNA fragments and bending fluctuations of the double helix. *Proc. Natl. Acad. Sci. U. S. A.* **102,** 5397–5402 (2005).

67. Wiggins, P. A. *et al.* High flexibility of DNA on short length scales probed by atomic force microscopy. *Nat. Nanotechnol.* **1,** 137–41 (2006).

68. Vafabakhsh, R. & Ha, T. Extreme bendability of DNA less than 100 base pairs long revealed by single-molecule cyclization. *Science (80-.).* **337,** 1097–1101 (2012).

69. Lane, D., Prentki, P. & Chandler, M. Use of gel retardation to analyze protein-nucleic acid interactions. *Microbiol. Rev.* **56,** 509–28 (1992).

70. Van Mameren, J., Peterman, E. J. G. & Wuite, G. J. L. See me, feel me: methods to concurrently visualize and manipulate single DNA molecules and associated proteins. *Nucleic Acids Res.* **36,** 4381–4389 (2008).

71. Hilario, J. & Kowalczykowski, S. C. Visualizing protein-DNA interactions at the single-molecule level. *Curr. Opin. Chem. Biol.* **14,** 15–22 (2010).

72. Bensimon, A. *et al.* Alignment and sensitive detection of DNA by a moving interface. *Science* **265,** 2096–8 (1994).

73. Lebofsky, R. Single DNA molecule analysis: Applications of molecular combing. *Briefings Funct. Genomics Proteomics* **1,** 385–396 (2003).

74. Ebenstein, Y. *et al.* Lighting up individual DNA binding proteins with quantum dots. *Nano Lett.* **9,** 1598–603 (2009).

75. Doyle, P. S., Ladoux, B. & Viovy, J. L. Dynamics of a tethered polymer in shear flow. *Phys. Rev. Lett.* **84,** 4769–72 (2000).

76. Blainey, P. C., Van Oijen, A. M., Banerjee, A., Verdine, G. L. & Xie, X. S. A base-excision DNA-repair protein finds intrahelical lesion bases by fast sliding in contact with DNA. *Proc. Natl. Acad. Sci. U. S. A.* **103,** 5752–5757 (2006).

77. Tanner, N. A. *et al.* Real-time single-molecule observation of rolling-circle DNA replication. *Nucleic Acids Res.* **37,** e27 (2009).

78. Ferree, S. & Blanch, H. W. Electrokinetic stretching of tethered DNA. *Biophys. J.* **85,** 2539–46 (2003).

79. Wang, M. D., Yin, H., Landick, R., Gelles, J. & Block, S. M. Stretching DNA with optical tweezers. *Biophys. J.* **72,** 1335–46 (1997).

80. Greene, E. C., Wind, S., Fazio, T., Gorman, J. & Visnapuu, M.-L. DNA curtains for high-throughput single-molecule optical imaging. *Methods Enzymol.* **472,** 293–315 (2010).

81. Forget, A. L. & Kowalczykowski, S. C. Single-molecule imaging of DNA pairing by RecA reveals a three-dimensional homology search. *Nature* **482,** 423–7 (2012).

82. Hamon, L. *et al.* High-resolution AFM imaging of single-stranded DNA-binding (SSB) protein--DNA complexes. *Nucleic Acids Res.* **35,** e58 (2007).

83. Lyubchenko, Y. L., Shlyakhtenko, L. S. & Gall, A. A. Atomic force microscopy imaging and probing of DNA, proteins, and protein DNA complexes: silatrane surface chemistry. *Methods Mol. Biol.* **543,** 337–51 (2009).

84. Huisstede, J. H. G., Subramaniam, V. & Bennink, M. L. Combining optical tweezers and scanning probe microscopy to study DNA-protein interactions. *Microsc. Res. Tech.* **70,** 26–33 (2007).

85. Noom, M. C., van den Broek, B., van Mameren, J. & Wuite, G. J. L. Visualizing single DNA-bound proteins using DNA as a scanning probe. *Nat. Methods* **4,** 1031–6 (2007).

86. Van Loenhout, M. T. J. *et al.* Scanning a DNA molecule for bound proteins using hybrid magnetic and optical tweezers. *PLoS One* **8,** e65329 (2013).

87. Fields, A. P., Meyer, E. A. & Cohen, A. E. Euler buckling and nonlinear kinking of double-stranded DNA. *Nucleic Acids Res.* (2013). doi:10.1093/nar/gkt739

88. Zhou, R., Schlierf, M. & Ha, T. Force-fluorescence spectroscopy at the single-molecule level. *Methods Enzymol.* **475,** 405–26 (2010).

89. Han, L. *et al.* Concentration and length dependence of DNA looping in transcriptional regulation. *PLoS One* **4,** e5621 (2009).

90. Parthasarathy, R. Rapid, accurate particle tracking by calculation of radial symmetry centers. *Nat. Methods* **9,** 724–6 (2012).

91. Marko, J. F. & Siggia, E. D. Stretching DNA. *Macromolecules* **28,** 8759–8770 (1995).

92. Vipond, I. B., Baldwin, G. S. & Halford, S. E. Divalent metal ions at the active sites of the EcoRV and EcoRI restriction endonucleases. *Biochemistry* **34,** 697–704 (1995).

93. Bernoulli, J. Quadratura curvae, e cujus evolutione describitur inflexae laminae curvatura. *Die Werke von Jakob Bernoulli* 223–227 (1692).

94. Euler, L. Methodus Inveniendi Lineas Curvas Maximi Minimive Proprietate Gaudentes, sive Solutio Problematis Isoperimetrici Lattissimo Sensu Accepti. (Marc-Michel Bousquet Co., 1744).

95. Landau, L. D., Lifshitz, E. M., Sykes, J. B., Reid, W. H. & Dill, E. H. Theory of elasticity. *Phys. Today* **13,** 44 (1960).

96. Van Kan, J. A., Zhang, C., Perumal Malar, P. & van der Maarel, J. R. C. High throughput fabrication of disposable nanofluidic lab-on-chip devices for single molecule studies. *Biomicrofluidics* **6,** 36502 (2012).

97. Markham, N. R. & Zuker, M. DINAMelt web server for nucleic acid melting prediction. *Nucleic Acids Res.* **33,** W577–81 (2005).

98. Levien, R. The elastica: a mathematical history. … Eng. Comput. Sci. Univ. … (2008).